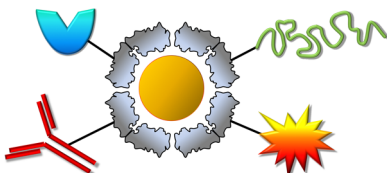


Ferritin: A Versatile Building Block for Bionanotechnology

Günther Jutz,^{†,§} Patrick van Rijn,^{†,‡,§} Barbara Santos Miranda,[‡] and Alexander Böker^{*,†}

[†]DWI - Leibniz-Institut für Interaktive Materialien e.V., Lehrstuhl für Makromolekulare Materialien und Oberflächen, RWTH Aachen University, Forckenbeckstrasse 50, D-52056 Aachen, Germany

[‡]Department of Biomedical Engineering-FB40, W.J. Kolff Institute for Biomedical Engineering and Materials Science, University of Groningen, University Medical Center Groningen, A. Deusinglaan 1, 9713 AV Groningen, The Netherlands



CONTENTS

1. Introduction: Bionanotechnology	A
1.1. Introduction to Ferritin	B
1.2. The Structure of the Mammalian Ferritin Protein Shell	C
1.3. The Native Ferrihydrite Core of Ferritin	D
1.4. Other Iron Binding Protein Cages	E
1.4.1. Thermally Stable Ferritins	F
1.4.2. Ferritin from <i>Listeria innocua</i>	G
2. The Ferritin Protein Shell as Multivalent Scaffold	H
3. Synthesis of Nanophase (In)organic Materials in the Ferritin Protein Cage	I
3.1. Encapsulation of Molecules and Ionic Species in the Interior of Ferritin	J
3.2. Synthesis of Inorganic Cores in the Protein Cage of Ferritin	K
3.2.1. Formation of Mineral Cores	L
3.2.2. Formation of Semiconductor Core Particles	M
3.2.3. Formation of Metal and Metal Alloy Cores	N
3.3. Synthesis of Inorganic Cores in Ferritin-Like Cages	O
4. Fabrication of Two-Dimensional Arrays of Ferritin	P
4.1. Ferritin Adsorption and Assemblies at Fluid Interfaces	Q
4.2. Ferritin Immobilized on Solid Surfaces	R
4.2.1. Covalent Attachment of Ferritin	S
4.2.2. Electrostatic Interactions on Solid Interfaces	T
4.2.3. Specific Interactions	U
5. Electrochemical Properties of Ferritin	V
6. Ferritin in Applications	W
6.1. Ferritin in Functional Nanostructured Composite Materials	Z
6.2. Applications in Semiconductors and Nanoelectronics	AB
6.3. Applications in Medicine and Diagnostics	AC
6.3.1. Ferritin as Drug Delivery System	AD
6.3.2. Ferritin Nanoparticles for Biomedical Diagnostics	AG

6.3.3. Basic Magnetic Properties of Magnetic Ferritin Particles	AM
6.3.4. Magnetic Ferritin Nanoparticles, Attractive for MRI Applications	AO
7. Conclusions and Outlook	AP
Author Information	AP
Corresponding Author	AP
Author Contributions	AP
Notes	AP
Biographies	AP
References	AQ

1. INTRODUCTION: BIONANOTECHNOLOGY

Nature is a great source of inspiration in solving extremely complex problems, and it is every day more common to use its strategies for the development of new materials, methods, and even structure fabrication. The approach of using natural occurring structures for nanotechnology applications is very nicely supplementing conventional technologies based on photolithography, which is approaching its lower theoretical limits. Furthermore, increased levels of sensitivity and specificity need geometric miniaturization of structures with functionalities positioned at regular and specific locations. Biological supramolecular assemblies possess this precise location of functions, monodisperse properties, and have dimensions in the low nanometer regime, which makes them ideal as nanoscaled building blocks and biotemplates.^{1–5} Protein biotemplates have been combined with many inorganic materials, for example, minerals, magnetic, and semiconductor materials as well as metals.^{6,7}

Proteins also allow for a convenient functionalization with ultimate precision via genetic engineering.⁸ An emerging branch of bionanotechnology makes use of various protein-based structures for production of novel structures and materials, for example, for biosensing,⁹ especially with inorganic components.¹⁰ The combination of inorganic materials with cage proteins like ferritin, virus capsids,¹¹ lumazine synthase,¹² and heat shock proteins¹³ is especially interesting. These are promising building blocks for nanofabrication because the interior space of cage proteins can host a variety of inorganic materials. The “bottom-up” approach for building nanomaterials entails the assembly of complex structures and functions from simpler building blocks.

Received: January 11, 2013

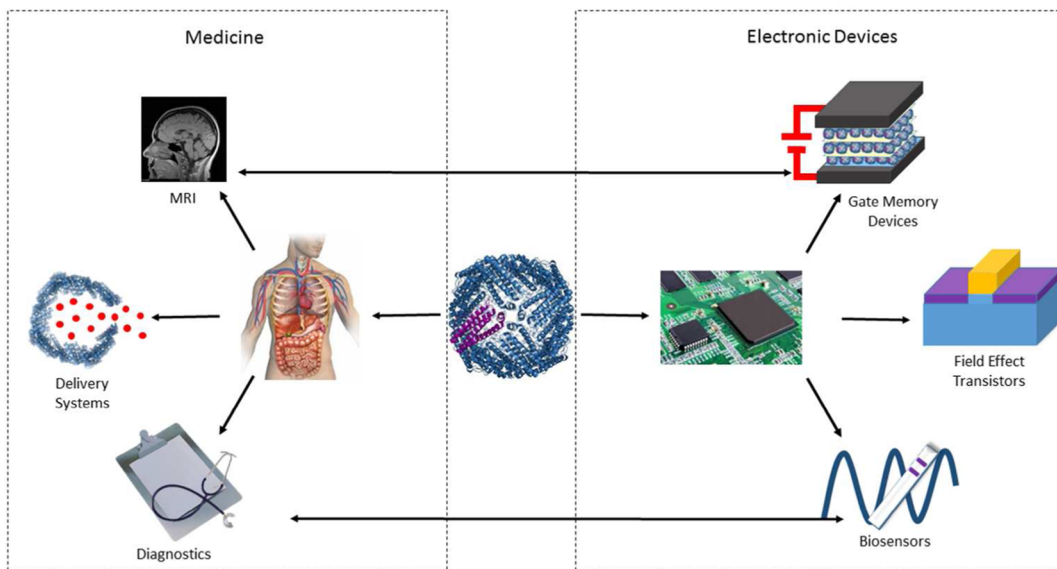


Figure 1. Various fields of research within (bio)medical applications, chemistry, materials science, (bio)sensors, and electronic devices can be targeted using ferritin.

For the development of protein–hybrid structures, ferritin is an often chosen biological structure due to its well-known structural features, stability, capability to mineralize a variety of minerals and metals within its cage structure,¹⁴ and possibility of redesigning the interior of ferritin via genetic engineering.¹⁵ Therefore, combining material specificity in the outer surface of ferritin with the mineralization within its interior space, ferritin-like cage proteins could be used to assemble a wide variety of novel inorganic composite materials on the nanoscale. Here, an extensive overview is presented on the various structural modifications of ferritin and ferritin-like structure and their development toward systems and materials used in a wide variety of areas ranging from templated ordered materials and (bio)medical applications to the integration of the structures into electronic devices and other nanochemical systems (Figure 1).

1.1. Introduction to Ferritin

Ferritin describes a family of iron storage proteins with ubiquitous distribution among all life forms, with the notable exception of yeast (vertebrate;^{16–18} bacterioferritin;^{19–21} DNA-binding protein from starved cells (Dps);^{22–24} plants;^{25,26} insects²⁷), and they are the most abundant members of the ferritin-like superfamily and may have developed from a rubrerythrin-like ancestor protein with two homologous pairs of antiparallel helices as main structural feature.^{28,29} A carboxylate-bridged di-iron center within the four-helix bundle can be considered as a general similarity within the ferritin family. On the basis of sequence similarities, which show the high conservation or conservative substitution of few key structural residues of the iron-binding and -chelating motifs, it was suggested that ferritins are obligate proteins for aerobic metabolism.³⁰ Ferritins and Dps function as dynamic iron storage, and Fe(II) sequestration not only prevents spontaneous oxidation to Fe(III) and production of toxic free radicals but also has various other functions that have been identified recently.^{17,31} Ferritin seems the only way to handle iron with its low solubility and potential harmful participation in free radical reactions. The protein shell influences the formation of a mineral iron oxide phase from which efficient mobilization of

the essential element iron can occur despite its very low solubility.³² The important biological role of ferritin and related proteins in homeostasis of ferrous ion level and as oxidative stress protection system is not discussed here, but the reader is referred to reviews and references therein. A recent dedicated volume of *Biochimica et Biophysica Acta* gives an excellent collection of articles on various aspects of ferritin biochemistry.¹⁸ The cellular regulation of ferritin gene transcription and mRNA translation was summarized by Hintze and Theil.³³ Alkhateeb and Connor reviewed the current status of knowledge on nuclear ferritin and its possible function as transcription factor.³⁴ The role of cytosolic and mitochondrial ferritins in the regulation of cellular iron homeostasis and the newly insight that ferritin may act in some disorders as a pro-oxidant has recently been described by Arosio and Levi.³⁵ Knovich, Torti, and co-workers reviewed serum ferritin as clinical tool and its importance as marker for total body iron storage and indicator of several physiologic and pathologic processes from the perspective of a clinician.^{36,37} Finally, ferritin and its role as iron source in nutrition were discussed by Theil et al.³⁸ A correlation of iron accumulation in the brain and pathological ferritin with neurodegenerative disorders is a topic of current research interests in biomedicine. An excellent review probably encompassing all literature about ferritin biochemistry until 1996 was published by Harrison and Arosio.¹⁶

Nevertheless, the particular features of the cage structure and iron oxide core formation will be summarized here as they are the basis for the extraordinary capabilities of ferritin and its numerous applications in the field of bionanochemistry. The next sections deal mainly with the structural basics of horse and human ferritin, representative for the mammalian ferritins with the conserved ferroxidase motif. Bacteria can contain three subfamilies of ferritin.^{22,28,39} Bacterial ferritin has similarity to mammalian H chain ferritins with 24 identical subunits. Bacterioferritins bind additionally an iron-protoporphyrin (heme-like) at the 2-fold symmetry center at the interface between two subunits, which is not involved in iron mineralization but in iron mobilization from the core. The 8 nm in diameter Dps is composed of 12 subunits (3/3/2 octahedral symmetry) and found only in prokaryotes. Dps

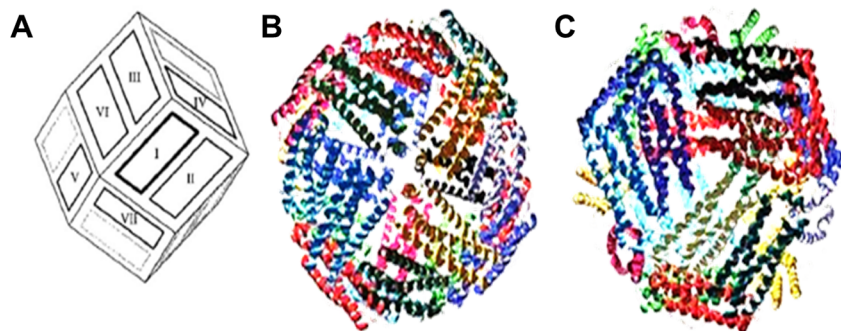


Figure 2. Ferritin subunit symmetry relations. (A) Schematic diagram illustrating the relation between symmetry-related subunits. (B) View of the ferritin molecule down the 4-fold symmetry axis. (C) View of the ferritin molecule down the 3-fold symmetry axis. Reprinted with permission from ref 42. Copyright 2010 Elsevier.

oxidizes iron at sites between the 2-fold related subunits using exclusively hydrogen peroxide.²³ Its major function is the prevention of harmful Fenton chemistry by catalytic turnover of hydrogen peroxide and Fe(II) to water and Fe(III), thus protecting DNA against iron-induced redox damage.²² The protein shell of plant ferritin is composed of 24 identical H/L hybrids: The subunits contain a ferroxidase center but all of the amino acids typical for L-chains as well. Both channels in plant ferritins are hydrophilic. Their cores are amorphous with a high phosphor/iron (P/Fe) ratio of 1:3.^{25,26} While ferritins from bacteria, plants, and animals share many common structural features, they differ vastly in their way of expression and regulation.¹⁶

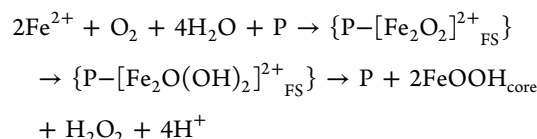
1.2. The Structure of the Mammalian Ferritin Protein Shell

The principal tertiary (particularly the central four-helix bundle) and quaternary structure is highly conserved throughout a broad range of species, but the amino acid sequence can vary significantly.²⁹ Generally, 24 protein subunits self-assemble in dimers to form a dodecameric cage with an outer diameter of approximately 12 nm and an inner cavity of 7–8 nm, which is filled with a ferric oxohydroxy core (Figure 2). Ferritin devoid of the inorganic core is called apoferritin. The protein cage is temperature stable up to 85 °C and tolerates reasonably high levels of urea, guanidinium chloride, and many other denaturants at neutral pH.^{40,41} Ferritin preparations from natural sources possess some heterogeneity, arising from irreversibly aggregated dimers and trimers.

Today, there is a pretty clear image of the ferritin shell structure by X-ray diffraction as reviewed recently by Crichton and Declercq and Harrison and co-workers (Figure 2).^{29,42} The protein shell of mammalian ferritin is usually heterogeneous and consists of a mixture of two subunits of about 21 kDa, termed H for heavy (predominant in heart) and of about 19 kDa, termed L for light chain (predominant in liver), with around 55% amino acid homology for human H- and L-ferritin.²⁹ The H-chain contains the highly conserved di-iron binding site (intrasubunit ferroxidase center), which binds and oxidizes ferrous ions.⁴³ Iron oxidation in pure L-chain ferritins is much slower because they only provide a favorable nucleation site in the protein cavity but have no catalytic ferroxidase center.^{31,44} The ratio of the subunits varies between organisms as well as between different tissues within an organism, reflecting the different functions, fast iron metabolism or long-term iron storage, of the various isoferritins required in different tissues.¹⁷ The commercially available and

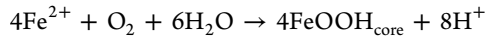
most frequently used ferritin from horse spleen contains approximately 90% L-subunits.

Each of the subunit proteins form a four-helix bundle with a left-hand twist that arranges in 12 antiparallel pairs, sharing the 3-fold symmetry axis, to build a roughly rhombic dodecahedron shape (space group $F432$).^{45,46} The resulting eight funnel-like channels at the 3-fold axis are hydrophilic in nature. The six channels at the 4-fold axis are surrounded by the short fifth E helices at the C-terminus, which are lying at an angle of about 60° with respect to the four long helices and provide a hydrophobic lining of leucine residues. Both channels are approximately 0.4 nm wide. Iron entry occurs most likely through the 3-fold channels. The electrostatic field gradient directs cations to the channel entrance and guides them to the interior.^{42,47} Only the H-subunit has a highly conserved ferroxidase center within the four-helix bundle, which catalyzes the oxidation of two Fe(II) ions by consumption of oxygen and the intermediate product H_2O_2 .^{43,48} The initial intermediate at the ferroxidase site is a μ -1,2 diferric-peroxo-complex, which decays to diferric-oxo-clusters. In various, but not in all, ferritins, the blue peroxo-complex could be observed by stopped-flow UV-vis spectroscopy.⁴⁹ The scheme for the ferroxidase reaction reads:⁴⁹



with “P” as a vacant ferroxidase site and in braces the μ -1,2-peroxo- and -oxo(hydroxo) di-iron(III) intermediates. Lacking the catalytic ferroxidase center, L-homopolymer ferritin can still oxidize iron but at much lower rates than H-chain ferritin. Some L-chains in the ferritin shell, however, help in accelerating the iron transport and clearing the catalytic site on the H-chains. At a high L- to H-chain ratio, the observed net oxidation stoichiometry changes to $3\text{Fe}(\text{II})/\text{O}_2$, pointing to a two-step reaction involving ferroxidation ($2\text{Fe}(\text{II})/\text{O}_2$) and direct mineralization on the core ($4\text{Fe}(\text{II})/\text{O}_2$).⁴⁹ Ferritin cores in heteropolymer or L-chain ferritins were reported to be structurally more ordered, a hint on preferred nucleation sites on L-chains. Such mineral “anchors” of 4–8 carboxylic acid residues protrude from the interface of subunit dimers to the interior and are believed to act as chelation sites for the formation of iron oxides.^{31,44} In the absence of the ferroxidase site, they may accumulate Fe(II) and Fe(III) and initiate oxo-bridge and nuclei formation through a high local ion

concentration.⁵⁰ At low iron flux of up to 48 iron atoms per ferritin, the catalytic centers are saturated first and iron oxidation occurs mainly through catalytic turnover at the ferroxidase site. If more iron is incoming and a mineral core is formed, iron can also be directly catalytically oxidized and deposited on the surface of the growing mineral core.¹⁶ This mineralization reaction consumes O₂ and H₂O₂ and becomes the predominant reaction, thus leading to the overall experimentally observed stoichiometry of^{16,49}



Today, several investigations indicate toward the entering and exiting of iron through the 3-fold channels, which act as gated pores.⁵¹ For such experiments, ferritin core dissolution under reductive conditions (e.g., NADH/FMN) can be conveniently followed spectroscopically with bipyridine as reporting chelator in solution. Thus, it was shown that any conservative or nonconservative change of amino acids in the 3-fold channel did not alter the subunit folding or disrupting the protein shell but increased iron dissolution rate strongly.⁵² Circular dichroism spectroscopy revealed a low temperature structural melting point that originates from softening of about 10% of the α -helices, presumably at the 3-fold channels, the postulated gated pores. Similar reversible subdomain unfolding was achieved with low concentrations of chaotropes such as 0.001–1 M urea.⁴¹ Likewise, the release of iron from ferritin by aceto- or benzohydroxamic acids was strongly increased in the presence of 10 mM urea. The effect was pH-dependent, and a higher release of iron was observed at pH 7.4 with respect to pH 5.2.⁵³ Albeit the pore function by softening of the protein structure through localized unfolding seems established, no factor triggering the iron release *in vivo* has been found yet. However, in a recent study with a combinatorial heptapeptide library, two ferritin binding oligopeptides were found, which increased and decreased the rate of Fe²⁺ exit, respectively.⁵⁴ Recently, also a cytosolic chaperon that binds iron and loads ferritin was identified. Increased iron loading of ferritin was observed when ferritin and the chaperon were coexpressed in yeast.⁵⁵ The work of Theil and co-workers and others in that field is summarized in a short mini-review.^{51,56}

In recent work, Theil and co-workers unraveled a likely transport path of (ferrous) metal ions from the outside to the inner cavity of the symmetrical M ferritin of bullfrog.⁵⁰ The location of cocrystallized Mg(II) and Co(II) ions traced the way through the 3-fold pore to the inner cavity and the di-iron catalytic site.⁵⁷ The ferrous product after the catalytic turnover is then guided from the ferroxidase center to the subunit C-terminus within the protein shell where it is released to the mineralization site in the cage interior. Paramagnetic effects of coordinate iron species on the lining amino acid residues allowed for tracing the channel within the four-helix bundle by NMR spectroscopy.⁵⁸ Another mosaic in the iron translocation mechanism was provided by the identification of a well-conserved transit site.⁵⁹

While there has been considerable progress in tracing the pathway of iron from the 3-fold channel to the ferroxidase site and to the capsid's interior, the nature of the ion transport across the ferritin shell is still obscure. On the one hand, studies with nitroxide radical spin probes showed that only positively charged spin probes entered the ferritin interior. On the other hand, platinum particles were successfully formed inside ferritin upon incubation with [PtCl₄]²⁻,^{60,61} which would involve diffusion of a large negative anion through the shell or prior

stripping of ligands from a stable ion-complex. Possible pathways include the gated pores at the 3-fold axis (see above).

Apo ferritin can be readily disassembled and reassembled by reducing the pH to a value as low as pH 2 and increasing it above pH 7, respectively.⁶² During the recombination process, the bulk solution and dissolved molecules as well as nanoparticles can be entrapped in the interior, which is an efficient way to encapsulate material that is unable to enter the cavity of the intact protein shell through one of the pores. Webb et al. gave a rough estimation of the internal volume of 1.4 × 10⁻¹⁹ cm³, which can hold solubilized species. More about this approach will be given in section 3.

1.3. The Native Ferrihydrite Core of Ferritin

The iron oxide content can vary significantly from a few Fe-atoms to clusters with theoretically up to 4500 Fe-atoms. Typically, an average of 2000 iron atoms is present. The chemical composition of the core can be described in a simplified form as hydrated ferric oxide (ferrihydrite) with a stoichiometry of 5Fe₂O₃·9H₂O.⁴⁴ The protein cage directs the formation of the relatively low stable ferrihydrite as compared to other hydrous iron oxides like lepidocrocite or goethite, which precipitate in protein-free solutions and probably ensure thus its later mobilization.³² Phosphate is further associated with most native ferritins in significant amounts, particularly plant and bacterial ferritin with up to one phosphate per iron atom. These cores are typically amorphous. Phosphate in mammalian ferritin is mostly surface bound. The associated anions are also responsible for the surface binding and oxidation of Fe²⁺ and might be eventually incorporated in this way. There is no evidence that phosphate helps the ferroxidase center. Rather, the interaction of incoming iron with the growing core, capped with phosphate, leads to an accelerated growth of the core.⁴⁷

Characterization of the native ferrihydrite core of ferritin has been notoriously difficult. The nanoparticulate structure of ferrihydrite with its inherent structural disorder is still a matter of debate. Aspects like crystallinity, magnetic properties, and reactivity depend strongly on the size, structure, and composition of the ferrihydrite particles, which vary depending on the mineralization conditions and biological source of native ferritin.^{44,63} Broadly, two forms of the nanoparticulate mineral can be distinguished, 2-lines and 6-lines particles, according to the number of peaks in the XRD pattern. Dark-field TEM shows small disordered 2 nm crystallites in 2-line ferrihydrite and 2–4 nm crystallites in 6-line ferrihydrite consistent with the XRD and electron diffraction pattern of the two samples.⁶⁴ The two crystallites do not only differ in their apparent crystallinity but also in their magnetic behavior, which was mainly ascribed to their different particle size. Michel et al. list some of the suggested structural models for ferrihydrite.⁶³ Nanosized hematite was sometimes included in this structural model as well to fit scattering data. The single phase model for scattering domain sizes of 2–6 nm suggests a basic structure with a central tetrahedral coordinated iron, which is surrounded by 12 edge-sharing FeO₆ octahedra.⁶⁵ Total scattering data for reconstituted ferritin cores show a smooth transition from the curve of a 2-line ferrihydrite for ferritin loadings with 500 iron atoms to the curve shape of a 6-line ferrihydrite for ferritin loadings with 3000 iron atoms. This continuous change supports the single phase model and suggests that size and crystallinity of the core as well as a size-dependent strain are the

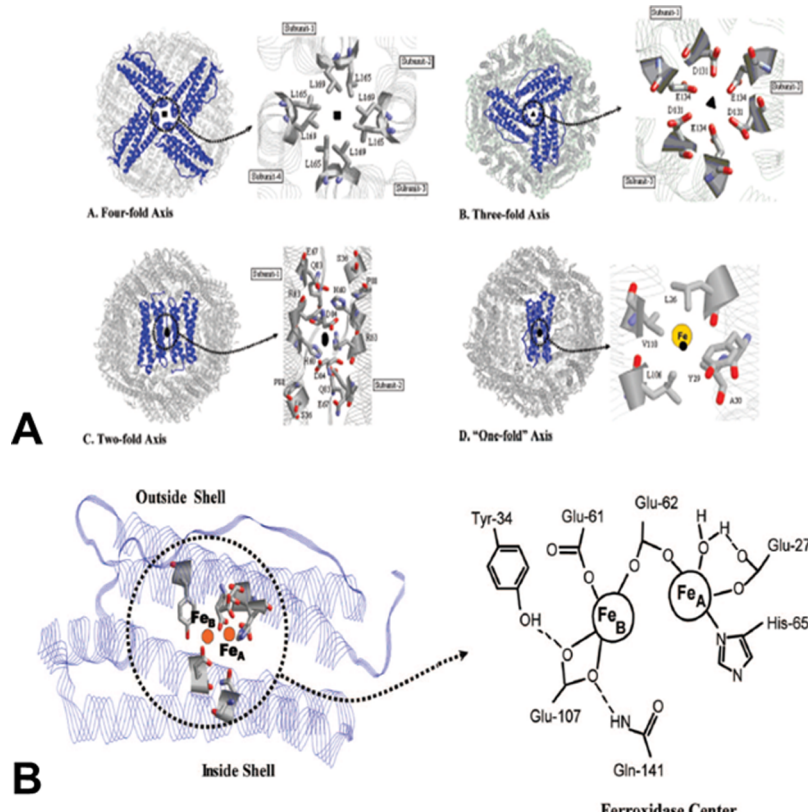


Figure 3. (A) Ferritin protein shell with views down the (A) 4-, (B) 3-, (C) 2-, and (D) “1-fold” axes (channels) of the protein shell. The full protein shell is shown on the left with the rotation symmetry related subunits indicated in blue. An expanded view of each type of channel is shown on the right with key residues indicated. The “1-fold” rotation axis is a C1 axis (rotation through 360°). There are an infinite number of such axes in the protein, but the one shown lies along a narrow channel leading to Fe (yellow) in the A site of the ferroxidase center (see B) and thus has special significance. (B) Tyr29 extends into the exterior solution. Ferroxidase center of human H-chain ferritin located within the four-helix bundle (left). Schematic view of the ferroxidase center (right). The ligands are those observed in the X-ray structure of Zn²⁺ bound at the ferroxidase site. Reprinted with permission from ref 66. Copyright 2008 American Chemical Society.

main differences between various ferritin-derived ferrihydrite particles.⁶³

To analyze a possible substructure of the ferritin core, Galvez et al. gradually removed iron from fully loaded horse spleen ferritins (~2200 iron atoms) (Figure 3).⁶⁶ On the basis of their findings from bright-field TEM, SAXS, and X-ray absorption near-edge spectroscopy (XANES), they suggested a ferrihydrite-enriched core with a magnetite surface. Electron energy-loss spectroscopy (EELS) across single cores confirmed a higher fraction of iron(II) species at the surface of the cores. SQUID (superconducting quantum interference device/magnetometer) magnetic measurements supported their findings in that fully loaded ferritin behaved more like a superparamagnetic particle (ferrihydrite core dominating), while the behavior of depleted ferritin with a higher fraction of shell magnetite was more ferrimagnetic. In contrast, Pan et al. found predominantly ferrihydrite cores in human hepatic ferritin containing only iron(III). In the detailed discussion in their report, they suspected that high electron fluxes in most of the previous investigations may have induced coordination and valence changes, which they considered carefully for the first time in their study.⁶⁷ High angle annular dark field (HAADF) images from scanning transmission electron microscopy (STEM) confirmed the polycrystallinity of the cores. After normalizing the image intensity of particles in STEM HAADF with the number of core iron atoms from EELS, the core reconstruction revealed a cubic arrangement of crystal granules corresponding

to the symmetry of the protein shell with its eight hydrophilic channels as the 3-fold symmetry axis.

Holo-ferritin exhibits a remarkable affinity for anions and some nonferrous metal ions. Investigations with apoferritin, holoferritin, phytoferritin, and synthetic iron cores clearly showed that it is the iron core that is responsible for uptake of large amounts of, for example, phosphate.⁶⁸ Ferritin can bind other nonferrous metal ions, but phosphate-free synthetic cores had a much reduced ion binding capability.⁶⁹ Among Cd²⁺, Zn²⁺, Cu²⁺, Co²⁺, Mn²⁺, and Mg²⁺, only Cd²⁺ was bound in stoichiometric amounts to apoferritin. The authors proposed that the very strong surface binding of phosphate ions to the positively charged ferrihydrite core can neutralize the surface charge and give a more anionic character, and thus install a number of ionic binding sites for nonferrous metal cations. The investigations show that ferritin binds nonferrous metal-ions *in vivo* and *in vitro*, suggesting that holoferritin can have a detoxifying physiological role.

The uptake of anions caught considerably less attention. As mentioned, the ferrihydrite cores absorb significant amounts of phosphate, which is mostly superficial in mammalian ferritins. Plants and bacterial ferritins contain very high amounts of phosphate throughout the core, which are consequently less regular.⁴⁴ However, phosphate incorporation is more a matter of the reconstitution solution than a property of the different protein shells. Other oxoanions like arsenate, vanadate, and

molybdate will be incorporated in vitro as well in an approximate 1:1 fashion, but not sulfate, nitrate, or carbonate.⁷⁰

Direct demineralization of the iron core in ferritins can be induced with strong Fe(III) chelators. Domínguez-Vera and co-workers used catechol in the presence of urea or hydroxamic acids to release iron from the ferritin core by direct chelation of Fe(III).^{53,71} Addition of reductants markedly facilitates and increases the release rate of iron as iron(II).¹⁶ Demineralization proceeds very effectively with dithionite as reduction agent in the presence of bipyridine at low pH, but thioglycollic acid is mostly used because it has a slightly lower mobilization rate as compared to other thiols. Complex formation of SO₃²⁻ and thiols with Fe(III) core surface sites in the case of reduction by dithionite or thiols was suggested to explain the differing behaviors.⁷² FMNH₂ as well as ascorbate can also be used as a reductant.^{73,74} 2,2-Bipyridine and 1,10-phenanthroline are among other polypyridyl ligands frequently used as Fe(II) scavengers, which allow spectroscopic following of the iron mobilization.^{74,75} Little is known about the biochemical pathways of iron release in vivo.⁴⁷ Recently, an iron binding chaperone was identified, which possibly mediates iron.⁵⁵ Efforts were also spent toward modeling the kinetics of the dynamic iron storage in ferritin.⁷⁶

1.4. Other Iron Binding Protein Cages

Various other protein cage architectures can be utilized as a size- and shape-constrained reaction environment for the synthesis of nanomaterials of which the small heat shock proteins (Hsp), a 12 nm protein cage with 4:3:2 symmetry, are the most important.⁷⁷ Hsp was used as a multivalent drug display as well as container for catalytically active species.^{78,79} Hsp from *Methanococcus jannaschii* was incubated with PtCl₄²⁻ at 65 °C for 15 min before nanoparticles were formed by reduction with dimethylamine borane. At a loading of 1000 Pt per cage, the average diameter of the Pt-clusters was 2.2 ± 0.7 nm. The Pt-nanoparticles proved to be an efficient catalyst for H₂-production. The Pt-nanoparticles are not as strongly passivated as conventional prepared Pt nanoparticles but not sensitive to oxygen or carbon monoxide, even though they are poisoned by thiols.

Another interesting but not yet widely investigated class of protein cages with iron binding capability are so-called DNA-binding proteins from starved cells (Dps). Dps protects DNA by reducing oxidative stress; their precise function is still under investigation. The characterization and a phylogenetic classification were presented by Douglas and co-workers for the 10 nm dodecameric protein cage of Dps found in *Sulfolobus solfataricus*.⁸⁰ Such particles can be used, for example, for nanoparticles synthesis or for the decoration of surfaces, similar to that for ferritins.⁸¹ Because various species have ferritin and ferritin-like protein cages, differences in structure, morphology, and size can be expected. Figure 4 provides some basic dimensions and symmetry elements and compositions of the mostly used ferritin and ferritin-like molecules.

1.4.1. Thermally Stable Ferritins. Biomimetic synthetic approaches are currently mainly restricted by the thermal stability of the biological components. The preparation of novel nanomaterials or different phases of nanomaterials in vitro requires sometimes increased temperatures, which are not tolerated by many biological scaffolds. However, during the recently emerging interest in thermophilic and hyperthermophilic archaea, a number of thermally stable protein cages were identified and isolated. They can be used to expand the

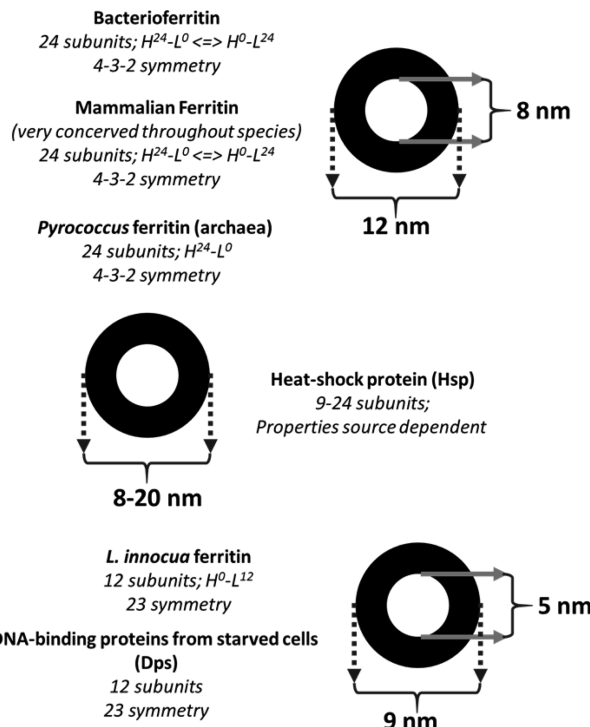


Figure 4. Ferritin and ferritin-like cages can deviate when originating from different organisms. Here, the basic features of ferritins originating from different sources are shown regarding number of subunits, composition between light (L) subunits, and heavy (H) subunits and symmetry.

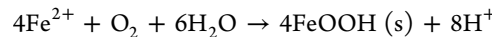
temperature range for the synthesis of novel bioinorganic composite materials in vitro.

Pyrococcus furiosus is a marine anaerobe that resides in thermal springs where temperatures can reach up to 120 °C. A ferritin protein was cloned from the organism and expressed in *E. coli*.^{82,83} The structure was found to be homologous to other ferritins, but the ferroxidase center contains a third iron site, which acts as a stable redox-active prosthetic group that is different from mammalian ferritins.⁸⁴ Parker et al., who studied also the biomimetic synthesis of maghemite nanoparticles at elevated temperatures with mammalian ferritins, used the *Pyrococcus* ferritin (PfFn) for an improved synthesis of the important maghemite nanomaterials.⁸⁵ Magnetic iron oxide nanoparticles are of special interest for magnetic resonance imaging (MRI), cancer treatment, and memory storage. The stability of PfFn toward temperatures as high as 120 °C was confirmed by dynamic light scattering and size exclusion chromatography measurements. The template synthesis of ferromagnetic γ-Fe₂O₃ encapsulated in the interior of the protein cage was successful for temperatures up to 85 °C; however, higher temperatures led to precipitation of bulk iron oxides. Nevertheless, the temperature range was expanded with 20 °C as compared to mammalian ferritin as template. In another study, largely amorphous ferrihydrite cores inside the hyperthermophilic ferritin of *Pyrococcus furiosus* were converted under boiling conditions to hematite (α-Fe₂O₃).⁸⁶ The subtle differences in charge distribution between inner and outer shell as well as the location of certain amino acids acting as metal binding and nucleation sites can have a strong influence on the formed nanoparticles. Thus, in *Pyrococcus furiosus* ferritins, single small Ag nanoparticles (2.1 ± 0.4 nm) were formed, but not in human ferritin.⁸⁷

1.4.2. Ferritin from *Listeria innocua*. When Chiancone and co-workers isolated a new nonheme iron-binding protein complex from the Gram-positive bacterium *Listeria innocua*, the high sequence similarity to Dps was immediately recognized.⁸⁸ Dps are a diverse group of multimeric bacterial polypeptides that bind and protect DNA in cells that are exposed to oxidative or nutritional stress. Further, among the different classes of known ferritins, the sequence similarity of *L. innocua* ferritin is highest with mammalian L-chain subunits. Thus, the bacterial ferritin from *L. innocua* provided a first evidence of a common evolutionary origin of the ferritin and Dps superfamilies. Both the *L. innocua* ferritin and the Dps from *E. coli* assemble into dodecamers. First structural investigations revealed that *L. innocua* ferritin is a cage-like, spherical complex of 240 kDa in weight, composed of subunits with a mass of 18 kDa with an inner diameter of 4 nm and an outer diameter of 10 nm, and Chiaraluce et al. showed the extraordinary stability of the protein cage below pH 2.⁸⁹ The native protein contains only very few iron atoms, but upon reconstitution with Fe-ions in the presence of molecular oxygen, electron microscopy revealed the formation of electron dense cores with very narrow size distribution.⁸⁸ The *Listeria* ferritin accelerates Fe²⁺ oxidation about 4-fold over autoxidation and can sequester up to 500 iron atoms inside the spherical cavity.⁹⁰ The monomeric protein folds into a four-helix bundle, which is stabilized by hydrophobic interactions. The principal structural similarity of the four-helix bundle but also the differences from *E. coli* Dps and horse spleen L-chain ferritin are discussed in detail by Ilari et al.⁹⁰ The dodecameric structure has 23 symmetry; that is, the four trimers are placed at the vertices of a tetrahedron. Thus, the 3-fold axes, passing through the vertices and the centers of the opposite site, have two different, nonequivalent environments. One, designated as “ferritin-like”, is characterized by a hydrophilic pore, which provides the pathway for iron entry into the cavity. Similar to ferritin, the pores are lined by negatively charged residues and surrounded by two lysine residues. The other 3-fold environment shares structural features with Dps proteins and is thus called “Dps-like”.⁹⁰ The *L. innocua* ferritin sequence contains a cluster of carboxylate residues similar to the iron core nucleation site in mammalian ferritin L-chains. Although no part of the canonical ferroxidase center residues within a subunit can be found, an iron binding site can be found at the interfaces of the subunits, which are related to each other by 2-fold symmetry and have the chemical nature and stereochemistry known for ferroxidase sites. In ferritins, the iron core nucleation sites are formed by carboxylate residues only, while the redox process of iron in the ferroxidase site is accomplished by carboxylate residues and histidine residues. In *L. innocua* ferritin, it is the specific alignment and involvement of two histidines that makes the iron binding site bifunctional, as ferroxidase and nucleation site. This explains why L-ferritin that lacks the histidines also lacks ferroxidase activity despite containing a cluster of negatively charged residues in the same helix. This double function could also be the explanation for the lower ferroxidase activity of *Listeria* ferritin, which amounts to only one-third to one-fourth of that of mammalian recombinant H-chain ferritin or *E. coli* bacterioferritin. The strong negatively charged internal surface as interface for deposition of the iron oxide minerals finally completes the important structural and functional features for iron oxidation and storage. The strong similarity in chemical nature and spatial arrangement of the iron coordinating ligands of the iron-binding site of *Listeria* and the ferroxidase centers

led to the conclusion to assign the *Listeria* iron-binding site to the ferroxidase family. Vice versa, the strong similarity of the *Listeria* ferritin with *E. coli* Dps further supports the proposed iron binding capacity as a general feature of Dps. The release of iron-mediated stress can protect DNA, and thus “DNA-binding signature” might be a misleading connotation regarding the biological function of the Dps protein.⁹⁰

Theil, Chiancone, and co-workers showed that iron translocation occurs through the ferritin-like pores and can be modulated by changing the electrostatic gradient. For this, they created a few single site variants by changing the pore-lining Asp to Asn.⁹¹ A detailed study of iron oxidation and hydrolysis reactions of *Listeria* ferritin was performed by Chasteen and co-workers.^{92,93} *L. innocua* incorporates iron very efficiently but does not bind DNA despite the structural similarities to Dps. Upon mixing ferritin with iron(II) as FeSO₄, the oxygen consumption and H⁺ production were measured simultaneously in buffer-free conditions. Similarly to mineralization in *E. coli* bacterioferritin, three phases were observed. The first phase is ascribed as rapid Fe²⁺ binding to the protein shell with a half-life of less than 0.8 s, which was given by the response time of the pH electrode. One proton per bound iron(II) is released. Phase 2 corresponds to the ferroxidase reaction, that is, oxidation of iron(II) to iron(III) at the dinuclear metal complex. Autoxidation is initially slower, but due to the autocatalytic effect of the precipitating FeOOH (s), the reaction rate becomes faster later on. In the ferritin protein controlled reaction, phase 3 reactions, which corresponds to oxidation/mineralization, are faster than phase 2 reactions (the oxidation of the initially bound 24 iron(II) ions). Some not yet clarified synergism seems to occur here. The final phase 3 oxidation/mineralization stoichiometry reads:



which is the same as for bacterioferritins and mammalian ferritins. Competitive experiments with H₂O₂ indicated that peroxide is a better oxidant than O₂ in *Listeria* ferritin. Fast consumption of eventually produced peroxide at another ferroxidase site might explain why H₂O₂ cannot be found while it accumulates to measurable levels for mammalian ferritins.

In this way, Dps–nanoparticle composites have been used in applications in ways similar to those of ferritin, for example, as catalyst for the growth of single-walled carbon nanotubes⁹⁴ or for the size constrained mineralization with ferrimagnetic iron oxides nanoparticles and cobalt oxyhydrite cores by Allen et al.^{95,96}

2. THE FERRITIN PROTEIN SHELL AS MULTIVALENT SCAFFOLD

As a consequence of the regular assembly of the protein subunits, binding sites and reactive groups on the surface of the complexes are arranged in a geometrically well-defined manner. The distances of functional groups in dendrimers or multiple antigen peptides are basically defined by steric or electrostatic repulsion, but protein complexes provide a well-defined, rigid scaffold of which the structure can be known to atomic resolution. Polyvalent scaffolds as carrier of medically important antigenic determinants are promising candidates in the development of potent antibiotics and novel effective inactive vaccines.^{97,98} Defined structural constraints are important for immunogenicity.⁹⁹ Thus, particularly virus-like particles exhibit

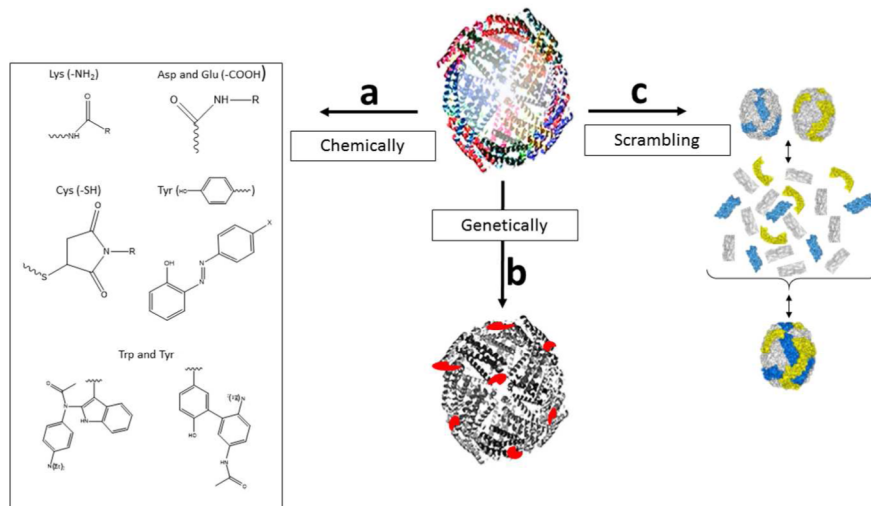


Figure 5. Ferritin can be modified via chemistry (a) or using genetic (b) modification. Ferritins having different modifications can also be easily combined because of the reversible disassembly/reassembly process (c). This also allows for the preparation of more complex and multifunctional bionanoparticles.

strong immunogenic properties.¹⁰⁰ The well-defined structure and behavior of ferritin make it an excellent particle to be modified on various levels, for example, synthetically or genetically, but also combinations of various modifications are easily accessible (Figure 5).

An early work on chemical derivatization of the outer shell of ferritin was reported by Danon et al.¹⁰¹ Searching for biocompatible cationic labels for transmission electron microscopy, they blocked the free carboxylic groups of ferritin by carbodiimide-mediated reaction with *N,N*-dimethyl 1,3-diaminopropane. Decreasing the pH led to a higher degree of carboxyl-modification (559 carboxyl groups present), that is, higher positive net charge on the ferritin ("cationic ferritin"). Cells that were treated with cationized ferritin showed different labeling densities with ferritin, reflecting the respective cell surface charge. A precise analysis of the chemical composition of the modified ferritin was not presented. This is an early example of an engineered bionanoparticle where the advantages of the inorganic core (contrast in electron microscopy) were combined with the advantages of the functional organic shell (modification to cationic surface charge). Recently, an exciting observation with cationized ferritin was reported by Mann and co-workers. They complexed cationized ferritin electrostatically with an anionic polymer surfactant, poly(ethylene glycol) 4-nonylphenyl 3-sulfopropyl ether.^{102,103} Approximately 240 *N,N*'-dimethyl-1,3-propanediamine (DMPA) groups were covalently coupled, and approximately 264 anionic polymer surfactants were electrostatically bound to each ferritin. After extensive dialysis, lyophilization, and annealing of the solid to 50 °C, a red liquid was obtained, which remained fluid upon cooling to room temperature. While the cationized ferritin-surfactant liquid showed at 50 °C Newtonian fluid behavior, the samples transformed after a few hours at 32 °C to a viscoelastic liquid with the typical Maltese cross texture of a smectic liquid crystalline phase. The onset of the protein fluidity ("liquid protein") was explained with an increase of the range of the intermolecular forces to length scales of the protein structures and thus to be commensurate with fluid behavior.¹⁰² The observed anisotropy is harder to explain. The anisotropic distribution of the H- and L-chains in the protein shell of ferritin can lead upon cationization and electrostatic con-

jugation to anisotropic particles as a statistic evaluation of AFM images of a large number of single particles indicated.

Wetz and Crichton modified ferritin with different labels to establish the number of accessible functional groups in the interior of ferritin, apoferritin, and on the disassembled protein shell.¹⁰⁴ They found that one sulphhydryl, three amino, and seven carboxyl groups could be modified per subunit of ferritin. In apoferritin, one amino group and four carboxyl moieties are additionally accessible, which can be blocked resulting in efficient inhibition of the iron uptake in core reconstitution experiments. A number of 4–5 lysine residues and 11 carboxyl moieties are additionally accessible in disassembled ferritin, which was supposed to be involved in intersubunit interactions. In a similar approach, based on the chemical reactivity of different labels toward the cysteine sulphydryl groups at positions 52 and 130, no clear conclusions for the biochemical mechanism for the reaction could be drawn.¹⁰⁵

Aqueous solutions are the natural environment of proteins. However, for many applications, it would be advantageous to transfer them to organic solvents. This would significantly broaden the number of synthetic routes and accessible composite materials. Success is often hampered by the irreversible destruction of the secondary and tertiary structures of the protein (denaturation). Wong et al. derivatized the ferritin protein shell with long alkyl chains and obtained fully organic-soluble hydrophobic particles ("hydrophobic ferritin").^{106,107} Efficient coupling of primary alkyl amines was achieved in water/THF, water/ethanol, or water/methanol mixtures after carbodiimide activation of surface exposed carboxyl groups. Low solubility of the longer-chain tetradecylamine or stearylamine led to limited long-term stability and slow precipitation. Although the excess amines impose problems for an unambiguous characterization, they estimated from sedimentation analysis an average number of 400 covalently bound nonylamine molecules per ferritin particle. The C₉-, C₁₂-, and C₁₄-alkylated proteins could be readily extracted into dichloromethane by addition of small amounts of sodium chloride to the aqueous phase. The successful extraction could be followed by the color change of the phase containing the orange-brown ferritin particles. The possibility of surfactant micellization of ferritin particles and

transfer to the organic medium was ruled out in control experiments, although a significant amount of physically bound alkylamines on alkylated ferritin must be assumed. Correspondingly, derivatized ferritin did only migrate under reverse polarity in non-denaturing PAGE. TEM proved that the ferritin core remained well-separated and nonaggregated upon alkylation and transfer/back-transfer between the aqueous and organic phase. The specimen did not stain well with uranyl-acetate, presumably a result of the significantly different surface properties of modified ferritin. Most importantly, the modified protein shell exhibited a remarkable difference toward mineralization: No ferrihydrite core was formed upon incubation with iron(II) solutions. Alkylated ferritin was, for example, used to prepare ferritin–polymer composites (see below).¹⁰⁸

Sengonul et al. have chosen another way to render the ferritin particles soluble in organic solvents or polymeric matrixes.¹⁰⁹ They modified ferritin with short polyethyleneglycol chains (750 g/mol) or alkyl groups by using the synthetic protocol developed by Wong et al. The PEG-ylated or alkylated ferritin particles retained on a cation exchange column and eluted only after slow increase of the NaCl concentration, indicating its reversed charge. Zeta-potential measurements gave a value for the isoelectric point of pI 8.0, in line with the mentioned elution behavior. The modified particles could readily be extracted into dichloromethane and remained stable in solution. The dispersion in polymer blends showed a preferential distribution of the PEG-ylated ferritin in the minor PEG phase and of the alkylated ferritin into the major phase of a hydrophobic polymer. Although significant flocculation of the particles in their respective host phase was observed, it should be possible to optimize the polymer/ferritin system. The self-directing and -assembling character of nanoparticle/polymer systems is not yet explored in greater detail, but promising new nanostructure composite materials and films can be expected. Ferritin as a carrier of biological function and as a host of various inorganic materials can be an interesting building block for such systems.

PEGylation of proteins changes their properties dramatically; thus, in further attempts, PEG-chains of different molecular weights were conjugated.¹¹⁰ While PEG-labeled virus precipitated in solution during conjugation with high concentrations of PEG or longer polymers than PEG-5000, ferritin remained stable in solution. The differential estimation of the reaction of PEG-ylated ferritin with the fluorescent dye FITC yielded grafting numbers between 20 and 30; the considerable lower number as compared to reaction with biotin (72) might be due to steric hindrance. Indeed, DLS showed a strong increase of the diameter for PEG-ylated ferritins with increasing PEG chain length. PEGylation enabled ferritin to remain mobile upon adsorption onto surfaces and thus able to form more regular assemblies (see below).

Wang and co-workers were the first who did a rigorous and encompassing evaluation of the reactivity and accessibility of functional groups on the empty protein cage of horse spleen ferritin.^{111,112} They used surface exposed lysine amino groups for chemo-selective derivatization of the ferritin protein shell. After digestion, a detailed proteomics analysis was conducted with MALDI-TOF mass spectrometry. By reaction with small reagents, four lysine residues of each apoferritin subunit could be derivatized at a time, K83, K97, K104, and K143. Larger reagents like 5-carboxyfluorescein (FL) N-hydroxysuccinimidyl (NHS) ester react with K83, K97, and K143, but not with

K104. The UV-analysis of reaction mixtures with increasing concentration of reactive dye showed that the number of dye molecules attached per apoferritin particle reached a plateau at approximately 22–24. This indicates that only one lysine residue was conjugated with FL-NHS at a time that was confirmed by MALDI-TOF MS-analysis. Presumably, steric crowding prevented multiple reactions on one subunit as soon as one lysine residue was labeled. The click-reaction between alkyne-functionalized ferritin and an azide-bearing coumarin-derivative was in accordance with this conclusion: all four derivatized lysine moieties on a subunit were accessed but only one on the same subunit (Figure 6). The fluorogenic properties

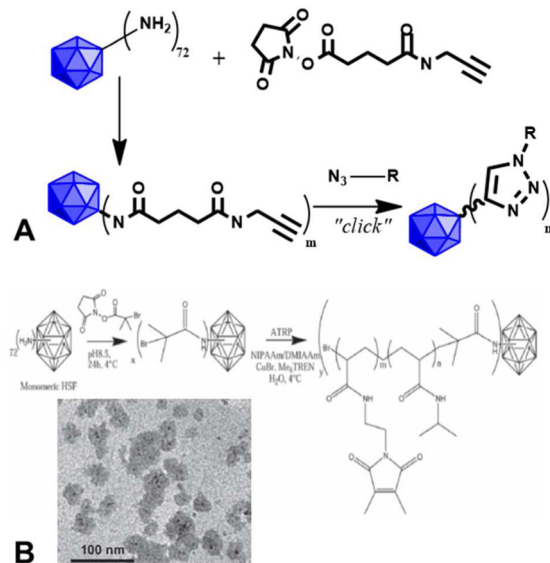


Figure 6. Procedure for the addition of small molecular components onto the ferritin via the surface available lysine-residues and an activated carboxylic acid. The added molecular component can function as a platform for further modification via (A) a click-reaction as described in ref 112 or via (B) a polymerization reaction like atom transfer radical polymerization (ATRP). TEM-image displays the ferritin particles with a polymer corona. Reprinted with permission from ref 114. Copyright 2011 Wiley-VCH.

of the click-reaction could be conveniently used to follow the reaction by fluorescence and UV-vis spectroscopy. A detailed mass-spectrometry analysis of the intact and the digest of labeled apoferritin confirmed the four lysine moieties as reaction sites.

After functionalization of the protein shell with bromoisobutyl NHS-ester, derivatized HSF could be used as multivalent initiator in grafting-from polymerizations.¹¹² A hydrogel consisting of polymer-grafted ferritin particles was obtained from the radical polymerization of water-soluble polyethyleneglycol methacrylate as well as poly-N-isopropylacrylamide (PNIPAAm) in another study by Böker and co-workers.^{113,114} The PEG-modified ferritin could be dissolved in excess H₂O as well as in dichloromethane. The PNIPAAm-polymer-grafted particles aggregated and adsorbed strongly at polar–polar interfaces (more details in section 4), and the hybrid particles had the same temperature hysteresis as is known for PNIPAAm.

The close proximity of lysine amino groups on the same subunit was also shown by fluorescence resonance energy transfer (FRET) experiments.¹¹⁵ Only if an average of more

than approximately 24 dye molecules were introduced on one ferritin shell, that is, if two different dyes are both on one subunit, did efficient FRET occur. The authors proved their hypothesis of dual-labeling in a number of control experiments without conducting a proteome analysis. First evidence was the unchanged FRET signature for dissociated ferritin particles; that is, both fluorophores must have been on the same subunit. Reassembled particles from a 1:1 mixture of ferritin subunits that have been separately labeled with only one sort of dye did not show FRET; if, however, the reassembled particle was labeled in a second reaction, FRET was observed (Figure 7).

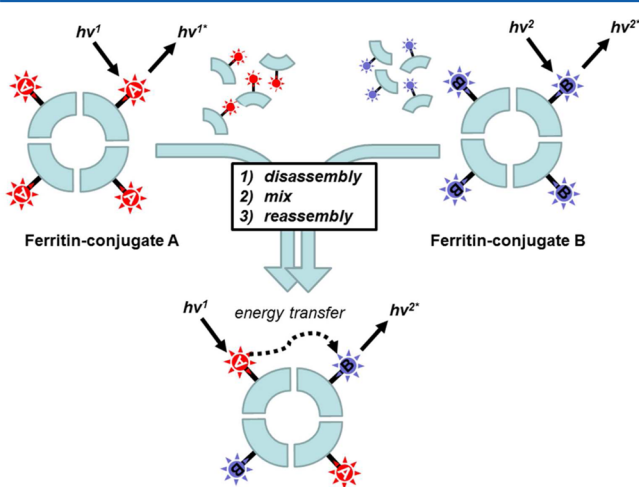


Figure 7. Dissociation into subunits of labeled ferritin-A or ferritin-B (fluorophores with complementary spectroscopic properties) followed by reassembly of the subunits from the mixture. Blue and red subunits represent the complementary-labeled apoferritin subunits. Upon mixing, the complementary fluorophores are close enough to undergo energy transfer. Process is described in ref 115.

The FRET efficiency was governed by the ratio of the two covalently bound dyes. That means that by controlling the labeling ratio, the fluorescence emission of the FRET ferritin samples could be tuned.

In other research works, also vinyl sulfone reactive dyes were conjugated to ferritin, yielding fully intact particles each modified with 20–40 dyes.¹¹⁶ Modification of sulfhydryl groups with Traut's reagent (2-iminothiolane hydrochloride) has also been reported.¹¹⁷

3. SYNTHESIS OF NANOPHASE (IN)ORGANIC MATERIALS IN THE FERRITIN PROTEIN CAGE

Ferritin with its unique cavity is able to house many different inorganic materials. The highly functional protein surface in combination with technologically interesting inorganic cores yields valuable composite bioinorganic building blocks. Their monodisperse nature facilitates the formation of regular arrays and assemblies. Because the electronic, optical, or magnetic properties of nanoparticles depend strongly on particle size and shape, the control over these aspects is important. The apoferritin cage provides a viable template for the size-controlled synthesis and advantageously renders the cores water-soluble and biocompatible. Biocompatible, functional nanoparticles are expected to have many applications in medicine and diagnostics, in chemistry, or in electronics, for example, as fluorescent markers, drug delivery systems, catalysts, and in data storage and quantum electronics, respectively. Because of the channels inside the protein cage but also the ability of the cage to reversibly disassemble and reassemble, many species can be incorporated into the core. In the case of small species not interacting with the shell or channel, they are able to diffuse uninhibited (Figure 8). However, when species become too large or are expelled by the channel due to charge repulsion, diffusion is not possible. Still these are able to be incorporated via the disassembly/reassembly process (Figure 8). The amount able to be incorporated depends then on size and concentration as well as specific favorable interaction with the inner part of the protein shell. Various inclusion approaches and functional systems will be discussed in this section.

When in the beginning of the 1990s research was focusing on the preparation of well-defined nanoparticles, Mann and Meldrum were the first who made use of the cage structure of ferritin as a size-constrained reaction vessel.^{118,119} Although the binding of metal-ions to ferritin has already been explored earlier, the interest now went well beyond the understanding of biominerization using the ferritin as a bionanoreactor for the production and encapsulation of new inorganic nanosized structures of different materials. Today, a large number of minerals, among them technologically interesting semiconductor nanoparticles, and metal or metal alloy nanoparticles have been formed within the apoferritin cavity (Table 1, section 3.2).^{120,121}

Two approaches have been followed mainly: either reassembly of the protein cage from the subunits in the presence of the material that should be encapsulated⁶² or incubation of the empty and intact apoferitin with the respective metal ions (Figure 9).¹²² Both approaches have

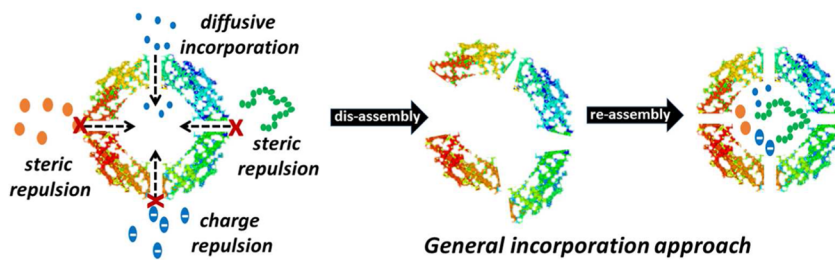


Figure 8. Uninhibited flow from the medium into the empty ferritin cage is only possible for small species that are small enough to pass through the channels but also do not interact with the inside of the channels. For the loading of species not capable of passing through the channel due to, for example, steric repulsion or charge repulsion, the disassembly/reassembly process is required.

Table 1. Various Ionic and Organic Complexes Formed within the Cavity of Ferritin and Ferritin-Like Cage Proteins

incorporated					
ions	reactants	protein cage	inclusion mechanism	ref	
Eu ³⁺	EuCl ₃	HSAF(m) (BCCP–ferritin)	reassembly of biotin carboxyl carrier protein	138	
Cu ²⁺	CuSO ₄	HSF	diffusion	69	
		HSAF		69	
Co ²⁺	CoCl ₂	Fmfer(m)	diffusion	57	
		HSF		69	
		HSAF		69	
Mg ²⁺	CoSO ₄	HSAF		69	
	MgCl ₂	Fmfer(m)	diffusion	57	
		HSF		69	
		HSAF		69	
Mn ²⁺	MgSO ₄	HSAF		69	
	MnSO ₄	HSF	diffusion	69	
		HSAF		69	
Gd ³⁺	GdHPDO ₃ A	HSAF	reassembly		
Ni ²⁺	NiSO ₄	HSF	diffusion	69	
		HSAF		69	
Fe ²⁺	FeSO ₄	HSF	diffusion	69	
		HSAF		69	
	FeSO ₄ or FeCl ₂	HSAF		70	
Cd ²⁺	CdSO ₄	HSF	diffusion	69	
		HSAF		69	
Zn ²⁺	ZnSO ₄	HSF	diffusion	69	
		HSAF		69	
organics/organic complex	reactants	protein cage	inclusion mechanism	ref	
ferrocene	ferrocene derivatives	RLcHSAF	diffusion	130	
fluorescein	fluorescein sodium salts fluorescein-5-maleimide/5-(and 6-) carboxy-fluorescein-succinimidyl ester	HSAF	reassembly	132	
		Hsp-Mj(m)		133	
hexacyanoferrate	K ₃ Fe(CN) ₆	HSAF	reassembly	77	
				132	
				133	
neutral red	neutral red	HSF	reassembly	62	
phenophthalein	phenophthalein	HSF	reassembly	62	
Prussian Blue (CuFe)	CuSO ₄ ·5H ₂ O K ₃ [Fe(CN) ₆]	HSAF	reassembly + diffusion	124	
Prussian Blue	Fe(CN) ₆ ³⁻	HSF		185	
methylene blue	methylene blue	HSF	reassembly	125	
	methylene blue	HSF	reassembly	126	
halothane	halothane	HSAF HSF (with core)	intersubunit binding	186	
isoflurane	isoflurane	HSF	intersubunit binding	186	
		HSF (with core)			
cisplatin	K ₂ PtCl ₄ cisplatin	HSF	reassembly	128	
carboplatin	K ₂ PtCl ₄ carboplatin	HSF	reassembly	129	
oxaliplatin	oxaliplatin	HSF	reassembly	129	
Ru- <i>p</i> -cumene	[Ru(<i>p</i> -cymene)Cl ₂] ₂	RLcHSAF	diffusion	187	
doxorubicin	(6-maleimidocaproyl) hydrazone derivative of doxorubicin	Hsp-Mj(m)	diffusion	78	
Pd-allyl-Cl ₂	[Pd(allyl)Cl] ₂	RLcHSAF	diffusion	188	
				189	
	[Pd(allyl)Cl] ₂	RLcHSAF(m)		190	

been extensively employed for the synthesis of ferritin encapsulated materials during the past few years. The latter approach is restricted to molecules and ions that are able to penetrate the protein shell, that is, which are sterically and electronically able to pass one of the channels in the protein shell.

3.1. Encapsulation of Molecules and Ionic Species in the Interior of Ferritin

Approaches to encapsulate bulky molecules and ionic species (tabulated in Table 1) in the interior of apoferritin followed the observation of Webb that apoferritin can be reversible disassociated and reassociated by simple adjustment of the pH to pH 2 or above pH 7, respectively.⁶² Once trapped, the tracer molecules, for example, neutral red, were efficiently sequestered in the protein cage if they are too large to escape

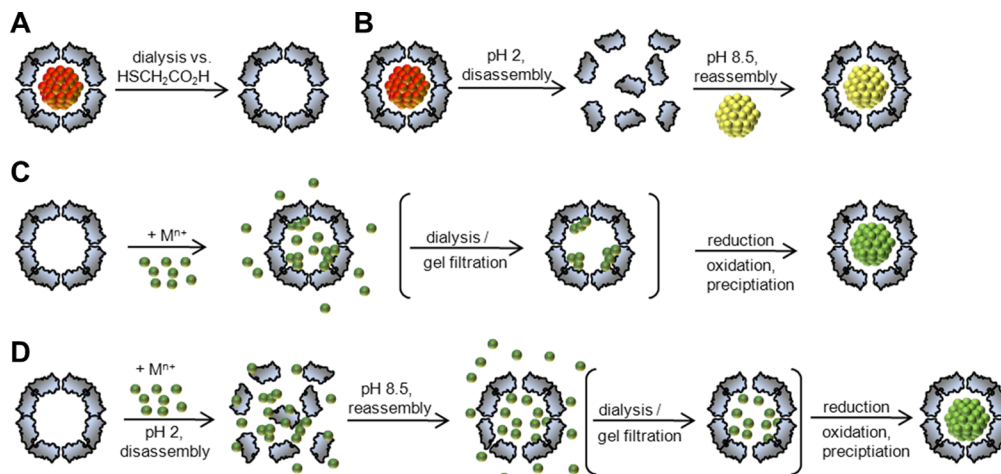


Figure 9. Schematic representation of different approaches for the removal of the inner core of ferritin (a,b) and the possible routes for the incorporation of new synthetic cores (b–d). The two main approaches consist of using the pores inside the ferritin shell to transport ions that are dissolved from the core or condensed upon particle formation or completely disassemble the ferritin shell and reassemble it in the presence of the desired species to be encapsulated. Reprinted with permission from ref 1. Copyright 2011 Elsevier.

through one of the two types of channels in the shell. Webb et al. gave a rough estimation of the internal volume of 1.4×10^{-19} cm³ that can hold solubilized species, which would mean that on average 8.7 small molecules of neutral red could be entrapped if the cavity has been reconstituted in a 0.1 M neutral red solution.⁶² They found 4 molecules per ferritin, determined by UV-vis spectroscopy, which is in reasonable agreement with what was expected. The number of entrapped solutes corresponded to the number in an equivalent free volume. By different careful purification procedures and control experiments, Webb could rule out unspecific binding of the tracer to the outer protein shell surface. However, a general rule of which molecules will be sequestered could not be identified.

Dominguez-Vera and co-workers used this strategy for the encapsulation of bulky ionic complexes inside the ferritin cavity. They sequestered hexacyanoferrate(III) within the apoferritin cage through rise of the pH from 2.0 to 8.5 (Figure 10).¹²³ After removal of non-compartmentalized hexacyanoferrate(III) by extensive dialysis, the addition of Fe(II) resulted in the formation of Prussian Blue complexes within the protein cage.

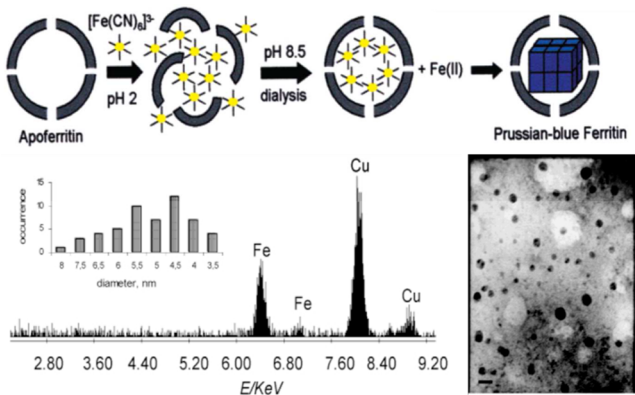


Figure 10. Schematic representation of pH-induced disassembly/reassembly of apoferritin in the presence of hexacyanoferrate(III) after reacting with iron(II); Prussian Blue is formed within the apoferritin cavity. Below are shown the EDXA and TEM images of the respective particles. Reprinted with permission from ref 123. Copyright 2003 American Chemical Society.

TEM and EDX analysis showed the formation of round discrete particles consisting of iron; however, the sizes were broadly distributed, which does not point to the formation of well-ordered crystalline particles but to the formation of a “Prussian-Blue–ferritin complex”.

In another study, the size-exclusion properties of the protein channels in the shell were nicely demonstrated.¹²⁴ Cu(II)-ions were bound inside the protein cavity after incubation with CuSO₄ and subsequent dialysis. The approximately 225 encapsulated Cu(II)-ions were efficiently sequestered from Fe(CN)₆³⁻ ions in the bulk solution, and no formation of Cu–Fe–Prussian Blue complexes occurred. This result ruled out also the binding of Cu(II) to the external surface of apoferritin. The bulky hexacyanoferrate(III)-ion with a size of 0.6 nm could be guided through the channels only in the presence of urea. Urea acts as a softener and induces an opening of the channels but does not disassemble the protein cage. On the other hand, small molecules like NaBH₄ could penetrate the channels and reduce the entrapped copper or palladium ions to metallic nanoparticles.^{61,124} Oxidation to Cu₂O can be induced if the Cu-apoferritin solution is exposed to air and the characteristic plasmon excitation of Cu at 570 nm vanishes.

Of special interest is the encapsulation of clinical relevant, either diagnostic or therapeutic, agents because the biocompatible and/or functional shell helps in efficient protection and targeted delivery of ions, complexes, or organic compounds. The disassembly/reassembly process is the only suitable way to introduce bulky molecules. In this way, Yan et al. showed the entrapment of methylene blue inside the apoferritin cage (approximately one molecule/protein cage) for photodynamic therapy.^{125,126} In that procedure, a photosensitizing agent induces the production of cytotoxic singlet oxygen with the aid of light. The photosensitizer methylene blue dye showed a reduced rate of singlet oxygen production as compared to free dye; however, it was proposed that the protein shell can protect the methylene blue from further metabolic reactions, which led to its quick deactivation *in vivo*. The cytotoxic activity of the drug loaded apoferritin was shown *in vitro* using a two color fluorescence cell viability test.

Aime et al. prepared via the disassembly/reassembly route gadolinium(III)-loaded apoferritin.¹²⁷ The development of

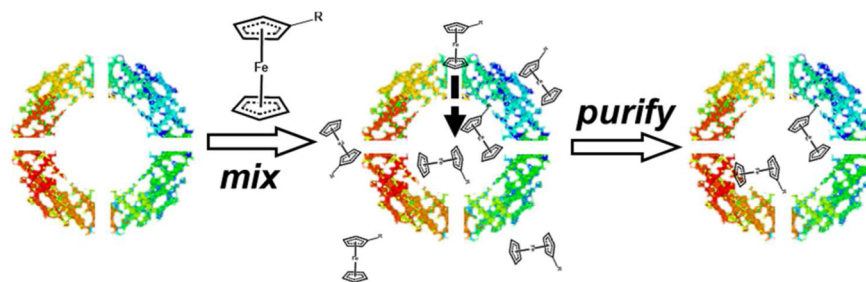


Figure 11. Electrochemical active ferritin via inclusion of ferrocene into the cavity via incubation and washing as described in ref 130.

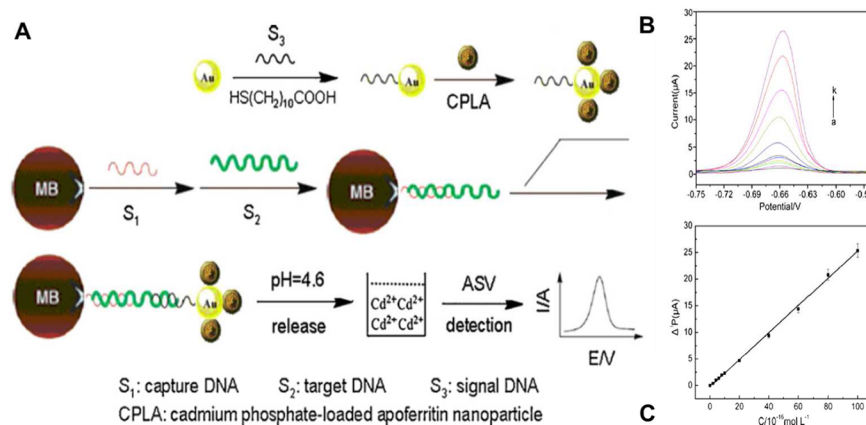


Figure 12. Electrochemical detection of DNA hybridization based on signal DNA probe modified with Au and apo ferritin nanoparticles. (A) Schematic diagram for the biosensor fabrication. (B) ASV of Cd²⁺ and (C) calibration curve for the detection of DNA sequences. The concentrations of target DNA: (a) 0 M, (b) 2 × 10⁻¹⁶ M, (c) 4 × 10⁻¹⁶ M, (d) 6 × 10⁻¹⁶ M, (e) 8 × 10⁻¹⁶ M, (f) 1 × 10⁻¹⁵ M, (g) 2 × 10⁻¹⁵ M, (h) 4 × 10⁻¹⁵ M, (i) 6 × 10⁻¹⁵ M, (j) 8 × 10⁻¹⁵ M, and (k) 1 × 10⁻¹⁴ M. Reprinted with permission from ref 134. Copyright 2010 Elsevier.

paramagnetic contrast agents for magnetic resonance imaging focused on highly stable Gd(III)-chelates, which exhibit a high magnetic moment and long relaxation times due to their seven unpaired electrons. The microenvironment of the chelate strongly influences the relaxivity. A pronounced effect was observed if Gd-complexes were bound to proteins. Aime et al. entrapped a gadolinium(III) chelate within the apoferritin cavity by adjusting the pH of a mixture of the protein subunits and gadolinium complex from pH 2 to 7. The relaxivity increased 20 times as compared to free complexes in aqueous solution. The constraining protein shell allowed multiple interaction pathways yielding a highly relaxing sink. The effective entrapment was proven by different control experiments; further, the authors ruled out that the Gd-complex disassociated upon entrapment.

Cisplatin and carboplatin, two potent anticancer drugs, were entrapped by the disassembly reassembly route.^{128,129} The loading efficiency in the initial experiments was very low (two and five molecules, respectively, per apoferritin cage), while the in situ method allowed the incorporation of a much higher number of platinum complexes.¹²⁸ After incubation with K₂PtCl₄ at pH 8.5, ammonia buffer was added. In this way, a mixture of *cis*-platin and inactive, nontoxic *trans*-platin was generated. However, improved synthesis enabled the loading of up to 45 ± 4 cisplatin or 17 ± 1 carboplatin complexes per apoferritin particle via the disassembly reassembly route.¹²⁹ The cytotoxic activity of the systems was shown against the rat pheochromocytoma cell line. At the same Pt concentration, the apoferritin encapsulated drugs had pronounced less cytotoxicity than the pure platinum compounds. On the other hand, the cellular uptake of the ferritin systems was

higher than for the pure drugs, a significant result for defeating cisplatin resistance. Binding sites and endocytosis of ferritin are responsible for an increased uptake by tumor cells, which overexpress ferritin receptors. The cellular viability was monitored as a first test of the pharmacokinetic properties. Cells almost died completely after 48 h with cisplatin, while the apoferritin system shows much milder and slower effects because the enclosed cisplatin is only slowly released.¹²⁹ The particles did not leak, as the Pt content of the loaded apoferritin did not change, and thus the release mechanism is not yet clear under *in vitro* or *in vivo* applications.

For the binding and entrapment of three different ferrocene derivatives, only the *in situ* method was considered. It was shown with UV-vis spectroscopy, ICP-OES spectroscopy, and protein content analysis that the incorporation of ferrocene varies with subtle differences in substitution patterns of the ferrocene (Figure 11).¹³⁰ The structure of the ferrocene derivatives within the protein shell could not be determined by X-ray analysis. However, an anomalous Fourier difference map calculation located an iron at the 2-fold symmetry axis of the apoferritin shell. This binding site was also found by Eckenhoff et al. for molecules like halothane and isoflurane.¹³¹ The electrochemical analysis of the entrapped ferrocene revealed a constant shift of approximately +8 mV as compared to free dimethylamine-substituted ferrocene derivatives, indicating a more hydrophobic surrounding.

The multifunctional protein cage of ferritin can be used as an advantageous marker for protein assays. Loading of the cage with multiple signaling moieties and labeling with different binding functionalities can give rise to multiple interactions and enhanced detection levels. Liu et al. encapsulated fluorescein or

hexacyanoferrate to produce ferritin-based optical or electrochemical markers.^{132,133} The loading was dependent on the marker concentration in the entrapment solution. A maximum loading of 65 of the fluorescent or 150 of the redox marker with the disassembly reassembly route was obtained, more than was expected from calculation on the basis of molecular volumes, which points toward specific interactions of the marker molecules in the cavity with the protein shell and/or themselves. The use of the biotin-functionalized ferritin labels for biosensing and assay purposes was studied in a classical immune-sandwich assay with fluorescence microscopy or in a magnetic bead-based sandwich hybridization assay with voltammetry, after release of the hexacyanoferrate. The detection limits of 0.06 and 0.08 ng/mL, respectively, were much lower than that of a colorimetric protein assay.¹³² Hexacyanoferrate-loaded ferritin, which was tagged with about eight signal DNA probes for a dual hybridization assay with magnetic bead separation, allowed detection levels as low as 3 ng/L of target DNA by electrochemical quantification of hexacyanoferrate(III) released.¹³³ The assay was further developed by using signal DNA tagged gold nanoparticles, which were conjugated cadmium phosphate loaded apoferritin nanoparticles (Figure 12). After release of the cadmium ions at pH 4.6 from the ferritin protein cage, the electrochemical detection limit was as low as 5×10^{-17} M.¹³⁴

Loading multiple markers makes it possible to construct a molecular marker library and extend the concept to multiplex assays. This could be achieved by the loading of apoferritin with any predetermined mixture of ions by the disassembly reassembly process and the convenient preparation of encoded particles for multiplexed electrochemical biosensors or -assays.^{135,136} Increasing the pH of the phosphate buffered solution with the metal ions triggered first the reassembly of the protein cage and then the precipitation of metal-phosphates. Thereby, it is critical to approach pH 5 slowly. The preferential formation of mineral cores over precipitation in solution was explained by the preferred initial interaction of ions with the subunits of the apoferritin and the autocatalytic growth after the formation of critical nuclei on the inside of the assembled protein cage.¹³⁵ Upon dissolution of the metal phosphate particles from the apoferritin cage under mild acidic conditions, the released ions generate a distinct voltammetric pattern. The composition ion ratio of the nanoparticle cores was determined by the initial ion concentrations, and the cores were formed with high precision and uniformity. Thus, a large number of encoding patterns can be accomplished by simple adjustment of the ionic composition; moreover, as several ions can be detected in parallel with baseline separated peaks in stripping voltammetry, several thousands of bar code patterns with distinct electrochemical signatures can be achieved. It must be pointed out that the approach via the diffusion method did not allow for the preparation of ferritin particles with uniform and structurally and compositionally defined mineral cores with mixed ions because of the different interactions of the metal ions with the capsids' interior and following catalytic kinetics of mineral deposition. However, in an earlier report, the diffusion method was used to construct ultrasensitive labels consisting of cadmium phosphate containing ferritin, which was modified with biotin-NHS.¹³⁶ In a classical sandwich immunoassay, the antigen was linked via biotin-modified antibodies to avidin-modified magnetic beads and the ferritin labels. After capture of the substrate, labeling, and separation, the release of cadmium ions from the ferritin capsid could be induced under mild acidic

conditions. The free cadmium ions could be electrically detected. The extrapolated detection limit was 2 pg/mL for the tested tumor necrosis factor alpha. The principal proof of feasibility for multiple parallel electrochemical detection was given by the mixed assay of TNF-alpha and MCP-1 with cadmium and led phosphate loaded apoferritin particles, which were functionalized with the respective antibodies.¹³⁶

Encapsulated europium(III)-ions can be used as labels for time-resolved fluorometry. Virta and co-workers fused the biotin-containing domain of biotin carboxyl carrier protein to the amino-terminal end of ferritin subunits, which are exposed on the outer surface of the protein shell.^{137,138} After expression in *E. coli*, ferritin fusion protein particles could be successfully reassembled from the dissolved inclusion bodies in the presence of Eu³⁺ by raising the pH. Generally, loadings between 20 and 150 (average 30) Eu³⁺-ions were achieved.¹³⁸ The addition of the strong Eu³⁺-chelating ligand could leach only small amounts from freshly Eu³⁺-loaded ferritin, indicating that most of the Eu³⁺-ions were tightly attached to the inner surface of the protein shell. The production process for different engineered ferritin particles was investigated in detail. Urea- and pH-induced refolding, various pH refolding conditions, and additives like glutathione or L-arginine were tested for their effect on the particle yield.¹³⁹ The simple preparation of multivalent affinity labels by bacterial fermentation and nonchromatographic workup of the inclusion bodies, which can be directly loaded during refolding with many different inorganic compounds, constitutes a clear advantage. Other functional bioinorganic nanoparticle labels need more elaborate synthesis and functionalization to introduce useful binding and signaling moieties and to render them biocompatible.

3.2. Synthesis of Inorganic Cores in the Protein Cage of Ferritin

Although the ferroxidase subunit has vital regulatory functions for iron sequestration in vivo, genetic engineered HSF showed that precipitation of ferrihydrite also occurs in the absence of the ferroxidase center. Moreover, the examples for all nonferroxidase substrates or mineralization reactions, which are not specifically protein-assisted, indicate that the spatial selectivity is at least partially controlled by charged nucleation sites at the protein interface or controlled by the size of the material that should be entrapped. The accessibility of the interior is restricted by the size of the hydrophilic channels in the protein cage. The pores can be widened by, for example, urea.⁴¹ Although protein cages have a robust structure, the synthesis conditions have to be mild, which is a challenge.

The nucleation on the internal surface of the protein cavity is triggered by the metal-ion binding capacity of negatively charged amino acids. The catalytic intracavity oxidation to highly oxidized ions increases the local supersaturation further and triggers the precipitation of inorganic cores. The formation of native ferrihydrite cores is a combination of the protein-facilitated redox activity and inorganic nucleation. This principle also works best for other transition-metal materials. Other routes are the reduction of metal ions and complexes to metal and metal alloys, nonredox hydrolysis reactions to form hydrated oxides and hydroxides, or slow coprecipitation routes. These routes with non-natural mechanisms are most often compromised by nonspecific bulk precipitation. A careful control of reaction rates through reagent concentrations, pH, specific binding ligands, or triggers is necessary.

Table 2. Various Inorganic As Well As Organic Complexes Formed within the Cavity of Ferritin and Ferritin-Like Cage Proteins^a

incorporated					ref
metals/alloys	reactants	protein cage	particle-forming chemical		ref
Pd ⁰	K ₂ PdCl ₄ K ₂ PdCl ₄	HSAF HSF	NaBH ₄ NaBH ₄		155 61
Cu ⁰	CuSO ₄ ·5H ₂ O CuSO ₄	HSAF HSAF	NaBH ₄ NaBH ₄		124 156
Co ⁰	Co ²⁺	HSAF	NaBH ₄		157
Ni ⁰	Ni ²⁺	HSAF	NaBH ₄		157
Au ⁰	HAuCl ₄ AuNP HAuCl ₄	HSAF RLcHSAF9(m)	NaBH ₄ or MOPS gold binding peptide: MHGKTQATSGTIQS/reassembly (1) NaBH ₄ ; (2) ascorbic acid		158 159 160
Ag ⁰	AgNO ₃	HSAF HSAF(m) PfFt	NaBH ₄ AG4 peptide (-Asn-Pro-Ser-Ser-Leu-Phe-Arg-Tyr-Leu-Pro-Ser-Asp-) NaBH ₄		161 15 87
Pd ⁰ /Au ⁰ (alloy)	Au _{core} Pd _{shell}	KAuCl ₄ /KPdCl ₄	RLcHSAF	NaBH ₄	162
Ag ⁰ /Au ⁰	AgNO ₃ /HAuCl ₄	HSAF	NaBH ₄		163
Pt ⁰	K ₂ PtCl ₄ K ₂ PtCl ₄ K ₂ PtCl ₄ PtCl ₄ ²⁻ (65 °C)	LiDps HSAF HSAF Hsp-Mj	sodium citrate(UV) NaBH ₄ NaBH ₄ (CH ₃) ₂ NBH ₃		164 60 165 79
Co ⁰ Pt ⁰	(NH ₄) ₂ Fe(SO ₄) ₂ and K ₂ PtCl ₄ Co(NO ₃) ₂ ·6H ₂ O and K ₂ PtCl ₄	RPfFer	NaBH ₄		144
metalloxide-deriv.	reactants	protein cage	particle-forming chemical		ref
FeOOH	(NH ₄) ₂ Fe(SO ₄) ₂	BacterA-PfFer	air		84
Fe ₃ O ₄	(NH ₄) ₂ Fe(SO ₄) ₂ (NH ₄) ₂ Fe(SO ₄) ₂	RhcHfer	H ₂ O ₂		153
U(O)OH	UO ₂ (Oac) ₂	HSF	air, 600 °C		150
Mn(O)OH	MnCl ₂	HSF	air		119
β-MnOOH	MnCl ₂	HSAF	air		166
αMnOOH/Mn ₃ O ₄	MnCl ₂ ·4H ₂ O	HSF	air		148
MnOOH	MnCl ₂ ·4H ₂ O	HSF	air		119
Co ₃ O ₄	Co(NO ₃) ₂ ·6H ₂ O	fip-Li	H ₂ O ₂ , 65 °C		96
Co(O)OH	Co(NO ₃) ₂ CoSO ₄	HSF	H ₂ O ₂		167
Ni(OH) ₂	NiSO ₄ Ni(NO ₃) ₂ NiCl ₂ NiSO ₄ Ni(NO ₃) ₂ NiCl ₂	HSAF(m)	CO ₂ ; Na ₂ CO ₃		166 168
Cr(OH) ₂	(NH ₄) ₂ Cr(SO ₄) ₂	HSAF	CO ₂		168
Fe(O)OH	Fe ³⁺ -citrate	Mfer	O ₂ /light		169
Eu(O)OH	Eu ³⁺ -citrate	Mfer	O ₂ /light		169
Ti(O)OH	Ti ⁴⁺ -citrate	Mfer	O ₂ /light		169
Gd ₂ O ₃	Gd(NO ₃) ₃ ·6H ₂ O	HSF			170
CeO ₂	CeCl ₃ ·7H ₂ O	RLcHSAF	air		171
Cu ₀ -FeO(OH)	(NH ₄) ₂ Fe(SO ₄) ₂ CuSO ₄ ·5H ₂ O	HSF	sodium citrate or potassium sodium tartrate (UV)/UV		172
γ-Fe ₂ O ₃	(NH ₄) ₂ Fe(SO ₄) ₂ (NH ₄) ₂ Fe(SO ₄) ₂ (NH ₄) ₂ Fe(SO ₄) ₂	Fip-Li LiDps(m) PfFer	H ₂ O ₂ H ₂ O ₂ H ₂ O ₂		95 173 85
α-Fe ₂ O ₃	(NH ₄) ₂ Fe(SO ₄) ₂	PfFer	Na-oxalate, 97 °C		86
Fe ₃ O ₄ -γ-Fe ₂ O ₃	(NH ₄) ₂ Fe(SO ₄) ₂	HSF	Me ₃ NO		141
Fe ₂ O ₃	(NH ₄) ₂ Fe(SO ₄) ₂	RpfFer	air		144
γ-Fe ₂ O ₃	(NH ₄) ₂ Fe(SO ₄) ₂	RhsFer	H ₂ O ₂		144
Mn ₃ O ₄	MnCl ₂	RhsFer	H ₂ O ₂		144
salts	reactants	protein cage	particle-forming chemical		ref
CdPO ₄	CdCl ₂ /PBS Cd(NO ₃) ₂ /PBS U(OAc) ₂ /PBS	HSAF	diff./reassemble		135 136 149
UPO ₄		HSAF			

Table 2. continued

		incorporated		
ZnPO ₄	Zn(NO ₃) ₂ /PBS	HSAF	diff./reassembly	135
InPO ₄	In(SO ₄) ₃ /PBS	RLcHSAF		
PbPO ₄	Pb(NO ₃) ₃ /PBS	ApoHSF	diff./reassembly	135
	Pb(NO ₃) ₃ /PBS	ApoHSF		136
YPO ₄	Y-salt/PO ₄ -ions	HSAF		174
LuPO ₄	LuCl ₃ /PBS	HSAF		175
Fe ₃ (PO ₄) ₂	FeSO ₄ or FeCl ₂ /H ₃ PO ₄	HSAF	air	70
Fe ₃ (AsO ₄) ₂	FeSO ₄ or FeCl ₂ / H ₃ AsO ₄	HSAF	air	70
Fe ₃ (VO ₄) ₂	FeSO ₄ or FeCl ₂ /H ₃ VO ₄	HSAF	air	70
Fe(MoO ₂)	FeSO ₄ or FeCl ₂ /H ₂ MoO ₂	HSAF	air	70
BaCO ₃	BaCl ₂ /Na ₂ CO ₃	HSF	PMMA-mediated	176
SrCO ₃	SrCl ₂ /Na ₂ CO ₃	HSF	PMMA-mediated	176
CaCO ₃	Ca(HCO ₃) ₂	HSAF	37 °C	177
	CaCl ₂ /Na ₂ CO ₃	HSF	PMMA-mediated	176
semiconductors		reactants	protein cage	particle-forming chemical
CdS	Cd(OAc) ₂ /Na ₂ S	HSF		ref
	Cd(OAc) ₂ / thioacetic acid	HSAF		140
	Cd(OAc) ₂ /Thioacetic acid	LiDps		178
CdSe	Cd(OAc) ₂ /selenourea	LiDps		179
	CdCl ₂ /NaHSe	HSAF		180
ZnSe	Zn(Oac) ₂ /selenourea	HSAF		181
Au ₂ S	KAuCl ₄ /thiourea	HSAF		142
FeS	(NH ₄) ₂ Fe(SO ₄) ₂ /Na ₂ S	HSF		182
	(1) Fe(NO ₃) ₃ ; (2) H ₂ S	HSF	(1) air	145
CuS	Cu(OAc) ₂ /thioacetic acid	HSAF		146
PbS	Pb(AcO) ₂ ·3H ₂ O/Na ₂ S	HSF		183
				184

^aHSF, horse spleen ferritin (core removed chemically unless stated otherwise); HSAF, horse spleen apo ferritin; RLcHSAF, recombinant light-chain horse spleen apo ferritin; RHcHSAF, recombinant heavy-chain horse spleen apo ferritin; Hsp-Mj, heat shock protein from *Methanococcus jannaschii*; Fmfer, frog M ferritin; PfFer, ferritin protein cage, from the hyperthermophilic archaeon *Pyrococcus furiosus*; PfFt, ferritin from the hyperthermophilic bacterium *Pyrococcus furiosus*; LiDps, listeria innocua DNA-binding protein from starved cells; Hsp-Mj, heat shock protein cage from *Methanococcus jannaschii*; RpfFer, recombinant *Pyrococcus furiosus* ferritin; BacterA-PfFer, bacterioferritin ferritin A *Pyrococcus furiosus* ferritin; RhcHfer, recombinant heavy-chain human ferritin; flp-Li, ferritin-like protein from *Listeria innocua*; Mfer, mammalian ferritin; RHsFer, recombinant *H. sapiens* ferritin; addition of (m) noted that a genetic mutant was used of the respective protein cage structure.

The directed mineralization inside the intact capsid is a prerequisite for the controlled synthesis of nanoscale materials without nonspecific bulk precipitation. Simple electrostatic arguments have been put forward to explain the formation of inorganic mineral cores, the ions of which are not ferroxidase substrates; particularly, the ferroxidase center cannot be involved in the successful mineralization of recombinant ferritin particles, which are composed of only L-chain subunits and thus are lacking the enzymatic center. It was assumed that the complementary negative electrostatic potential inside the protein shell produced by acidic amino acid residues attracts the metal ions and induces nuclei formation. After a nucleus has formed, materials may grow autocatalytically in size. The size-dependent autocatalysis on the mineral surface leads to a growth of the large particles at the expense of the smaller ones for subsequent incremental additions of ions, eventually leading to particle sizes exceeding the cavity volume.^{140,141} This putative model was formed on an elucidative experimental basis by Meldrum et al. and Iwahori et al.¹⁴² They found that reconstitution with MnOOH resulted in an all-or-nothing behavior pointing to a prevailing autocatalytic mechanism. Among fully loaded apo ferritin, many empty protein cages were found. In the reconstitution of horse spleen apo ferritin with FeOOH cores, on the other hand, there is a slow and effective catalysis, which enabled almost all protein shells to grow cores of which the size was dependent on the available iron ions. Control experiments with genetically engineered ferritin cages

lacking the ferroxidase center confirmed the explanation model.¹⁴³ The electrostatic potential in the 3-fold channel and the protein cage interior have a pronounced effect, while the enzymatic center plays a minor role in the efficient core formation for nonferroxidase substrates. The low catalytic activity of the protein on non-native inorganic substrates also explains the less uniform inorganic cores. The complementary action of the two protein surfaces of the cage wall on ions, clusters, or nanoparticles has sometimes led to the notion of being a "Janus" architecture: While the outer surface of the protein inhibits inorganic particle formation, the inner cavity allows for precipitation and fosters uninhibited growth of inorganic matter. Another way to sequester material inside the cage is to change conditions that slowly induce precipitation of the infiltrated ions. The higher ion concentration inside the protein cage led to a preferred nuclei formation due to preferable electrostatic interaction, which increases the electrostatic gradient and promotes the further autocatalytic growth of the cores. On the other hand, hydrolytic nonredox mineralization leads to more pronounced mineralization around ferritin and bulk precipitation.¹¹⁹

The metal/protein ratio is often determining the nanoparticle size. However, similarly important as the size of the nanoparticle are their crystalline domain sizes, which have, for example, an influence on the magnetic response. Jolley et al. analyzed the total X-ray scattering by pair distribution function analysis to examine the size of the crystalline domains of

various nanoparticles formed inside ferritin.¹⁴⁴ They suggested using chimeric protein cages, assembled from subunits with a low number of crystal nucleation sites, or the use of more stable protein cages, for example, from *Pyrococcus furiosus*, which allow high temperature synthesis and the formation of larger crystalline domains.

3.2.1. Formation of Mineral Cores. The first non-native inorganic cores that were synthesized inside ferritin were iron sulfide, manganese oxide, and uranyl oxide after which many more non-native cores followed (Table 2).¹¹⁹ Iron sulfide was synthesized by chemical conversion of the native iron oxide with H₂S or Na₂S. The final cores had a slightly smaller average size as the starting ferritin cores and were amorphous. EDX analysis gave a Fe/S ratio close to one for the reaction with H₂S, pointing to nearly stoichiometric conversion of the ferrihydrite core to FeS. The reaction with Na₂S proceeded much slower and did not lead to full conversion.

The iron sulfide that precipitated in alkaline solution when native ferritin was bubbled with H₂S was investigated in more detail by ⁵⁷Fe Mössbauer spectroscopy.^{119,145} Only partial transformation of the ferrihydrite core was observed, and it was assumed that only the outermost iron atoms reacted, forming a ferrihydrite core–iron sulfide shell structure. Thus, the iron sulfide was amorphous but could be related to mixed-valence ferrimagnetic sulfides in terms of its magnetic structure. On the other hand, complete transformation of native ferrihydrite to iron sulfide cores was observed under slightly acidic conditions.¹⁴⁶ A detailed analysis of the predominantly amorphous iron sulfide cores with extended X-ray absorption fine structure (EXAFS) analysis, X-ray absorption near-edge structure (XANES) analysis, and ⁵⁷Fe Mössbauer spectroscopy revealed that an unusual Fe(III)–sulfide was formed in which high-spin Fe(III) is present in a tetrahedral environment.

Manganese oxide cores were formed by reconstitution of the mineral core inside demineralized ferritin in MnCl₂ solutions at pH 8.0–9.2. Here, some nonspecific precipitation was observed that consisted of a mixture of crystalline α -MnOOH and Mn₃O₄.¹¹⁹ In contrast, electron diffraction of reconstituted ferritin gave no diffraction pattern, indicating that the protein-coated cores were amorphous.¹⁴³ In a following detailed X-ray absorption spectroscopy (XAS) study, the core structure of manganese oxide reconstituted ferritin was related to that of γ -MnOOH.¹⁴⁷ The oxidation state of Mn was found to be (III). Reconstitution of manganese oxide cores in horse spleen and several recombinant ferritins was used to elucidate the mechanism of mineral formation.¹⁴³ TEM revealed the formation of defined cores with regular spherical morphology and only minor nonspecific oxide formation in solution. MnOOH-reconstituted apoferritin can be reduced to render biocompatible magnetic resonance imaging agents (see below).¹⁴⁸ Uranyl acetate, which is commonly used for staining protein assemblies and virus particles, was found to be able to penetrate the protein shell as well. A yellow gel was forming at alkaline pH in solution by the hydrolytic polymerization of uranyl acetate (UO₂(O₂CCH₃)₂), but TEM analysis revealed also a preferential precipitation of electron dense cores inside the protein cages.¹¹⁹ Hainfeld infiltrated apoferritin with uranyl ions through incubation at pH 4 where uranyl ions were stable in solution; after increasing the pH, the uranium precipitated inside the cavity, and crystallization was further enhanced by adding phosphate buffer.¹⁴⁹ With a large excess of uranium, the mineral could grow strongly and break the protein shell. However, with optimized conditions, a loading of around 800

atoms per apoferritin could be achieved with only limited solution precipitation. The uranium loaded ferritin particles are supposed to be a superior novel system for neutron capture therapy.

Of special interest are the synthesis of nanoparticles with useful properties, such as magnetic or luminescence. Magnetic iron oxide cores were synthesized in the protein cavity (magneto-ferritin) if the reconstitution experiments were done under conditions favorable for the formation of Fe₃O₄.^{150,151} Electron diffraction could not unambiguously clarify whether magnetite (Fe₃O₄) or maghemite (γ -Fe₂O₃) was formed in the protein cavity. Although the protein free control experiment clearly produced magnetite crystals under the given conditions, the catalytic ferroxidase activity may also induce the formation of a different crystal structure. The magneto-ferritin particles did not react to a bar magnet because the encapsulated crystals were within the superparamagnetic size range for magnetite. The synthesis was later changed using stoichiometric trimethyl-N-oxide as oxidant under anaerobic conditions.¹⁴¹ Higher loadings were achieved by using incremental additions of Fe(II) at concentrations that did not exceed the solubility of Fe(OH)₂. An increasing number of particles with dimensions greater than the protein cavity were observed. The size-dependent autocatalytic growth resulted in a number of empty particles and an increasing number of particles with larger cores, which grew at the expense of smaller ones, eventually exceeding the size of the ferritin cavity. Aggregated but not intergrown bioinorganic particles were observed. Many individual iron cores were single domain crystals, but the weak superlattice reflections to distinguish maghemite from magnetite were not observed. A detailed investigation of the magnetic properties hinted that the cores must be predominantly maghemite. All samples were superparamagnetic below 100 K, and the respective blocking temperature increased from 10 to 100 K for increased iron loadings as for natural ferritin. The magnetic stability of the cores was very sensitive with respect to its size in such a way that the remanences changed by three orders of magnitude while the core volume changed by only one order of magnitude. To change the magnetic properties without changing the particle size as this is given through the protein template, doping with other magnetic transition metals, for example, manganese, can be done. To this end, co-oxidation of iron and manganese works well, and iron oxide particles with manganese contents between 6.1% and 33% have been synthesized and structurally characterized.¹⁵² Recently, a revised synthesis protocol was given by Douglas and co-workers for the preparation of ferritin iron oxide magnetic resonance contrast agents.¹⁵³ (NH₄)₂FeSO₄·6H₂O and H₂O₂ were slowly and continuously added to the recombinant human H chain ferritin solution at pH 8.5 and 65 °C under inert atmosphere. Ferritin was reconstituted with 1000, 3000, or 5000 Fe atoms per cage, corresponding to particle sizes from 3.6 ± 0.7 to 5.9 ± 0.9 nm. As mentioned above, also these particles could not be unambiguously identified as either maghemite or magnetite. Another study has to be mentioned at this point, which aimed at elucidating the conditions of the biological formation of magnetite nanocrystals. Prozorov et al. precipitated iron oxide in an aqueous viscous Pluronic solution of Fe(II) and Fe(III) by increasing the pH in the presence of various proteins.¹⁵⁴ A protein isolated from magnetosome membranes directed the formation of 30 nm large magnetite crystals with good crystallinity, while under the same conditions much smaller nanoparticles formed inside ferritin, which were

largely amorphous. The controlled synthesis of highly stable protein coated magnetic minerals is considered as promisingly useful in a variety of applications, for example, magnetic labeling and imaging or separation.¹⁵³

While a considerable amount of phosphate anions is bound in natural ferritin, only minor attention has been paid to other anions. Oxyanions are, however, of particular interest. Polanams et al. investigated the kinetics of iron oxide core formation in the presence of phosphate and various other oxyanions, particularly, arsenate, molybdate, and vanadate.⁷⁰ The mechanisms of the entry of the negatively charged species are hard to explain and still largely unknown. Although there is a considerably large negative potential at the 3- and 4-fold channels, oxyanions could enter the cavity without capsid disassembly. Further, the radii of the fully deprotonated PO_4^{3-} , AsO_4^{3-} , VO_4^{3-} , and MoO_4^{2-} anions (i.e., in the state with smallest radius) exceed the channel size as determined from X-ray crystallography of ferritin. The large oxyanions were incorporated in even higher ratios than was phosphate. The overall iron-loading reached 71–92% of the iron-only control sample, and amorphous, but stable and nonleaching mineral cores were formed. The presence of oxyanions increased the initial rate of core formation as compared to control reconstitution experiments and changed the kinetic curve from sigmoid to hyperbolic.⁷⁰ The obviously different mechanism was attributed to less involvement of the catalytic ferroxidase center. Rather, the catalytic surface of the formed nuclei was determining the rate of mineral core formation.

It has always been a trial-and-error procedure to find the optimal reaction conditions for the synthesis of non-native inorganic nanoparticles inside the apoferritin cavity. Several strategies were used to prevent unspecific precipitation in the bulk solution, which is the most often encountered difficulty. The precipitation of protein during the synthesis is another often occurring side reaction. Tsukamoto reported on their systematic assessment of optimal conditions for the preparation of cobalt oxide nanoparticles. The buffer medium and pH, reagent concentrations, and reaction temperature were critical parameters to avoid bulk precipitation and to obtain Co_3O_4 nanoparticles inside ferritin in a one-pot reaction.¹⁹¹ Finally, they succeeded in producing narrowly dispersed, near-monocrystalline Co_3O_4 nanoparticles within the ferritin cavity with a corresponding average diameter of 6 nm and high yields of core formation. The previously, by Douglas and Stark, reported oxidative precipitation of cobalt oxide nanoparticles proceeded also specifically inside the protein cage, but a stepwise procedure with slow incremental additions of Co(II) ions and H_2O_2 -solutions and dynamic titration with NaOH to maintain the pH at 8.5 was necessary.¹⁶⁷ The method of slow addition was adapted by Kim et al. to control the growth of the nanoparticles at the interior wall of ferritin.¹⁹² By doing so, the initially formed small nanoparticles will merge while growing and at a certain point form hollow cobalt oxide nano shells as shown by scanning TEM. The recipe was used with minor modification by Zhang et al. for the synthesis of Co(III)- and Mn(III)-cores with 800–1200 atoms/core.¹⁶⁶ They were interested in the electrochemical properties of the cores, and thus first determined the redox potential of Co(III)-HSF, which was found to be close to 0 mV. It was possible to evaluate a second-order reaction rate constant of $0.53 \pm 0.03 \text{ M}^{-1} \text{ min}^{-1}$ for the reduction with ascorbic acid (+47 mV vs ascorbic acid) by following the change of the typical absorption of cobalt

oxide-filled apoferritin at 350 nm over time with UV-vis spectroscopy.

Okuda reported the fabrication of nickel hydroxide and chromium hydroxide nanoparticles.¹⁶⁸ A screening of the synthesis conditions and concentrations provided an optimal recipe. The optimized synthesis conditions gave 80–100% yield of core formation (YCF = number of mineralized apoferritin over total number of protein cages) and 100% efficiency of core formation (ECF = YCF multiplied by supernatant protein concentration, divided by the initial apoferritin concentration). YCF gives a measure of how homogeneous the mineralization occurred, while ECF accounts for precipitated protein. Addition of ammonia, which complexes the metal ions, greatly increased the ECF, that is, prevented excessive bulk precipitation. Interestingly, the formation of nickel cores required indispensably the introduction of carbonate by bubbling the solutions with CO_2 . Excessive protein precipitation was observed, if carbonate ions were employed as a salt. The role of carbonate ions is not clear yet, but they may stabilize the metal ions in solution by coordination and/or aid hydroxylation in the apoferritin as compared to the outside bulk solution. Copper oxide particles were formed during aerial oxidation of ferritin containing Cu metal particles, which were prepared by incubation of apoferritin with CuSO_4 at pH 8.0 and reduction with NaBH_4 .¹²⁴

The earth alkali ions calcium, strontium, and barium have low binding affinities to apoferritin.⁶⁹ Thus, while there is no active mechanism of particle formation inside the cavity, the successful mineralization can be achieved by actively inhibiting the precipitation in bulk solution. Mann and co-workers added water-soluble polyelectrolytes to the mineralization solution.¹⁷⁶ Such polymers act as potent inhibitors; however, because they cannot enter the apoferritin cavity because of their large size, their action is restricted to the bulk solution, and mineral precipitation can occur only within the protein shell. The authors provided a full characterization of encapsulated CaCO_3 (aragonite polymorph, mean particle diameter 5.4 nm). BaCO_3 , SrCO_3 , and hydroxyapatite cores could be synthesized by the same approach, yielding particles with an average size of 5.1–5.3 nm. While the carbonates were crystalline, the hydroxyapatite particles were only poorly crystalline. The proposed approach illustrates a general promising principle. Native ferrihydrite cores are formed by an active mineralization inside the cavity. Other transition metal minerals can be precipitated spatially selective inside the protein shell by active or passive mechanisms. Fukano et al. used a saturated $\text{Ca}(\text{HCO}_3)_2$ solution and a temperature increase to precipitate CaCO_3 .¹⁷⁷ Repetition with removal of the bulk precipitate yielded Ca-containing cores with 6 nm in diameter, which were quite sensitive for dissolution with respect to solution conditions.

Ferritin typically oxidizes metal ions to high oxidation states, which are then forming insoluble metal oxyhydroxy materials. Thus, starting with high oxidation metals does not lead to specific precipitations inside ferritin, and starting with low-oxidation state ions requires anaerobic conditions. Klem et al. avoided the competing bulk precipitation of oxidized metal ions by capping them with citrate.¹⁶⁹ Upon illumination with UV-light, transient low-oxidation state metal ions were formed, which precipitated upon reoxidation with aerial oxygen spatially selective inside the cavity as Fe(O)OH , Eu(O)OH , or titanium(IV) oxyhydroxide. Control experiments verified the crucial presence of ferritin to avoid bulk precipitation. The characteristic color of $\text{Fe}(\text{phen})_3^{2+}$ or of the charge transfer

bands of the Ti(III)-ion could be observed when the reaction was done under anaerobic conditions, clearly proofing the proposed photolytic reduction mechanism. The work will likely extend the variety of attainable core nanomaterials.

For special biomedical, analytical, or nanotechnology applications, even more special systems have been synthesized, for example, lutetium or yttrium phosphate particles inside biotin-modified ferritin for radioimmuno-imaging and -therapy (see below).^{175,193} Core formation in recombinant horse liver L-chain apoferitin proceeded upon incubation at room temperature with indium sulfate under highly acidic conditions in almost 100% of the ferritin particles and yielded nicely round shaped cores with a diameter of 6.6 ± 0.5 nm.¹⁷⁴ The use of highly uniform recombinant apoferitin particles and controlled mineral deposition conditions was the requirement for the formation of excellent ordered and nearly defect-free hexagonal arrays of indium nanoparticles on solid surfaces. Cadmium and lead phosphate cores were prepared for electrochemical assays, but preparation of encoded particle (i.e., with a predetermined ratio of different metal ions in the core) was not successful except for the disassembly reassembly route (see above).^{135,136} Gadolinium(III) oxide hydroxide was sequestered by incubation of apoferitin solution with gadolinium nitrate solution.¹⁷⁰ Only negligible amounts of Gd(III) were released from the purified particles, a prerequisite to minimize toxicity of the metal-ions in biomedical applications. The particles were amorphous, and a crystalline phase corresponding to Gd_2O_3 developed upon calcinations above 400 °C. The magnetic characterization is described in more detail below. Cerium oxide nanoparticles were synthesized inside ferritin, and two-dimensional arrays and three-dimensional crystals were formed by salt bridge formation.¹⁷¹ The overall core formation ratio was low with only 7%. Particles with an average particle size of 5.0 ± 0.7 nm were formed. HR-TEM showed that the majority of the particles were CeO_2 consistent with the XRD pattern, but some minor amount of particles was also of Ce_2O_3 . Excess free cerium ions in the solution of ceriumoxide-ferritin particles led to the development of well-ordered, two-dimensional as well as three-dimensional crystals with octahedral or prismatic morphology.

3.2.2. Formation of Semiconductor Core Particles. In addition to metallic nanoparticles, semiconductor materials can also be incorporated into the ferritin biotemplate, which expands the scope of ferritin use for controlled biohybridization and templated synthesis containers. Yamashita et al. used a slow reaction system for the synthesis of CdSe nanoparticles.¹⁹⁴ They stabilized the cadmium(II)-ions through complexation with ammonia as $(\text{Cd}(\text{NH}_3)_4)^{2+}$. Further, they used seleno-urea, which slowly degrades in aqueous solution and provides a continuous source of small amounts of selenium ions. At pH 9.5, 5 mM ammonia–water, and deoxygenation by N_2 -bubbling, the core formation ratio was highest and CdSe bulk precipitation outside apoferitin lowest.¹⁹⁵ XPS confirmed that the formed cores consisted of cadmium and selenide. Cadmium ions were concentrated by the electrostatic gradient inside the cavity and led to a predominant nanoparticle formation inside the cavity, which acted during the further course of the reaction as self-catalytic centers. The formation of multicrystalline CdSecores inside apoferitin was accompanied by only little solution precipitation. XRD on heat-annealed (500 °C) samples showed that the core structure was predominantly the cubic zinc blend and only little hexagonal wurtzite structure. Very similar in the approach was the synthesis of Xing et al., who used

ethylenediaminetetraacetic acid (EDTA) as Cd(II) complexing ligand and NaHS_e as selenium supply.¹⁸¹ The obtained quantum dots with cubic zinc blende structure showed no cytotoxicity in a simple test with Hela and HepG2-cells. Wong and Mann avoided unspecific bulk precipitation by a preincubation of ferritin with a stoichiometric amount of 55 cadmium(II) ions per cage and reaction with excess sulfide after 1 h, that is, a two-step synthesis protocol.¹⁴⁰ Cadmium(II) had the highest binding to ferritin with an approximately equal number of binding sites to the exterior and interior protein shell of 28 and 26, respectively. The samples were dialyzed before new incubation. Few cycles of incremental incubations with cadmium(II) and sulfide yielded CdS nanoparticles inside the ferritin. The CdS cores were of irregular shape and showed a broad size distribution from 1.5 to 7.2 nm. Thus, the nanoparticles were lacking a distinct exciton peak and absorption edge in their electronic spectra. The larger particles had the zinc blende structure, and few particles were single crystals. However, applying the slow chemical reaction system to the formation of CdS-cores enabled the synthesis of cores with improved photoluminescence. Incubation of ferritin in a weakly acidic solution containing cadmium acetate, ammonium acetate, and thioacetic acid yielded slowly and over all ferritin cavities evenly growing nanoparticles.¹⁹⁶ This is in contrast to the all-or-nothing behavior in the synthesis of CdSe, ZnSe, or CuS and indicates a weak autocatalytic activity of the CdS-nanoparticle surface. Increasing the ammonia concentration from 7.5 to 75 mM leads to a longer Cd-ion supply period accompanied by an increased core size from 4.7 to 7.1 nm. In the same direction, the photoluminescence intensity of the ferritin protein shell at 430 nm decreased and that of the CdS core at 500–700 nm increased with a red-shift. This indicates an excitation of the cores by the photoluminescence of the protein shell.

Further, the use of genetically engineered apoferitin with a more positive zeta potential, that is, surface charge, resulted in a much lower core formation ratio (ferritin particles with reconstituted cores over employed apoferitin particles), indicating the importance of the surface charge for attraction and incorporation of metal ions. Recently, CdS quantum dots prepared by the slow chemical reaction protocol were shown to exhibit circularly polarized luminescence.¹⁷⁸ The chiral protein template can induce a chiral crystal structure, not in the expected hexagonal phase but in cubic phase crystals. Signals from both the direct transition band as well as from the surface-trapping sites were detected, and the circular polarized luminescence was explained by single crystal cores, which are present up to 7% in the overall composition and the rest of the double, triple, or polycrystals. HR-TEM was used to prove and quantify the distribution of the polycrystal cores.

The successful approach of the slow chemical reaction system was consequently extended to the formation of ZnSe nanoparticles, which would give otherwise excessive bulk precipitation from the intense reaction between zinc and selenium ion.¹⁴² The systematic approach was also successfully applied to the formation of CuS nanoparticles inside apoferitin.¹⁸³ CuS cores had a high catalytic surface reactivity, and core formation proceeded according to an all-or-nothing behavior. Sintering above 500 °C converted the particles to Cu₂S single crystals. ZnSe, CdSe, CdS, CuS, etc. are interesting n-type semiconductor materials with fluorescent properties rendering them as useful quantum labels, which do not easily quench.

A careful investigation of optimal conditions was performed and resulted in the successful production of monodisperse ZnSe particles with a cubic crystal structure. Because the cores were usually polycrystalline, one can assume multiple nucleation sites in the cavity from which crystal growth started. Correspondingly, the large number of defects quenched the photoluminescence of the biotemplated quantum dots. Annealing gave well-separated, single crystalline ZnSe nanocrystals. The sequence of addition of zinc and selenide proved important in the synthesis of these nanocrystals. The addition of selenide after incubation with zinc ions produced ZnSe cores but not the reverse order, pointing out the importance of accumulation of metal ions inside the cage before precipitation. A similar synthetic approach was also employed for the synthesis of gold sulfide nanoparticles.¹⁸² PbS quantum dots, however, were formed inside the apoferritin cage by simple incubation with Pb(OAc)₂ and Na₂S at pH 5.5.¹⁸⁴

3.2.3. Formation of Metal and Metal Alloy Cores. A current topic in catalysis is suspended metal nanoparticles, which have been immobilized on some submicrometer scaffolds. Pd(0)-nanoclusters inside the ferritin capsid were used by Ueno et al. for the catalytic hydrogenation of olefins in aqueous medium.⁶¹ The synthesis was carried out by first incubation of the apoferritin with palladium(II)-salt under slightly alkaline conditions and then reduction to Pd(0)-clusters by NaBH₄. While no black precipitates were formed as in protein-free control experiments, it was shown by UV-vis, FPLC, and native PAGE that small Pd-clusters were present inside the ferritin cavity. Particularly, analysis with TEM revealed that round-shaped clusters of 2.0 ± 0.3 nm were formed specifically inside the protein cage. The investigation of the catalytic properties with substrates of different steric demand suggested that the anionic 3-fold hydrophilic channel in the protein cage is the pathway for substrates as the turnover frequencies correlate with the substrate size rather than with the substrate reactivity. No enantioselectivity in the products was observed. Similarly, Pd/Au alloy nanoparticles and bimetallic Pd@Au or Au@Pd core–shell particles were prepared by a coreduction or sequential reduction.¹⁶² The different catalytic behavior of these particles in hydrogenation of acrylamide discriminated the different nanoparticle morphologies. Watanabe and co-workers investigated the coordination structure of palladium ions and organometallic palladium complexes in apoferritin. Upon incubation with [Pd(II)(allyl)Cl]₂, 96 palladium complexes were bound. The anomalous different Fourier maps of crystallized ferritin displayed the presence of two binding areas, one located at the 3-fold axis of the channel and one area that is called the accumulation center.¹⁹⁰ In the first location, three times two palladium ions form a dinuclear thiol bridged structure with Cys126 and are stabilized by the N^e of His114 and a water molecule. At the accumulation center, two palladium ions are bridged by the thiol-group of Cys48. They are additionally coordinated by the O^e of Glu45 and N^d of His49. If the His114 or His49 are exchanged by a non-coordinating Ala, only trinuclear Pd-complexes with a square-planar structure were formed at the 3-fold channels. Here, Cys126 is used to build a six-membered ring structure, while at the accumulation center the coordination of the two palladium ions was solely taken over by the carboxylate moiety of Glu45.¹⁹⁰ While the replacement of His114 or His49 changed the coordinating sphere, the deletion of cysteine Cys126 and Cys48, which are located at the 3-fold axis and the accumulation center, respectively, led to a loss of the Pd-

binding ability in these areas.¹⁸⁹ The essential role of Cys residues in forming the bridged dinuclear Pd-structures with assisting His residues nearby, which control the orientation of the palladium complex through interactions via the nitrogen, was confirmed with further mutants.¹⁹⁷ In another investigation, the quantity and location of palladium ions were determined for recombinant L-chain apoferitin from horse liver after incubation with different concentrations of K₂PdCl₄.¹⁹⁸ First, the three coordination sites at the 3-fold channel and three sites at the accumulation site are occupied, followed by two more palladium ions at the accumulation center and up to three palladium ions at so-called third sites. No palladium ion was found at the ferrihydrite nucleation site, which can be due to the square-planar coordination sphere of palladium versus the octahedral coordination structure of Fe(II), Cd(II), Zn(II), or Mn(II). The binding of Au was also different: only two gold(III) ions were bound at the 3-fold channel and three at the accumulation center because of the different affinities of the metal ions toward the different amino acids.¹⁶² In an extension of their work, also ruthenium, another versatile catalytic active transition metal, was incorporated as a Ru (*p*-cumene) half-sandwich complex.¹⁸⁷ However, only one Ru at the accumulation center kept its *p*-cumene ligand; both others lost it at their coordination positions. An in-depth investigation of the magnetic properties of the (fcc) Pd-nanoparticles was pursued by Clemente-Léon et al. and is discussed below.¹⁵⁵

For creating metallic platinum particles inside the ferritin template, Deng et al. incubated apoferritin with K₂PtCl₆ and obtained Pt-ferritin hybrid particles after reduction with NaBH₄.⁶⁰ The maximum uptake of Pt ions was 12.7 mmol/lh per mM apoferritin. The size distribution of the obtained nanoparticles was quite broad with an average size of 4.7 ± 0.9 nm. The effect of Pt-loaded ferritin on reduction of oxidative stress and cytotoxicity on cells was explored by Knez and co-workers.¹⁶⁵ They give also more details on the XPS spectra of their 2 nm-sized platinum nanoparticles.

Also, Galvez et al. used this approach and reduced apoferritin solutions with NaBH₄, which have been previously incubated with Co(II)- or Ni(II)-salts.¹⁵⁷ Upon addition of the reducing agent, the initially colored solutions turned blackish, but no precipitation was observed. TEM with negative staining revealed the formation of small nanoparticles of 3.5 ± 0.5 and 3.0 ± 0.5 nm for the nickel and cobalt hybrids, respectively, inside the apoferritin cavity. According to XRD, the nanoparticles were almost amorphous, but annealing produced the respective fcc-crystalline metal nanoparticles. Both kinds of nanoparticles were superparamagnetic. Encapsulated Cu(II)-ions could also be reduced by NaBH₄ to form metallic Cu nanoparticles.¹²⁴ After incubation with CuSO₄ and dialysis, approximately 225 Cu(II)-ions were bound to the interior of apoferritin, which led to particles with a monodisperse size distribution of around 3.5 nm in diameter. The metallic particles were only stable under inert conditions; upon exposure to air, a significant decrease in intensity of the surface plasmon absorption band at 570 nm was observed, indicating the oxidation of the Cu to Cu₂O particles. The uptake of copper ions inside apoferritin at alkaline pH was explained by the precipitation of Cu-oxide/hydroxide species, as also was shown by X-ray near edge structure (XANES) spectroscopy.^{156,199} While the Cu-nanoparticles are crystalline (fcc) at low temperature, the increase of the Debye–Waller factor of the second and third coordination shells points to a phase

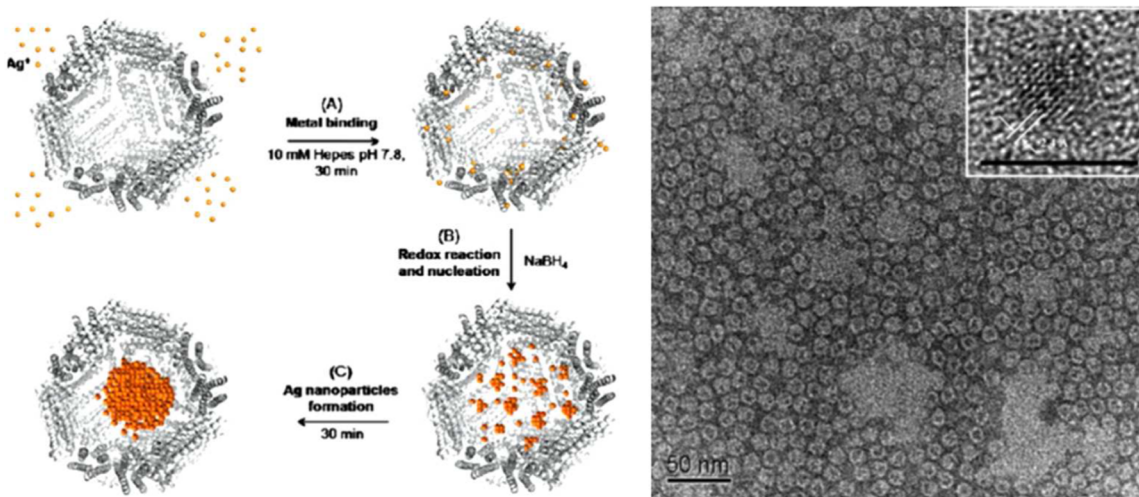


Figure 13. Inclusion of Ag ions in the ferritin cage followed by reduction and further growth of the Ag-nanoparticle. Left: A schematic reaction scheme. Right: TEM analysis of the ferritin–Ag composite particle. Reprinted with permission from ref 87. Copyright 2010 American Chemical Society.

transition via an amorphous phase. Above 260 K, the nanoparticles' structure seems to be best described by a relaxed surface structure with slightly larger Cu–Cu-distances than in the FCC structure, while the first-order distance of most copper atoms corresponds more to the less stable BCC phase.^{156,199} Ensign et al. produced copper metal nanoparticles through photocatalytic reduction of Cu(II) with citrate or tartrate.¹⁷² The nanoparticle formation depended on the presence of the ferrihydrite core and the iron loading, that is, the Cu(II)/ferritin ratio. Increasing Cu(II)/ferritin ratios led to larger particles, which tended to strongly exceed the size of the ferritin cage of 12 nm. Thus, it was proposed that either the protein cage is disrupted by the growing metal nanoparticle or they are grown on the outside of the ferritin cage. TEM images of the reaction product could not exclude one of the two cases. Nevertheless, the broadly disperse particles remained well-stabilized in solution and were shown to be purely fcc Cu(0) by EELS. The “core”-formation ratio was not very high. The solution could be reoxidized and reductively rephotolyzed in several repeated cycles; only minor amounts of protein shell subunits from disassembled ferritin cages could be detected.

Gold nanoparticles represented some challenge as there is a poor natural preference for the ferritin interior over the exterior to bind gold ions. The reduction of gold(III) compounds in the presence of apoferritin in solution with NaBH₄ or MOPS yielded broad polydisperse gold nanoparticles, which were not contained within the apoferritin cage but rather attached to the outside as was seen by TEM.¹⁵⁸ Fan et al. used a two-step reduction procedure to grow gold particles on seeded gold–ferritin clusters inside the cavity.¹⁶⁰ Unmodified native horse spleen apoferritin was incubated with AuCl₄⁻ complex ions, desalting, and reduced with NaBH₄. The low abundance of gold atoms was sufficient to form small clusters, which, although characterization with UV-vis and HR-TEM failed due to their small size, worked as highly efficient seeds for a second mild reduction of AuCl₄⁻ with ascorbic acid. The homogeneous particles that fully filled the apoferritin cavity were identified as gold face-centered cubic, mostly single crystals with a plasmon band at 519 nm. Gold–silver alloy nanoparticles were produced by simple incubation of HSAsF with AgNO₃ and HAuCl₄ in an ammonium alkaline solution at pH 8.3.¹⁶³ Core formation

ratios over 80% were achieved, and the protein coated nanoparticles showed good catalytic activities in the reduction of nitrophenol with sodium borohydride. The pseudo-first-order kinetic constant increased exponentially with the Au-content in the alloy particles.

Silver metal nanoparticles were prepared after incubation with AgNO₃ by reduction with NaBH₄.¹⁶¹ The excess silver in the solution was removed before adding the reduction agent. The initial silver to apoferritin ratio determined the final size of the nanoparticles: for example, a ratio of 5000/1 and 500/1 (Ag/ferritin) yielded nanoparticles of 4 ± 0.5 and 1 ± 0.1 nm in diameter, respectively (Figure 13). The surface plasmon resonance frequency of the larger nanoparticles was influenced by the surrounding apoferritin protein shell because the electronic properties are highly sensitive to the dielectric properties of the surrounding medium. On the other hand, the smaller ones were less influenced, and the electronic spectra resembled more those of free Ag nanoparticles. High-resolution electron microscopy showed that some of the formed nanoparticles were single domain fcc crystals; most of them, however, consisted of single or multiple twinned domains. The surrounding protein shell was imparting increased stability also to very small silver particles.

Recently, proteins with specific binding properties have been identified by surface display technologies. Particularly, the identification of metal-binding protein sequences enabled the construction of nanoparticle–protein composites by directed interactions. Thus, a higher material specificity inside the cavity can be achieved if metal-binding peptides are displayed on the inner cavity wall. For this, Kramer et al. fused the silver binding AG4 peptide to the C-terminus of the L-chain of human ferritin and expressed the protein in *E. coli*.¹⁵ The additional oligopeptide did not prevent the proteins from self-assembling to the prototypical ferritin cage after purification. Incubation of the modified apoferritin cage in silver nitrate solution resulted in the formation of monocrystalline pure silver particles with an average diameter of 5 nm within the protein shell. No surface plasmon resonance peak indicative for Ag-nanoparticle formation was observed for the control native apoferritin. An in vivo strategy was followed as well. For this, silver nitrate was added to the growing bacterial culture, and silver nanoparticles

were *in vivo* grown in the expressed ferritin particles. The mean size distribution was 7 ± 1 nm, and empty or partially filled cages were observed as well. Less reduction of cell viability for cells expressing the silver binding peptide was observed as compared to a reference cell culture.¹⁵ The presented strategy is quite general. Recent progress in biomaterials chemistry identified many peptide sequences, which induce nucleation and support growth of nanometer sized particles of CdS, ZnS, SiO₂, CoPt, etc.¹⁰ Introducing such sequences allows for a more controlled synthesis of ferritin composite materials or binding them to specific surfaces.

Many types of nanoparticles with interesting properties are still difficult to synthesize under mild conditions; for example, high temperature annealing can be necessary to obtain monocrystalline particles. Recently, Thomas and co-workers showed that the ferritin subunits can readily be self-assembled around preformed cores, thus extending the range to nanoparticles that have to be synthesized under nonbiological conditions.¹⁸⁴ They used two different routes to prepare ferritin containing PbS nanoparticles: either by the “nanoreactor route”, that is, incubation of empty intact apoferritin cages with lead acetate and sodium sulfide at pH 5.5 with concomitant formation of quantum dots inside the protein shell, or by the “assembly route”, that is, the encapsulation of thioglycerol capped preformed PbS-nanoparticles by slow readjustment of the solution pH from 2 to 9 and reassembly of the dissolved ferritin subunits to intact cages. The successful and precise encapsulation was shown with electron microscopy techniques in both cases. The photoluminescence properties of both composite particles were also very similar, but a small shift of the photoluminescence energy to higher values as compared to the non-encapsulated quantum dots was observed. This was explained with a possibly different size distribution. The protein shell may either restrict the formation of larger nanoparticles or stabilize smaller ones better. In this particular example, both routes gave very similar structures.^{184,200} To guide the encapsulation of nanoparticles inside the protein shell, affinity labels were introduced at the C-terminus of the protein subunit, which is directed to the interior. In this way, gold nanoparticles were entrapped. The fuzzy protein shell visible in TEM and the analysis of the protein/gold nanoparticles ratio revealed that probably no well-ordered shell is formed but approximately 32 subunits wrap the gold nanoparticles in a disordered manner.¹⁵⁹ However, one can easily imagine that encapsulation of nanoparticles via the reassembly route opens the possibility to prepare novel biocoated nanoparticles, which were previously inaccessible via the nanoreactor route, and to render them water-soluble and biocompatible.

3.3. Synthesis of Inorganic Cores in Ferritin-Like Cages

The cage of Dps is, like ferritin from *Listeria innocua*, a dodecameric protein cage with an outer diameter of 9 nm and a correspondingly smaller cavity of 4.5 nm. Thus, by analogous reactions, *Listeria* ferritin can be used for size-constrained synthesis of smaller inorganic nanoparticles with different electronic and optical properties. Although the Dps-like protein assembly does not contain inorganic cores in native states, iron oxide core formation was studied and mechanistic details were clarified, which puts the Dps-like cage into a new category of ferritin-like particles (FLP). Since then, few different inorganic cores were synthesized. The mineralization procedures were readily adapted from ferritin. In the research groups of Young and Douglas, various inorganic cores have been synthesized.

First, synthesis of iron oxide cores was done at 65 °C at which the FLP was still stable at pH 8.5 in the presence of H₂O₂.⁹⁵ Powder diffraction pattern suggested that the particles were cubic phase γ-Fe₂O₃. Further, Allen et al. synthesized two cobalt oxide minerals, Co₃O₄ and Co(O)OH, inside the cavity.⁹⁶ The first product was produced at 65 °C, while the latter formed at room temperature. In both cases, TEM shows the formation of electron dense particles in the FLP interior, but only the high temperature product showed diffraction patterns, indicating that the spinel phase of cobalt oxide Co₃O₄ was formed. The bulk precipitate of the protein-free room temperature synthesis was identified as low crystalline Co(O)-OH; most likely, this was also the poorly defined cores in the low temperature synthesis in the presence of the protein cage. The particles had an average diameter of 4.34 ± 0.55 nm.^{95,96} The magnetism of the antiferromagnetic Co₃O₄ particles was investigated, and surface or finite-size effects may play a major role in the magnetic behavior, which was characterized by a low Néel temperature of 15 ± 2 K.²⁰¹ The magnetic properties of the maghemite (γ-Fe₂O₃) formed in *Listeria innocua* Dps were also magnetically characterized.²⁰² The slow chemical reaction synthesis was applied for the synthesis of CdS-nanoparticles. The reaction conditions had to be optimized, and the final reaction solutions were compared to the optimum conditions in horse spleen apoferritin. Particularly, the amount of ammonia–water and the added thioacetic acid were adjusted, and core formation ratios of up to 53% were achieved.¹⁷⁹ The pH of the solution specifically influences the dissociation equilibrium of the released H₂S, and only at pH 8.5 was stoichiometric CdS with a multicrystalline cubic phase obtained. For the preparation of CdSe nanoparticles, repetitive additions of a small amount of selenourea were applied to the *Listeria*–Dps solution, which was incubated with cadmium acetate, ammonium, and ammonium acetate.¹⁸⁰

For defined binding of platinum, the interior of the protein cage was genetically engineered to contain a cysteine in the middle of helix E. The sulphydryl group was chemically modified, to promote Pt²⁺ binding and probably facilitate nucleation of metal clusters upon photoreduction. The modification was verified with mass spectrometry to reach 85%, that is, 10.1 of binding motifs per dodecameric cage.¹⁶⁴ The process of metal binding was monitored with mass spectrometry; a loading with 43.5 Pt²⁺ ions was determined, while after photoreduction, a loading with 75 Pt(0) atoms was obtained. The catalytic properties of the Pt-clusters were tested through the production of hydrogen, and only the largest Pt(0) cluster was produced at significant higher level hydrogen. This work paves the way to a rational design of binding sites and thus the formation of non-native cores. The mass spectrometric analysis of *Listeria* Dps incubated with various amounts of Fe(II) and a half equivalent of H₂O₂ revealed that the first 12 Fe ions accumulate evenly into the protein cages.¹⁷³ In the following steps, small iron oxide cores form at higher loadings, while autocatalytic growth on the formed particle surfaces will be the prevailing growth mechanism.

4. FABRICATION OF TWO-DIMENSIONAL ARRAYS OF FERRITIN

When bionanoparticles are arranged as a two-dimensional array, interesting applications can be targeted. Also, ferritin is a much investigated protein at interfaces especially due to the possibility of incorporating different chemistries for adhesion control and the incorporation of inorganic cores, which can be

fluorescent, conductive, magnetically susceptible, or reactive. The two-dimensional arrays are not confined to solid surfaces; most interfaces can be used such as water–air, water–oil, water–cell, or water–solid interfaces. By using interface directed assembly, foams for food and drug formulations, capsules for delivery and emulsion stabilization, biointerfaces and cell-surface recognition in biomedical applications, and ordered surface arrays in bionanoelectronics, can be obtained and all belong to the possibilities using ferritin (Figure 14).

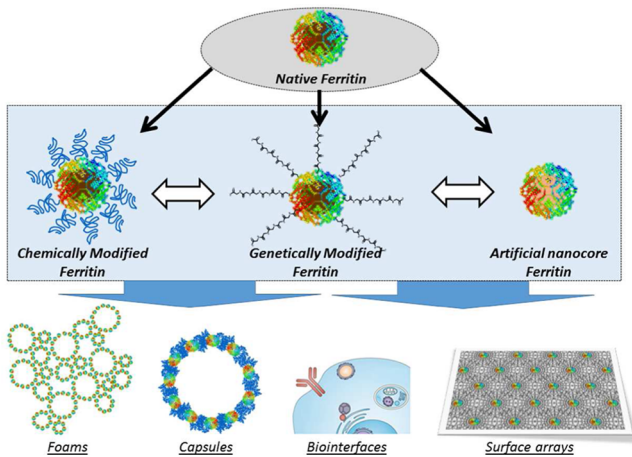


Figure 14. Schematic representation of the use of ferritin in foams, capsules, biointerfaces, and solid two-dimensional arrays.

4.1. Ferritin Adsorption and Assemblies at Fluid Interfaces

During the course of the Protein Array Project at Tokyo University in Japan,²⁰³ the adsorption and manipulation of two-dimensional arrays of ferritin on various surfaces and interfaces have been investigated in great detail.^{204–207} Often, three-dimensional protein crystals for conventional diffraction techniques are hard to obtain. Progress in electron microscopy allows high-resolution images from monolayers, which can contribute significantly to resolving structures of large biomacromolecules and complexes. The procedures, however, require well-ordered two-dimensional crystalline arrays. Image reconstruction techniques then can be used to elucidate the crystalline structure of protein assemblies at interfaces.

The monodisperse properties of ferritin or bionanoparticles in general make them readily crystallize in regular patterns on surfaces if they have sufficient lateral mobility but remain adsorbed at the interface. Aggregation has to be avoided. Both factors are critically dependent on the interface and solution conditions, which influence interparticle interactions. Further, directed interparticle interactions mediated by heavy metal ions can be important for the stabilization of specific crystal lattices.^{207,208} Denaturation can also affect the formation of regular arrays. The preparation of a well-defined sample, that is, without aggregates or natural structural inhomogeneities, is a prerequisite for a successful defect-free monolayer formation. Thus, recombinant ferritin devoid of the natural subunit inhomogeneity was frequently used or natural samples recrystallized and the monomer fraction separated by gel filtration.

The formation of regular 2D-arrays of ferritin at the water–air interface depends critically on solution conditions. The presence of divalent cations like cadmium was shown to be necessary to stabilize the hexagonal arrays of wild-type

ferritin.^{205,206} In a Langmuir–Blodgett setup, the ferritin solution was injected into the aqueous subphase, which had a higher surface tension than the protein solution (2% glucose, 0.15 M NaCl, 10 mM CdSO₄, 10 mM MOPS or MES, pH 5.7). The buoyant ferritin solution rose to the surface and spread on it with much less disturbance of the water–air interface. The initial formation of a thin protein film from unfolded protein provided an ideal substrate for the adsorption of intact ferritin and subsequent crystalline assemblies.²⁰⁶ The injection of small amounts of glutaraldehyde solution as fixative solution preserved the assembly better, and besides hexagonal arrays (molecular packing corresponding to the (111)-plane of the 3D-crystal), also square lattice crystal patches (molecular packing corresponding to the (100)-plane of the 3D-crystal) were observed.^{205,207,208} Thus, wild-type ferritin can assemble in different molecular orientations, either with its 3- or 4-fold axis perpendicular to the 2D-crystal plane. The preferred formation of the hexagonal lattice in the presence of cadmium ions in the subphase is attributed to the salt bridge between the strong chelating interactions of the carbonyls of Asp-84 and Gln-86, which are located around the 2-fold symmetry axis. If these residues are replaced by a neutral amino acid (serine), the apoferritin particles arranged in a new lattice with the 2-fold symmetry axis perpendicular to the crystal plane.^{207,208} Regions of alternating electrostatic potential on the protein coat can explain the preferred formation of this lattice type over the hexagonal crystal. High-quality 2D-crystals for 2D-protein crystallography using an electron microscope were also obtained by spreading on mercury in the presence of glucose, which stabilized the mercury–protein interface; however, experimental efforts were much higher than for the aqueous subsurface spreading method.^{207,209–211}

For the formation of regular large area ferritin arrays at the liquid–air interface, a conclusive scenario was considered where ferritin structures adsorb and assemble into regular patterns with unfolding occurring in the aerial phase while a layer of protein which resides in the aqueous phase remains intact.²⁰⁶ Adsorbed layers at the interface, formed by either an initially spread film from unfolded proteins,²⁰⁶ charged polypeptides like poly-1-benzyl-L-histidine,^{212,213} sugars,^{209–211,214} or positively charged surfactants,²⁰⁴ can strongly aid the formation of large area regular ferritin arrays. They can form a protective layer, which prevents direct contact with the apolar phase and decreases denaturation of the protein at the interface. Further, electrostatic interactions can facilitate the adsorption of ferritin on the interface of the spread molecules.²¹² No crystalline or patchy assemblies were found for arrays, which were picked from Langmuir films of surfactants like stearic acid methyl ester, stearyltrimethylammonium bromide, or stearic acid/cholesterol with ferritin in the subphase.^{204,215} Polycationized ferritin did not adsorb on a bacterial S-layer as reported by Bergkvist et al.²¹⁶

The kinetics of protein adsorption at liquid interfaces can be conveniently followed by pendant drop tensiometry. Nagayama and co-workers used mercury in aqueous ferritin solutions but did not draw detailed and substantial conclusions about the formation of ferritin layers.^{210,211} Jutz et al. investigated the adsorption of ferritin and other proteins and bionanoparticles at the water/decane interface and established an interfacial tension isotherm.²¹⁷ The recently awoken interest is certainly attributed to the revival of particle stabilized emulsions (Pickering emulsions, Figure 15)²¹⁸ and the recent progress

in quantitative modeling of protein adsorption isotherms and kinetic curves.^{219–221}

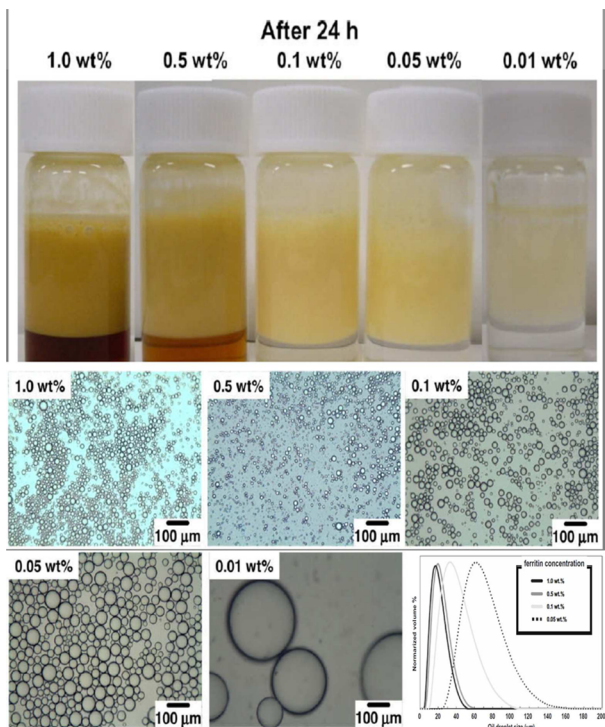


Figure 15. Digital photographs of ferritin-stabilized “Pickering-type” n-dodecane-in-water emulsions at various concentrations of ferritin (0.01–1.0 wt %) and optical micrographs of the corresponding emulsions with corresponding mean oil droplet diameters by laser diffraction measurements. Reprinted with permission from ref 218. Copyright 2009 Elsevier.

The ferritin–polymer conjugates are very suitable to direct the deposition of protein structures to a certain site. For this, two different approaches were taken. First, Emrick and co-workers used the poly-PEGMA (poly ethylene glycol methacrylate) ferritin conjugate to direct its assembly toward certain domains in phase separated block copolymer thin films of polystyrene-*b*-poly(ethylene oxide). It was found that the block copolymer structures were unaffected by the incorporation of the conjugates and that, due to the ethylene glycol polymers on the ferritin, this was directed toward the PEO-phase.¹¹³ Second, the group of Böker used PNIPAAm

decorated ferritin as a structure for interface stabilization.²²² The interface directed self-assembly in combination with cross-linking of the polymer and stable capsules composed of a polymer matrix with embedded proteins was obtained. The capsules were versatile and stable enough to form o/w, w/o capsules as well as o/o and w/w after transferring the collected capsules to the solvent of opposite polarity creating soft flexible shelled capsules (Figure 16). Additionally, when the ferritin–polymer oil–water emulsions were treated with extrusion with subsequent cross-linking, more complex interface stabilized structures were obtained, expanding the simple emulsion system.²²³

Co-assembly of ferritin with other types of nanoparticles and cross-linking gives rise to multifunctional hybrid films. For example, aqueous buffered ferritin solution was vigorously shaken with a toluene solution of aldehyde-capped CdSe-nanodots. Depending on the ratio of the aqueous and organic phase, oil-in-water or water-in-oil emulsions were created.²²⁴ The aldehyde groups on the CdSe-nanodots cross-linked with the amino groups of ferritin to build stable films from the mixed particles assembly. If no reduction of the acid-sensitive imine bond is performed, the capsules are degradable upon pH-change, which can be used for applications with triggered release. Norbornene-functionalized ferritin and CdSe quantum dots enabled Grubbs-catalyzed ring-opening metathesis polymerization to form thin stable films of up to 1 cm². Dual functionalization of ferritin with a fluorescent dye allowed two-channel confocal fluorescence microscopy on the formed films.

The adsorption of ferritin to lipid films was the first prepared two-dimensional array of ferritin.²²⁵ However, a satisfactory encompassing study has not been pursued yet. An early report pointed out differences in the adsorption behavior of ferritin to Langmuir films (i.e., lipids and lipid mixtures at the water/air interface) and to Langmuir–Blodgett films (i.e., lipid films that were transferred to a solid substrate).²²⁶ The adsorption kinetics was investigated by light reflectivity at the fluid or by total internal reflection fluorescence at the solid interface. Obviously, electrostatic considerations are not the only driving force. Different lipid mobility in the two fluid films led to different matching of the lipid head groups with the ferritin surface chemistry and thus an altered adsorption behavior. A structural investigation, for example, whether ferritin forms regular assemblies, was not pursued. Clemente-León and co-workers used the same stearic acid methyl ester/eicosic trimethylammonium bromide lipid mixture as Fromherz 36 years before (although they used the primary eicosylamine and

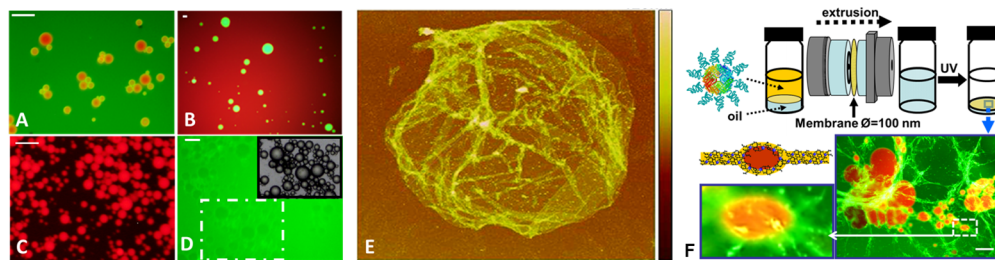


Figure 16. Fluorescence microscopy (overlay) images of emulsion of (A) BTF + Nile Red in water + fluorescein with Fer-NIPAAm-DMIAAm, cross-linked. (B) Water + fluorescein with Fer-NIPAAm-DMIAAm, in toluene + Nile Red, cross-linked. (C) Capsules of (A), collected and redispersed in BTF. (D) Capsules of (B), collected redispersed in water without fluorescein. The inset shows the bright field image of the w/w capsules. Scale bars represent 100 μm. (E) Scanning force microscopy height image $32 \times 32 \mu\text{m}^2$, $\Delta z = 250 \text{ nm}$, of a collapsed ferritin-PNIPAAm cross-linked capsule. Reprinted with permission from ref 222. Copyright 2011 Royal Society of Chemistry. (F) Extruded emulsion in combination with cross-linking provides more complex interface stabilized systems. Reprinted with permission from ref 223. Copyright 2012 Elsevier.

not the methyl quaternized derivative) and found the same optimum mixture of 4:1.^{225,227} Surface pressure–area measurements showed a strong expansion of the area (expressed per surfactant molecule), which is caused by the ferritin interaction in the subsurface layer with the mixed lipid monolayer. Brewster-angle microscopy (BAM) images showed qualitatively that no homogeneous films at any surface pressure were formed, and UV-vis analysis of multiple deposited LB-films confirmed that no complete monolayer was observed (surface concentration of $(6.0 \pm 0.5) \times 10^{-13}$ mol/cm² per monolayer, corresponding to a mean area per ferritin molecule of $28\,000 \pm 2000$ Å² vs the area of a ferritin of 11 300 Å²). Magnetic measurements of the LB films were more or less identical to that of ferritin in solution.^{227,228} This result is not surprising if it is assumed that the magnetic nanoparticles are well isolated from each other by the protein shell, which is preserved also in LB films. Thus, no interaction of the particles can be expected. Liposomes have also been employed as matrix for the assembly of ferritin by electrostatic interactions or ligand–receptor interactions.²²⁹ At pH 5.8, that is, above the isoelectric point of ferritin, the formation of an ordered shell around the positively charged liposomes from hexadecyl trimethylammonium bromide (HTAB) was observed. Fixating with glutaraldehyde was an efficient way of stabilizing the liposomes and liposome–ferritin assemblies. Favorable or neutral electrostatic conditions were also necessary for ferritin adsorption via specific interactions, for example, between liposomes with 10% biotinylated lipid and avidin-tagged ferritin particles or between liposomes with 1–2% cholesterol-mannan and Concanavalin A-tagged ferritin in the presence of Mn²⁺ or Ca²⁺.

Although the formation of 2D-crystalline arrays at liquid–liquid interfaces is experimentally a delicate task, Yoshimura and others have managed to produce excellent arrays of ferritin and Dps loaded with inorganic minerals over large areas by picking up self-assembled monolayers from the liquid interface.^{120,174,213,230,231} Under not too harsh conditions, the protein moiety can be removed, and arrays of inorganic nanodots were obtained. Unfortunately, the experimental difficulty of this procedure makes the fabrication of arrays by this method unsuitable for device fabrication. Simple droplet evaporation methods, convective assembly, or spin-coating on polyelectrolyte layers yielded dense arrays with no crystalline order.^{232–234} However, such irregular quantum dot arrays prepared from ferritin with various different mineral cores were proven suitable for application in nanoelectronics.^{232,233}

Generally, ferritin is not soluble or stable in organic solvents and does not prefer to reside in apolar domains, for example, in polymer blends. However, the combination of the very versatile ferritin particles with polymers that can adopt complex self-assembled structures would be a noteworthy goal. As presented above, ferritin with some solubility in organic solvents can be produced through alkylation.¹⁰⁹ Such modified ferritin particles were adsorbed on thin cuts of a microphase separated homopolymer blend of poly(desaminotyrosyl tyrosine dodecyl ester carbonate) (PDTD) and poly(epsilon-caprolactone) (PCL). At pH 5.8 the unmodified ferritin mainly adsorbed on the PDTD matrix, while the alkylated particles selectively adsorbed on the PCL domains.¹⁰⁸ Ferritin grafted with poly(ethylene glycol methacrylate) was also sufficiently hydrophobic to allow mixing with polystyrene-*b*-poly(ethylenoxide) block copolymers in DMF.²³⁵ A thin film with cylindrical PEO-microdomains was obtained in which the polymer-grafted ferritin particles assembled preferentially. The microdomain

size was dependent on the graft chain length. Adsorption of ferritin on UV-treated microphase separated polystyrene-*b*-poly(methyl methacrylate) diblock copolymers was found to occur majorly on the polystyrene ridges. Electrostatic repulsion of the negatively charged acidic PMMA and ferritin (pH 6.5) and hydrophobic interactions were suggested as reasons.²³⁶ Similar considerations are valid for the adsorption of ferritin on films of PCL–PDTD blends.²³⁷

The preparation of polyelectrolyte films through layer-by-layer assembly (lbl) has been developed to be one of the most versatile and successful methods for the preparation of functional thin films. Naturally, also proteins have been incorporated including ferritin.²³⁸ In alternating layers with poly(ethylene imine), ferritin as the outermost layer shows a patchy structure with islands of 150–200 nm, which are presumably aggregated ferritins. The surface appeared rough (3.20 nm) with significant height differences. Finishing the lbl assembly with an PEI layer produces a smoother surface (roughness 1.28 nm). The electrostatic adsorption on anionic poly(sodium 4-styrenesulfonate) (PSS) or cationic poly(diallyldimethylammonium chloride) (PDDA) was investigated in detail by quartz crystal microbalance measurements.²³⁹ Both apoferritin and ferritin had an adsorption maximum around a pH near their isoelectric point. AFM revealed the formation of aggregates at pH 6, while adsorption at pH 10 resulted in a much more uniform adsorption pattern with a thickness of around 10 nm. Frequency shifts leveled off after approximately 2 h, and the maximum shifts as a function of the ferritin concentration could be described by the Langmuir model, probably a result of the electrostatic screening due to the high salt content. The consistent observation that apoferritin absorbed at lower levels than ferritin with an iron core was hard to explain. In an elegant approach, Shiba and co-workers prepared bioinorganic thin films via a biomimetic inspired lbl process.^{240,241} They recognized that peptide aptamers not only bind specifically to certain inorganic surfaces, but often sustain mineralization reactions of the substrate materials. For example, ferritin with an N-terminal Ti-binding sequence (minT1-LF) did not only bind preferentially to silicon or titanium surfaces (natural oxide layer) but precipitated tetramethoxysilane within a short time.²⁴⁰ Consequently, this binding opens new routes for biomimetic layer-by-layer assemblies to integrate thin inorganic layers. For example, after formation of a minT1-LF monolayer on a titanium substrate, incubation in TMOS led to formation of a silica thin film, which forms a new binding surface for minT1-LF and so forth.²⁴⁰ This process could be conveniently followed using a quartz crystal microbalance, and control experiments supported the suggested mechanism. Moreover, as the core does not influence the interactions of the aptamers on the outer protein shell and their binding to surfaces, ferritin/silica multilayers with different inorganic ferritin cores were prepared. Investigations of thin cross sections prepared by ion milling with TEM and EDS mapping gave a nice visualization of the layered structure. The approach worked also for patterned titanium surfaces and incubation in Ti(IV) bis-(ammonium lactate)-dihydroxide.²⁴¹

The step from dense to crystalline arrays of bionanoparticles is only a first step to a programmed and defined assembly to complex structures. Ligands that mediate specific binding are useful, for example, biotin–streptavidin coupling or via the sticky ends of complementary DNA strands. In solution, the situation is even more difficult, and less well-defined aggregates

are obtained if polyvalent bionanoparticles interact via multiple linkers with several other particles. Li and co-workers functionalized ferritin with biotin and could show the reversible network formation of ferritin.²⁴² Ferritin–gold nanoparticle networks through hybridization of surface bound complementary single-stranded oligonucleotides could be reversibly dissolved upon heating over the melting temperature for the duplex hybridization of 54 °C.²⁴³ Simple electrostatic association led also to defined aggregates. Cationic FePt or Au nanoparticles formed aggregates with ferritin upon electrostatic interaction. The coupling of magnetic FePt with ferritin particles led to an increase of the blocking temperature as a consequence of the enhanced magnetic interaction of the magnetic cores.²⁴⁴

4.2. Ferritin Immobilized on Solid Surfaces

Hierarchically ordered two- or three-dimensional layers are of great interest for the preparation of functional hybrid materials. By combining techniques like contact printing and protein ligation, it is feasible to create ordered arrays of biological structures. This is useful for sensor applications but also electronic devices. Because of the great versatility of ferritin with respect to incorporation of synthetic species as well as the modification of the protein exterior, it is often used as a tool for deposition onto solid substrates. In this section, different approaches of such structures will be discussed.

4.2.1. Covalent Attachment of Ferritin. Covalent attachment of ferritin was achieved via conventional immobilization and cross-linking strategies. Domínguez-Vera et al. used gold surfaces covered with *N*-succinimidyl-3-(2-pyridylidithio)-propionate (SPDP) for reactive immobilization of ferritin via amide formation between protein-amino groups and the NHS-ester of SPDP. A dense and, as expected, irregular layer was formed.²⁴⁵ A similar result was obtained with self-assembled monolayers (SAMs) formed from various dithiobis-(succinimidyl alkanoate)s, although imaging was poor.^{117,246} Lam et al. reported on the spatially selective immobilization of ferritin on a superconducting quantum interference device (SQUID).²⁴⁷ For this, the top of a PMMA resist layer on Nb/Au was etched by electron beam lithography, and the exposed gold surface of the nanobridge was functionalized with a self-assembled layer of 3-mercaptopropionic acid to which in a second step ferritin was conjugated via NHS-EDC coupling. The amount of ferritin was calculated from the charge for complete electrochemical reduction of the core. A surface charge corresponding to 66–75% of the theoretical surface charge of 8.0×10^{11} ferritin particles cm^{-2} with an average loading with 3000 iron atoms was observed in qualitative agreement with the AFM of the surface assembly. The same cross-linking strategy was frequently used to prepare stable electrodes to study the electrochemical iron core dissolution or reconstruction.^{248,249} Evidently, the reverse, that is, functionalization of ferritin and adsorption to bare surfaces, should be possible as well. Spatially selective adsorption of thiolated ferritin particles was achieved on regular hexagonal arrays of gold dots, which were produced by diblock copolymer micelle lithography. Because of electrostatic repulsion, only one ferritin particle could be deposited on the dots with a diameter of 22 nm.²⁵⁰

4.2.2. Electrostatic Interactions on Solid Interfaces.

The site-specific deposition of ferritin is of high interest for the construction of nanodevices. Masuda reported on the preferred adsorption of ferritin on a gold disc, which was fabricated with

an anodic porous alumina substrate.²⁵¹ Earlier, a detailed study of the adsorption of ferritin to gold surfaces with quartz crystal microbalance (QCM), surface plasmon resonance (SPR), X-ray photoelectron spectroscopy (XPS), and atomic force microscopy (AFM) was pursued by Caruso et al.²⁵² The main results of these investigations are that ferritin forms a submonolayer with a thickness of 4.6–4.8 nm for the dry film, corresponding to a surface coverage of 6.3 mg/m^2 . Adsorption kinetics on gold measured by QCM followed Langmuir behavior. While SPR suggested that adsorption was completed after 200 min, the frequency shift in QCM already leveled off at 100 min. The film thickness in phosphate buffer was determined to 13.7 nm with SPR and thus is in good agreement with the actual size of ferritin. AFM employed under standard conditions had to struggle with severe artifacts from tip convolution effects and clustered ferritins. Frequently, no regular assembly of the first ferritin layer (monolayer) on gold was observed. Similarly, ferritin showed on top of dried ferritin multilayers regular hexagonal or orthogonal patterns, but upon decreasing the applied ferritin concentration only disordered and aggregated structures were observed on quartz.²⁵³ The strong interactions with surfaces do not allow the formation of regular structures, while mobility on an already adsorbed layer of ferritin is sufficiently high that ferritin particles can form regular structures on higher layers during drying. Submonolayer assemblies formed a meander-like island structure upon surface-induced aggregation by surface forces and intermolecular-attractive interaction upon drying.^{254,255} Such elongated layer structures were quite closely described theoretically with a model for reversible diffusion-limited aggregation.²⁵⁴ Crucial parameters for evolution of such elongated patterns in the model were considered to be the influence of the nearest neighbors, an increased dissociation probability for high surface coverage, as well as diffusion from the surface into the bulk solution. The selectivity of adsorption on gold, alumina, or other surfaces depends on the electrostatic surface potential, ferritin concentration, buffer pH, and time of incubation. The surface potential of ferritin particles can be tuned through the solution conditions, that is, ionic strength and buffer pH value. The isoelectric point of ferritin is at pH 4.5. Poór et al. showed with QCM that changing the pH to 7.5 and back to 5.0 by injecting KOH or HCl induces partial desorption and readsorption, respectively, of ferritin adsorbed on gold. Approximately 50% of the initial adsorbed amount was released independently of the initial adsorption time or adsorbed amount.²⁵⁶ Similarly, the different surface electrostatic potential, hydrophobicity or hydrophilicity, of a freshly chemically etched silicon surface and a silicon oxide pattern can be used for spatially selective ferritin deposition.²⁵⁷ The salinity plays an important role. If the salt concentration is high enough, charges are screened and electrostatic interactions are shielded; that is, the main interaction with hydrogen-passivated silicon is of hydrophobic nature, and the surface coverage remains fairly constant throughout a range of pH values while adsorption on SiO_2 is low. Surface modification with functional groups can be achieved through incubation with the appropriate silanes, for example, for amino-groups with aminopropyl triethoxysilane. The amino-groups render a positively charged surface at neutral pH or below. Thus, ferritin readily adsorbs from aqueous solutions, while no adsorption is observed on a bare silicon oxide surface.^{258–261} In buffered solutions at pH 5.8, the small negative charges on ferritin are screened and the electrostatic interactive forces are

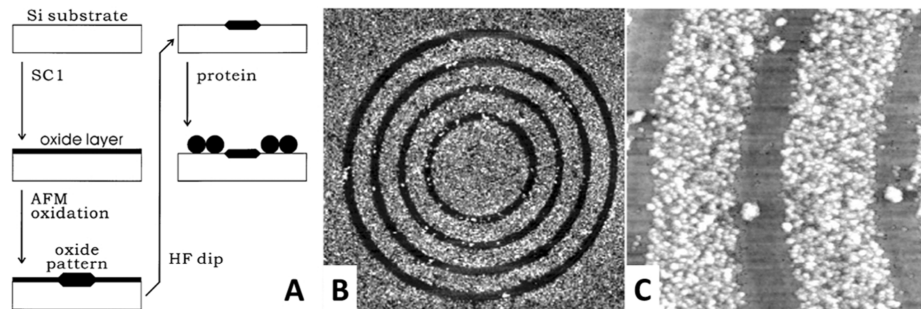


Figure 17. Patterning of ferritin molecules by combining local oxidation nanolithography via AFM (A) and surface functionalization at pH values close to neutral. (B) and (C) display AFM analysis of the adsorbed ferritin molecules (B, $10.8 \times 10.8 \mu\text{m}^2$; C, $2.1 \times 2.1 \mu\text{m}^2$). Reprinted with permission from ref 260. Copyright 2003 Elsevier.

low. Ferritin adsorbs with similar densities on the blank wafer as well as the amino-modified surfaces. Similarly, adsorption also takes place on carboxylated surfaces in PBS at pH 7.4, irrespective of the opposite charges.²⁶² Although functionalization with amino groups increases the adsorption, the maximum theoretical adsorption density was not reached, and few areas remained free. Once ferritin adsorbs, it changes the initial positive net surface charge to negative until it repels other ferritins and inhibits further adsorption. A very positive surface potential with a well-balanced negatively charged ferritin enables, on the one hand, good adsorption electrostatics but does not undermine high-density adsorption. Yamada et al. confirmed that APTES coatings, which have a stronger positive zeta potential, and the ferritin mutant Fe-4, which has a smaller net-negative surface charge than Fe-8, provide high-density surface coatings. Higher density of nanodots can be achieved if *Listeria* ferritin is utilized because it has smaller dimensions. It behaved the same, and furthermore it was shown that, upon drying and a second deposition, the surface potential became more positive again and more Lis-ferr could be adsorbed, reaching almost $1.5 \times 10^{12} \text{ cm}^{-2}$.²⁵⁹ With appropriately chosen conditions, Kumagai et al. were able to place selectively single ferritin molecules on nanopatterned aminopropyl triethoxysilane (APTES)-modified silicon surfaces through electrostatic interactions.²⁶³ In the following detailed study, the authors calculated the barrier of total free energy of interaction of the ferritin–surface system in a buffered solution.^{264,265} They considered contributions from van der Waals and electrostatic interactions and mixing-entropy from the mobile buffer ions. They modeled the electrostatic potential distribution of 100 nm spaced APTES-islands of 15 nm in diameter on the SiO_2 -surface for various Debye-interaction lengths. At short Debye-lengths, van der Waals interactions become dominant, and ferritin will adsorb on both the modified and the bare SiO_2 -surfaces. With increasing Debye-lengths, a repulsive potential barrier is observed above the SiO_2 -surface, but assuming that a potential barrier of 16 kT is necessary to prevent adsorption, only at Debye-lengths of 14 nm is an area in the vicinity of the APTES disk found where $F(\text{total})$ is smaller than 16 kT.²⁶⁵ This could be experimentally verified by adjusting the ionic strength or pH of the buffer solution system accordingly: On each of the islands on the APTES disk, predominantly one ferritin was absorbed but not elsewhere.²⁶⁴ To improve single-particle coverage on larger arrays, for example, for 32–45 nm photolithographic masks, ferritin mutants with higher surface charge densities were used.²⁶⁶ In this way, well-separated single nanodots could be placed on preformed patterns. Calculations can be used to predict the adsorption pattern, and thus in

reverse, surface patterns can be designed, which allow the placement of ferritin particles on preformed patterns. Ferritin deposited via drop casting on APTES-modified Si(100) generally covers the surface in a very dense and homogeneous fashion but without long-range order.²⁵⁸ AFM-based anodic oxidation can be used as a powerful tool for submicrometer nanopatterning. After selectively etching the thin native oxide layer in an HF-etching step, oxide islands on hydrogen passivated surfaces are obtained. Also, surfaces that have been functionalized by incubation with silanes can be oxidatively patterned, and the pattern can be specifically functionalized with a different silane. Thus, it is possible to create positive or negative protein-philic surfaces, depending on the pH of the solution. At pH 3, ferritin is positively charged and thus adsorbing only on locally oxidized areas, which are negatively charged due to trapped charges, but not on APTES- or octadecyl trichloro silane (OTS)-functionalized surface areas. At near neutral pH, ferritin adsorbs on APTES but not on OTS-covered areas. Thus, by appropriate surface functionalization with respect to pH, surface patterning with ferritin can be tuned (Figure 17).^{260,267} A high degree of cleanliness for samples used for nano device fabrication is required. Particularly, polar modified surfaces attract metal and salt contaminations from the buffer solutions. Methyl trimethoxysilane (MTMS) has proven to be useful for adsorbing ferritin from 0.01 M phosphate buffered saline, while HEPES-buffered solutions did not provide the desired results.²⁶⁸ Such modified surfaces adsorbed minimum, if at all, contaminants from the buffer solution as was found by XPS. APTMS surfaces, however, were very prone to adsorb buffer components. Typically, ferritin formed a dense but irregular array on MTMS-functionalized surfaces.

Alternatively, the SiO_2 layer can be coated with a thin film of PEI, which renders a positive charge. At neutral pH, ferritin is negatively charged and adsorption is electrostatically driven. Changing the pH of the solution allows convenient control over adsorption density.^{233,269}

PEG-ylated surfaces are well-known for their protein resistance, and PEGylation changes the interfacial properties of a protein significantly. As mentioned before, unmodified ferritin does not adsorb on bare SiO_2 -surfaces but neither does PEG-ylated ferritin. However, dense assemblies were observed on APTES-modified surface. While no regular assembly was observed for unmodified ferritin, PEG-ylated ferritin had more mobility and was forming hexagonal arrays at the interface.¹¹⁰ The increased mobility was confirmed by fitting QCM measurements with the Langmuir model of adsorption. While data were well overlapping for unmodified ferritin, reflecting

that the condition of irreversible adsorption is fulfilled, the adsorption process of PEG-ferritin had to take a desorption process into account. The successful kinetic modeling strongly confirms the possibility of PEG-ylated ferritin to desorb and readsorb, thus forming more regular arrays (Figure 18).

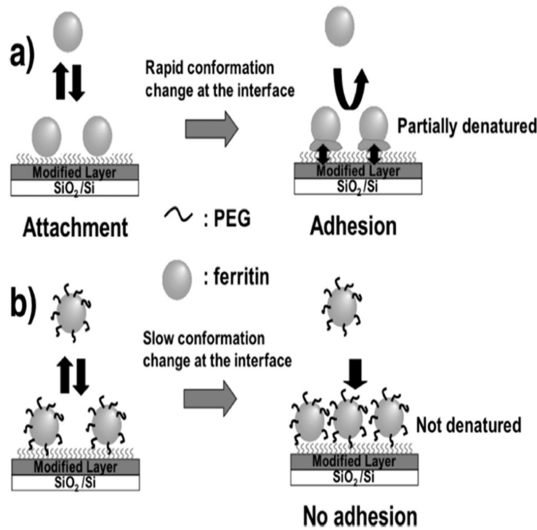


Figure 18. Illustration of the adsorption difference on the surface between (A) unmodified ferritin and (B) PEG-ferritin. Although unmodified ferritin strongly adheres on the surface at the initial stage of adsorption because of the change in conformation of the interfacial moiety of ferritin (partially denatured ferritin on the surface), PEG-ferritin can adsorb without a change in conformation and has a high ability of desorption on the surface. Reprinted with permission from ref 110. Copyright 2008 American Chemical Society.

Self-assembled monolayers (SAMs) are an easy and versatile means to change the properties of surfaces or to provide functional groups for covalent attachment. For example, carboxyl-linkers for ferritin-adsorption on gold were used.^{262,270,271} Unfortunately, this approach showed the presence of large aggregates on the surface by AFM analysis.²⁶² In a series of SAMs bearing amino-, carboxyl-, methyl-, and hydroxyl-end functionalities, the adsorption was strongest on the amino-functionalized surface, while for the carboxyl- and methyl-functionalized ones only a fifth of the adsorption strength was measured. No adsorption occurred on the hydroxyl-functionalized SAM. The adsorption was measured by cyclic voltammetry.^{272,273} AFM imaging revealed a dense but disordered monolayer of nonaggregated ferritin particles on the amino-terminal SAM, but calculation of the surface coverage gave a value of 74–79% only (based on 3000 iron atoms/ferritin core and 8.0×10^{11} ferritin particles cm^{-2}). QCM showed stable monolayer formation after 20 min, and calculation of the adsorbed mass pointed to a nearly complete monolayer. The surface morphology was similar for amino-alkanethiol SAMs on gold with different chain lengths.^{273,274} The amino-undecanethiol SAM, however, introduced such a large spacing between the electrode surface and the ferritin particle that no electron transfer occurred to the iron core anymore.

A controlled immobilization of proteins or other biomolecules are of interest for the construction of diagnostic or therapeutic devices in the emerging areas of nanomedicine. Dip-pen nanolithography, for example, can be used for the

transfer of biomolecules onto surfaces to create specific patterns. In this technique, an AFM tip is immersed into a protein solution and then brought into contact with a surface. If this is done on a TEM grid, the iron oxide core allows the direct and easy evaluation of the number of deposited ferritin particles. The number of transferred structure depends on the initial ferritin concentration, and the dimension of the dot generated by the tip can be controlled by adjusting the tip–substrate contact time. Bellido et al. showed that by this technique a controlled number of ferritin particles could be transferred to various surfaces.^{275,276}

The bionanoparticle can be further processed also in an adsorbed state. Under mild conditions, the protein shell can be removed and the mineral core reduced to the respective metal particles (see below).^{213,230} Ferritin can be used as a functional scaffold or in postdeposition mineralization to create functional surfaces. Holo-ferritin, which was adsorbed on APMS-modified silicon surfaces by short immersion into phosphate buffered ferritin solution (pH 7), could be slowly demineralized. Addition of the strong chelator, nitrilotriacetic acid (NTA), causes a slow degradation of the iron core through exchange via the pores in the ferritin capsid. Upon different times of incubation and subsequent heat treatment to remove the organic matter, well-distributed, increasingly smaller iron oxide nanoparticles on the silicon surface were obtained.²⁶¹ Having established the sigmoidal curve diameter versus immersion time, the size-controlled synthesis of nanodots immobilized on the surface can be realized. After approximately 30 min, a nearly complete dissolution of cores can be achieved; however, few intact cores remained, indicating that a small amount of ferritin particles was not accessed by NTA.

4.2.3. Specific Interactions. Defined interactions deserve special consideration as they represent important ways to construct complex bionanoparticle structures or allow the defined deposition and orientation on patterned surfaces. Binding peptide sequences with affinity for certain surfaces can be genetically fused to the capsid protein (as previously described). Thus, gold binding peptides that were fused to the N-terminus of recombinant horse L-chain ferritin subunit guided the preferential binding of ferritin to gold patterns on surfaces.²⁷⁷ Sano et al. engineered ferritin particles with a high affinity for TiO_2 -surfaces and created a high adsorption capacity.⁸ The binding and dissociation kinetics and affinity to TiO_2 -surfaces were investigated in detail with QCM and SEM.^{241,278} While freed aptamers can show very diminished or even none specific binding properties, binding peptides that are expressed on the filaments of phages or on other polyvalent heterologous substrates usually show strong affinities to the respective inorganic material. Thus, the dissociation constant of the tagged ferritin for titanium was 3.82 nM, as compared to 13.2 μM for the parental aptamer. Multivalency and/or a cooperative effect of multiple interacting peptides contribute to that observation.²⁴¹ The high affinity enables the formation of stable and specific decoration of patterned surfaces.^{241,278,279} The pH had a further discriminating effect on the adsorption on Ti- and SiO_2 -surfaces. While adsorption on titanium surfaces was nearly independent from the pH of the solution, adsorption on SiO_2 was higher at higher pH with a prominent minimum at pH 7.8.²⁷⁸ Usually, the adsorption via binding peptides led to formation of dense but irregular assemblies. However, 100 nm large hexagonal titanium patterns guided the formation of ordered arrays. Obviously, the corner edges of the hexagonal patterns initiated the nucleation and formed the template for a

regular hexagonal close-packed array.²⁷⁸ The sequence specificity of the binding strength of the hexapeptide aptamer was investigated by force–distance measurements with a ferritin-coated AFM tip and silicon oxide and titanium oxide surfaces.²⁸⁰ While the long-range interactions were mainly of electrostatic nature and could be screened at high ion concentrations, the adhesion forces did not depend much on the ion concentration but on the presence of arginine. A molecular model of the peptide aptamer and its interaction with titanium surfaces was presented. Regular arrays of ferritin tagged with carbon-affinity ligands were obtained in PIPES buffer.²⁸¹ The weak specific interactions with the surface and screened protein–protein interactions are important for regular 2D-assemblies. If modified ferritins were spread on non-hydrophilized carbon surfaces, strong and irregular binding due to hydrophobic interactions was observed, similarly as for unmodified ferritin. As the interaction with the surrounding is mediated solely through the shell, the formation of the arrays was independent of the core particles entrapped in the protein shell.^{279,281}

5. ELECTROCHEMICAL PROPERTIES OF FERRITIN

Although ferritin is itself not a redox active protein, an electron transfer step is involved in the formation or dissolution of the iron core. Thus, ferritin shows some electrochemical signature. For the investigation of the electrochemical properties, ferritin was frequently deposited on solid surfaces, for example, indium tin oxide (ITO),^{282–284} bare gold surfaces,²⁸⁵ or gold surfaces modified with SAMs.^{248,249,270,271,273,286}

Zapien and co-workers investigated ferritin, which adsorbed under high ionic strength ($\mu = 1.0\text{ M}$) onto ITO.^{283,284} From the charge under the initial cathodic peak, they calculated a packing density of roughly a monolayer, based on the assumption that ferritin contains an average of 1500 iron atoms. This maximum density was achieved after adsorption over 60 h. The ferritin layer was electrochemically active during cyclic-voltammetric scans. In the initial cathodic scan at potentials of -0.62 V (phosphate buffer) a pronounced reduction peak was observed, while in the anodic scan at a potential of -0.19 V , an oxidation peak appeared (vs Ag/AgCl). XPS, however, revealed that the reduction process was not accompanied by a significant release of iron from the adsorbed ferritin layer and the substantial decrease of electrolytic charge in the anodic and second cathodic peak is not due to a loss of iron into the solution. On the other hand, EDTA at a concentration of 10 mM could mobilize and complex iron after electrochemical reduction and inhibit anodic oxidation. Contrasting the initial assumption that ferritin can be reconstituted during anodic oxidation at potentials above 0 V (vs Ag/AgCl) with ammonium iron(II) sulfate,²⁸⁴ XPS revealed that iron was deposited directly on the ITO electrode, which was confirmed by a ferritin free control experiment.²⁸³ The experiment of reconstituting ferritin aerobically at the electrode at open circuit potential in the earlier report was not subjected to XPS measurements but would have been interesting. The electrochemical pattern between electrochemical and aerobical oxidation was very similar, and while the first one does not allow distinguishing between ferritin core reconstruction and direct deposition on ITO, the latter should be only possible upon catalytic action of the ferroxidase centers. At low ionic strength ($\mu = 0.1$), adsorption occurs only when ITO was dip-coated with an electrostatically adhesive layer of poly(L-lysine) or poly(L-arginine). After 30 min incubation at a ferritin

concentration of $2\text{ }\mu\text{M}$, near full monolayer coverage was achieved as seen by AFM. The electrodes were useful in investigating the electrochemical behavior of ferritin (Figure 19).^{287,288} The electron transfer reactions at ITO electrodes

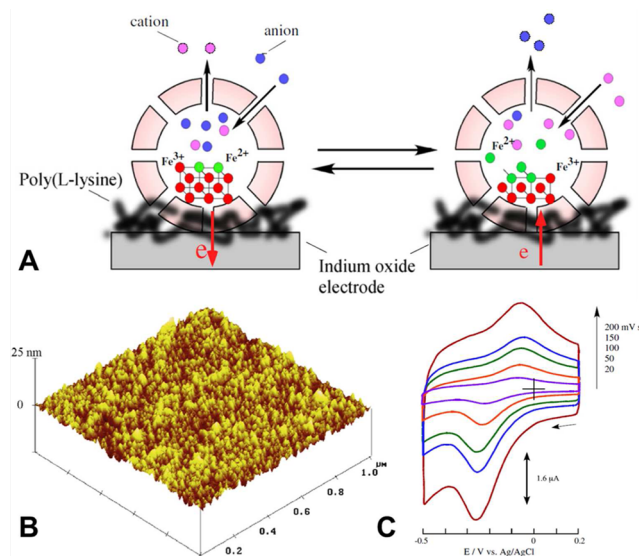


Figure 19. Redox reaction characteristics of ferritin-immobilized onto poly(L-lysine)-modified indium oxide electrodes. (A) A schematic illustration of a ferritin redox reaction on the electrode surface and ion flow during the redox processes; (B) tapping-mode AFM images of a polished indium oxide electrode surface with ferritin-immobilized poly(L-lysine)-modified electrode surface; and (C) typical cyclic voltammograms from ferritin-immobilized poly(L-lysine)-modified indium oxide electrodes in phosphate buffer solutions (pH 7). Potential sweep rates: 200, 150, 100, 50, and 20 mV s⁻¹. Electrode area: 0.25 cm^2 . Reprinted with permission from ref 288. Copyright 2008 Elsevier.

became more difficult for cores with low iron contents: Below 2300 atom numbers, the cathodic peak current decreased dramatically, indicating that partially filled ferritin must orient properly at the electrode interface to enable electron transfer.²⁸²

Ferritin containing vesicle dispersions of dihexadecylphosphate (DHP) render electrochemically active films as well. Wu and Hu showed that the ferritin in the DHP film enables an efficient electron transfer to ascorbic acid and displays a sensitive and stable electrode.²⁸⁹

The hydrophobic adsorption of ferritin on a bare gold surface could be induced at negative potentials of at least -0.20 V .²⁸⁵ Increasing ionic strength, ferritin concentration, or adsorption time led to higher surface packing densities. While on pure gold surfaces no electron transfer to ferritin was observed, on carboxylate- or amino-terminated SAMs on gold the electron transfer did occur.^{271–273,286} The cathodic current correlated roughly with the adsorbed particle density as measured by AFM and was highest on amino terminated, followed by carboxyl- and alkyl-terminated SAMs. No current was observed on hydroxyl terminated SAMs.²⁷³ While the first cathodic peak in cyclo-voltammetry was indeed related to the reduction of ferritin iron,²⁷¹ Zapien and co-workers pointed out in a later communication that, similar to the conclusions with ITO, the reoxidation of the mobilized iron is not necessarily occurring inside ferritin with reconstitution of the core.²⁷⁰ Rather, a reduced soluble species of iron was formed, which could be

scavenged with 1,10-phenanthroline or dissolved into the solution by stirring; that is, the released species was not bound to the ferritin layer. On the other hand, the species that formed upon oxidation readily adsorbed and created a new cathodic peak at -0.32 V (vs Ag/AgCl) after the second and subsequently higher cycles. The hindered electron transfer through SAMs with increasing alkyl chain length can be used for selective reduction of ferritin on gold. On surfaces that were patterned with undecyl chains, the core kept his original size, while on areas with shorter hexyl chains, the iron oxide core became significantly smaller after cathodic cycling.²⁸⁶ Functional SAMs also allow for covalent immobilization of ferritin on the electrode surface, for example, via amide formation with carboxyl terminated thiols.^{248,249} A significant negative shift of the initial cathodic peak with increasing chain length of the carboxylate-terminated SAM was explained with the slower electron transfer kinetics. Basically, the electrochemical behavior was very similar to the electrostatically adsorbed ferritin on SAMs or ITO. After dissolution of iron species during the initial cathodic scan, a new redox couple is generated. Because desorption of empty ferritin was not possible in this study, it became evident that the core of apo ferritin cannot be electrochemically reconstituted.^{249,270} However, at zero or slightly positive voltage, reconstitution in ferrous solutions seems possible for natural and recombinant horse spleen ferritins. Tominaga and Taniguchi and Scott and Zapien observed after incubation in iron sulfate at 0 and 0.1 V, respectively, a cathodic peak again close to the original one for holo-ferritin.^{248,272}

Ferritin is not a redox protein itself, and the iron core yields only transient redox properties as the new redox couple after initial cathodic reduction is slowly but steadily fading. Nevertheless, ferritin was used as redox mediator in a biofuel cell between the polypyrrole coated electrode and the glucose dehydrogenase, which was coupled via an NAD⁺/NADH diaphorase layer to the ferritin layer.²⁹⁰ The ferritin layer increased the anodic current for the oxidation of NADH significantly. Fading of the redox activity was not reported.

6. FERRITIN IN APPLICATIONS

Ferritin has become a kind of prototype particle in bionanotechnology, certainly because of the intimate association of inorganic nanomaterials with a soft, highly multifunctional biopolymer shell. Many applications were envisaged in chemistry and (bio-)nanotechnology such as in (photo)-catalysis, as magnetic recording materials, and quantum electronics. Promising applications of synthetic ferritins were also proposed for magnetic resonance imaging, neutron capture therapy, as radiopharmaceuticals, drug delivery systems, and biocompatible fluorescent and electrochemical markers. Because the electronic or magnetic properties of quantum dots depend strongly on the size, any application in nanotechnology requires more or less strictly monodisperse nanoparticles. Protein cages are ideally suited template reaction vessels as they are precisely defined and have identical sizes. Stringent uniformity of size and shape enables the formation of ordered nanostructures via self-assembly. The functionalities of the protein cage provide further possibilities for molecular recognition and functionalization.

6.1. Ferritin in Functional Nanostructured Composite Materials

Smart nanocontainers and nanoreactors have become a field of vivid research in particular in combination with the catalytic properties of metal nanoparticles.^{291–293} Ferritin has been used as such as well as indicated above and therefore holds great promise for functional biohybrid materials as will be discussed in this section.^{294,295}

Stable dispersible and biocompatible nanoparticles are of special interest for applications in nanomedicine and aqueous biological environments. Kim et al. reported on the photochemical reactivity of native ferritin in a redox reaction in aqueous solution.²⁹⁶ The native ferrihydrite core efficiently converted toxic chromium(VI) to chromium(III) when irradiated with visible light. The reduction was faster for ferritin with a higher loading of ferrihydrite. The photophysical properties of ferrihydrite cores were not investigated in detail, but the band gap was estimated to be between 2.5 and 3.5 eV from the onset of the photochemical reduction. Two potential mechanisms were proposed, either diffusion of CrO₄²⁻ ions through the channel and reduction inside in direct contact with the core or electron transfer through the protein shell. The authors put arguments in favor for both possibilities but could not come to an unambiguous result in light of their investigations. The importance of the protein cage could be inferred from control experiments with protein-free Fe(O)OH mineral nanoparticles. The unprotected catalyst precipitated quickly, while native ferritin remained soluble and showed no loss of catalytic activity. The ferritin system prevents complexation with Cr(III) and provides a self-healing mechanism against photocorrosion. Zhang et al. used ferritin in solution or immobilized on porous MCM-41 support for the radical hydroxylation of phenol.²⁹⁷ All experimental results provide evidence that small amounts of released Fe²⁺ ions were solely responsible for the observed catalytic activity according to the well-established radical Fenton mechanism. While pH was decreasing constantly after mixing the reactants, the conversion was strongly increasing just after an induction time of 60 min after which the pH had dropped to 3.8 and some minimum amount of iron leached from the ferrihydrite core. Apoferritin showed no catalytic effect at all. Because ferritin can be reloaded with iron, one can envisage a smart catalyst system of controlled release and uptake of homogeneously solubilized Fe(II). The photoinduced reduction is only truly catalytic in the presence of an electron donor like carboxylic acids or sulfur compounds. On the other hand, without an electron acceptor, ferritin undergoes complete photodissociation with reduction of Fe(III) to Fe(II). While this result shows the possibility of iron leaching and reduction reaction, different pH-dependence of photocorrosion and photoinduced reduction of, for example, cytochrome *c* and viologens allow the conclusion that the major turnover occurs via direct transfer of electrons from the core under illumination.²⁹⁸ Similarly, ferrihydrite-loaded apoferritin could catalyze the photoreduction of copper(II) with concomitant formation of Cu(0) nanoparticles if the reaction was done under anaerobic conditions.¹⁷² Smaller nanoparticles formed in other protein cages like Hsp or Dps are very active catalysts, for example, in biological hydrogen production systems.⁷⁹ Furthermore, it was shown that palladium-allyl-ferritin composites are active in catalyzing the Suzuki–Miyaura reaction,^{190,197} or the gold–palladium bimetallic particles catalyzed the hydrogenation of acrylamide.¹⁶²

The organic protein shell that mediates the interaction with the surrounding enables the well-defined distribution and adsorption of single, non-aggregated inorganic particles on surfaces where they can act as catalytically active particles after the removal of the protein shell. For example, Kirimura et al. adsorbed Ni entrapped in ferritin on amorphous silicon films on glass. After removal of the protein during a UV/oxygen treatment and annealing at 550 °C in N₂, the formation of silicon crystal domains was revealed. The formation of nickel silicide nuclei enabled the low temperature crystallization. The density and domain size correlated well with the initial ferritin nanoparticle distribution and can be position-controlled by appropriate surface patterning.^{299,300} By introducing a silicon nitride cap layer, nickel is filtered by diffusion, and protein contamination of the poly-Si is better avoided. Large crystal grains of up to 220 μm in diameter are obtained, as compared to 3 μm without cap layer, and the surface remains smoother.³⁰¹ Electron backscattered diffraction and pseudo-Kikuchi pattern revealed a radial texture with predominant (111) and (101) orientation normal to the surface. Such low-temperature crystallized thin films are of potential interest for thin film transistors or flat-panel displays.

Single walled carbon nanotubes (SWCNT) have been a topic of intensive research. Potential applications require chemical functionalization of the nanotubes;³⁰² especially the immobilization of proteins on water-soluble carbon nanotubes is considered as a key step in the construction of biosensors, biomedical devices, and the integration of biomolecules in electronic devices. However, noncovalent functionalization of the tubes is important to preserve their electronic characteristics. Chen et al. reported the noncovalent interaction of SWCNT with a hydrophobic pyrene derivative, 1-pyrenbutanoic acid succinimidyl ester, via π-stacking. This method did not destroy the conductive graphitic structure but installed amine-reactive succinimidyl esters, which could be used for covalent immobilization of biomolecules, such as ferritin. TEM showed that no attachment of ferritin occurred on pristine tubes, indicating the absence of physical interactions between ferritin and the graphitic surface of pristine SWCNT.³⁰³ The covalent attachment of biomolecules requires the formation of functional groups on the carbon nanotubes. The introduction of carboxylic groups by reaction with oxidizing acids, ozonolysis, or air oxidation are well-established procedures. Azamian et al. and Jiang et al. used aqueous dispersions of acid-oxidized single- or multiwalled carbon nanotubes for the immobilization of biomolecules.^{304,305} The reaction with ferritin was carried out without and in the presence of EDC. In both cases, strong and dense binding of ferritin was observed at comparable levels. This indicated a predominantly physical interaction, which could not be alleviated by extensive washing or the presence of surfactants. This behavior of strong protein affinity of SWCNT in water was investigated in more detail by Lin et al.³⁰⁶ In agreement with the results of Azamian et al., they found strong adsorption of ferritin at intermediate pH to the oxidized SWCNT. Covalent attachment through EDC was not crucial but was more effective in nanotube solubilization and yielded a more stable conjugation resulting in a less pronounced loss of ferritin during dialysis as for exclusively physically adsorbed ferritin. In contrast, SWCNT with hydrophilic surface coatings had pronounced protein-resistant properties. The strong interaction of ferritin with SWCNT can be completely eliminated after the tubes were functionalized with poly(ethylene glycol) (PEG), which is known to protect

surfaces against protein adsorption. The covalent immobilization of ferritin on the carbon nanotubes changed the electrochemical properties significantly.³⁰⁷ The cyclic voltammogram showed a broad reduction peak at -0.15 V and a strong oxidation peak at 0.22 V. Control experiments confirmed that the oxidation peak stems indeed from tunneling electrons through the protein shell and the redox reaction with the iron core. Increased oxidation times of the nanotubes in acid to generate the acidic functions lead to fragmentation of the tubes. Thus, less ferritin molecules are bound, and the specific capacitance is drastically reduced.³⁰⁸ The influence of different degrees of functionalization with ferritin on the electrochemical properties was unfortunately not investigated. The electronic connection between ferritin and SWCNT enables the fabrication of catalytically active sensor devices. Thus, Dechakiatkrai et al. showed that simple mixtures of ferritin and SWCNTs that were deposited on ITO substrates form an amperometric biosensor, which can be used to electroanalyze the oxidation of the model substrate ascorbic acid. The components alone only gave very small current responses.³⁰⁹

It is well-known that multiwalled carbon nanotubes (MWCNTs) are effective reinforcing materials in polymer nanocomposite materials. Two main problems, both connected with the chemistry of the graphitic interface of the carbon nanotubes, have to be overcome in the synthesis of such materials: (i) an efficient dispersion of the nanotubes and (ii) the interfacial adhesion between the nanotubes and the matrix. Bhattacharyya used the covalent immobilization strategy of Azamian et al. and Lin et al. to prepare ferritin-functionalized MWCNTs.³¹⁰ Dynamic mechanical thermal analysis showed a strong increased storage modulus for poly vinyl alcohol (PVA) films containing 1.5% ferritin-functionalized MWCNTs as compared to PVA-films prepared with the same amount of only acid-treated nanotubes. Correspondingly, the glass transition temperature shifted from 86 to 102 °C. Both properties can be explained by the strong mediating interaction of the polyfunctional ferritin moieties on the surface of the MWCNTs with the PVA matrix. The protein complex was homogeneously immersed within the polymer matrix, which could improve the compatibility with MWCNTs and act as multivalent cross-linking agent, either by intermolecular hydrogen bonding or by possible covalent binding. The same effect was observed for PVA nanofibers, which were electro-spun from PVA/ferritin solutions in water/ethanol mixtures.³¹¹ The ferritin was homogeneously dispersed in the polymeric matrix. The elastic modulus of the reinforced fibers (diameter < 100 nm) was significantly enhanced as measured with AFM and was comparable to previous measurements on CNT/PVA composite films. Electro-spinning of hydrogel nanofibers is a very simple and versatile process for the fabrication of thin scaffolds with high swelling properties as well as surface-to-volume ratios and has considerable interest for the construction of biomedical scaffolds. The fibrous mats prepared from PVA/ferritin were investigated for their mechanical properties.^{312,313} Besides the elastic modulus, tensile strength and elongation at break were all enhanced as compared to the pure polymer hydrogel material. The stress-strain curves of ferritin/PVA hydrogels immersed in buffers of different pH's showed only minor differences in the toughness but were otherwise very stable. While generally filler material introduces a porous structure in the PVA hydrogel, which decreases the mechanical properties, the strong bonding between the matrix and the

protein shell is responsible for much reduced hoop stress at the boundary of the reinforcing material and led to the observed improvement of mechanical properties. Isotonic cycling between pH 4 and pH 9 was completely reversible without creep.³¹³ Because of the superparamagnetic properties of the iron oxide core, such hydrogels can be conveniently visualized by MRI techniques. Upon temperature-induced aggregation of ferritin in the PVA solution before electro-spinning, the transverse relaxation time T_2 and hence the contrast can be tuned.³¹⁴ Uniform and continuous core–sheath nanofibers can be produced by coaxial electro-spinning of two immiscible components. Ferritin tended to precipitate in solutions of poly(2-acrylamido-2-methyl-2-propanesulfonic acid) (PAMPS), a strong anionic polyelectrolyte, and was thus dissolved in water/glycerol mixtures (Figure 20). The matrix polymer was

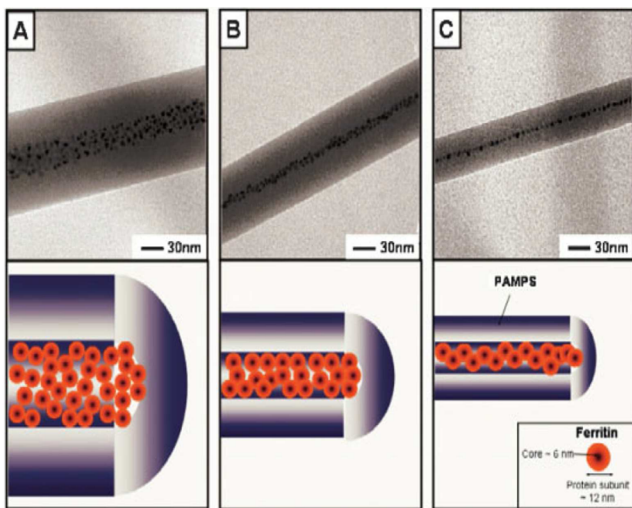


Figure 20. (A–C) TEM images of different width ferritin 1D arrays with PAMPS tubular nanostructures, formed by adjusting the concentration of the PAMPS solution. The schematic illustrations below each TEM image indicate the different widths of the ferritin 1D-arrays and PAMPS tubular nanostructures. Reprinted with permission from ref 315. Copyright 2008 American Chemical Society.

dissolved in ethanol/water mixtures. The tubular diameters are tunable through different concentrations of PAMPS. The width of the 1D-ferritin arrays was determined by the diameter, and an almost linear chain of individual ferritin particles was formed within a 30 nm diameter fiber prepared from a 3 wt % solution.³¹⁵ The process was very robust and highly reproducible as shown by TEM.

The great versatility of the ferritin capsid to house different semiconductors and the alignment in precise long linear assemblies opens exciting prospects for nanowires composed of different materials. Biocompatible fibers, for example, from poly(glycidyl methacrylate) (PGMA), are interesting materials for biomedical applications, in tissue engineering or as polymeric carriers. PGMA provides a rich support with epoxy groups, which allow direct conjugation to amino functionalities of proteins. In a proof of concept, ferritin was immobilized on PGMA nanofibers, and the sparse assembly on PGMA fibers was successfully visualized with TEM and SEM.³¹⁶

The enclosed nanoparticles in ferritin can also be used as efficient catalysts for growing carbon nanotubes (CNTs) by chemical vapor deposition. The interest in the synthesis and engineering of single walled carbon nanotubes concentrates on

addressing (i) control of CNT diameter, (ii) control of chirality, (iii) control of growth direction, and (iv) density control on the substrate surface. Ferritin with the unique possibility to place well-dispersed inorganic nanodots of tunable size in a controlled manner on substrates was soon considered as an ideal catalyst precursor. In a first investigation, Li et al. followed the growth of well-separated SWCNTs from iron oxide nanoparticles derived from ferritin by AFM and TEM.³¹⁷ The core dimensions after oxidative removal of the protein shell were close to the tube diameter distribution of the grown nanotube, thus confirming the expected catalyst tube-size diameter correlation.^{317,318} Thus, removing the aggregates from ferritin preparations or fractionating them according to their weight, that is, core size, yields fairly narrow catalyst size distributions and concomitantly narrow SWCNT diameter distributions.³¹⁹ Observation of nanotubes grown from nanoparticles that were deposited on alumina coated grids by TEM yielded a detailed insight into the growth mechanism.^{317,320} The association of the tubes with one discrete nanoparticle at one end of the closed tubes was clearly identifiable. Furthermore, the nanoparticles and the associated ends of the CNT remained fixed to the substrate, while the other closed end was freely extending out of the support membrane, clearly in favor of the base-growth model. The low efficiency of the CNT growth on nanoparticles and the remarkable length variation were attributed to catalyst poisoning effects, size effects, and structural changes in the catalyst–tube interaction. Kim et al. followed the approach and synthesized with a different chemical vapor deposition (CVD) procedure ultralong SWCNTs.³²¹ A high yield of semiconducting tubes was obtained as a detailed electronic investigation revealed. In the synthesis of monodisperse multiwalled carbon nanotubes with ferritin as catalyst, it was necessary to immobilize the ferritin particles in a matrix formed by $\text{Al}(\text{NO}_3)_3$. Otherwise, diffusion and coalescence of the inorganic cores took place, significantly impeding the controlled growth of MWCNTs.³²² However, this problem was never observed by other authors in the synthesis of SWCNTs. A good superposition of the catalyst particle size distribution with the MWCNT diameter distribution was found but depended on the gas mixture during the CVD process.³²³ While partial loading of ferritin gives relatively easy access to tunable sizes of catalyst dots, the accompanying size distribution directly affects the size distribution of the carbon nanotubes. This problem can be avoided if smaller protein cages are used, which are mineralized to a saturation maximum. Kramer et al. used fully iron oxide loaded Dps and obtained iron core particles of 1.05 ± 0.11 nm in diameter after oxidative removal of the protein shell and reduction.⁹⁴ The narrow size distribution related directly to a very narrow size distribution of the tube diameter of 1.0 ± 0.1 nm as measured by AFM. This exceeds the previous benchmark for the size set by iron oxide nanoparticles, which were formed from iron loaded dendrimers and allowed the formation of nanotubes with 1.4 ± 0.3 nm in diameter.³²⁴ SWCNTs could also be grown unidirectional on the quartz substrate. Durrer and co-workers investigated the adsorption density of ferritin and growth of carbon nanotubes on SiO_2 for integration in FETs.³²⁵ Clearly, a geometrical pattern of the catalyst particles with defined surface density would be advantageous to have a site and number controlled growth of the nanotubes; otherwise, a nanotube “mess” is obtained, unsuitable for microdevice fabrication.³²⁶ For example, patterning of a ferritin layer on a TiN substrate via optical or electron beam lithography of a top-layer negative

resist was done and tested for biocompatibility with PC-12 nerve cells.³²⁷ Ferritin solutions for inkjet printing on aluminum oxide surfaces needed a nonionic sugar-based surfactant as additive, which incorporated ferritin particles in a micellar morphology. The improved wetting properties supported the homogeneous catalyst particle distribution and adhesion prior oxidation treatment and CNT growth.³²⁸ With help of their experience on placing individual ferritin particles on lithographically patterned silica surfaces, Kumagai et al. were able to grow single carbon nanotubes from predefined positions.³²⁹ The plasma-enhanced chemical vapor deposition under a DC electric field made the nanotubes grow vertically, yielding a forest of individual nanotubes. A heat treatment by rapid thermal annealing under oxygen at 500 °C for 10 min was preferable to UV/ozone treatment of the deposited ferritin particles to avoid nanodot migration. Tominaga et al. showed that carbon nanotubes can exhibit also lattice-oriented growth on gold surfaces.²⁷⁴ They used dense arrays of iron oxide cores from ferritin deposited on amino-terminal alkanethiol-modified gold surfaces. A heat treatment removed the organic components without clustering of the inorganic cores. Selective placement of the catalyst and growth of nanotubes in a defined direction is a challenging prerequisite to use CNTs in bottom-up approaches for organic electronics. In subsequent research works, also cobalt-filled³³⁰ or gold-filled apoferritin³¹⁸ was used. Unreached goals are still catalyst nanodots that would promote the selective chiral growth of carbon nanotubes.

The protein shell of ferritin could also be used as the carbon source for the preparation of quasi-spherical fullerene-type multiwall shells (onions) with encapsulated iron nanoparticles. During mild heat treatment, the protein shell was carbonized and formed graphitic shells.³³¹ The dried ferritin suspension was first heated under vacuum with a rate of 10 °C/min to a temperature of 600 °C and held there for 16 h before the sealed glass tubing was subjected to a ramp of 100 °C steps over 4 h and held for 96 h at 900 °C before the sample was brought to room temperature by a similar cooling step ramp. High-resolution TEM showed that predominantly single crystals of the high-temperature modification of iron, γ-Fe (fcc), were formed, which were surrounded by multiwalled graphitic shells. Many empty shells could be found as well. Although the formation of filamental and tubular graphitic structures was observed with other carbon sources in the presence of catalytic iron nanoparticles and the phenomenon of catalytic graphitization is well-known, an explanation or mechanism was not put forward. However, this observation is an unprecedented approach to the formation of nanometric graphitic structures, which could be of high interest in nanoelectronics.

Biological materials contain usually only lightweight atoms and provide thus no contrast in electron microscopy. The inorganic core of ferritin is advantageous in this respect because it features a fully biologically encapsulated iron oxide core, which provides contrast and eliminates the need for staining. Ferritin represents thus a very useful tracer particle because of the inorganic core but also because of its multivalence properties. These features are especially useful to visualize organic assemblies, for example, the encapsulation of ferritin (guest) in lipid nanotubes.^{332–334} Self-assembled lipid nanotubes are size-tunable hosts and display an ideal template for the one-dimensional assembly of nanoparticles.³³³ Because the inner walls are hydrophilic, the protein-coated inorganic particles of artificial ferritins are readily taken up by capillary forces upon rehydration of the tubes. Such assemblies can be

used as building blocks for nanoelectronic devices. Kameta et al. observed the real-time dynamic behavior of ferritin particles inside the tubes by time-lapse fluorescence microscopy. Ferritin, which was labeled with the fluorescence acceptor dye QSY7, was added to lipid nanotubes that were covalently functionalized on their interior with the fluorescence donor dye 4-fluoro-7-nitrobenzofuran. Within a few seconds, the fluorescence of the tubes started to quench from both open ends. The diffusion coefficient of the ferritin particles inside the tubes was around 5 times smaller than that in solution. Control experiments ruled out quenching from exterior ferritin particles. Moreover, the encapsulation of the negatively charged ferritin could be controlled by changing the electrostatic properties of the interior.³³²

6.2. Applications in Semiconductors and Nanoelectronics

Traditionally, semiconductor physics and nanoelectronics have been connected with high vacuum or clean room conditions. Improved lithographic techniques advanced the development of electronic devices, and ever smaller line widths could be achieved. However, traditional UV-based techniques approaching their limits and lithography based on electron beam, synchrotron radiation, or surface probe microscopy techniques are time-consuming and require expensive equipment. On the other hand, biomolecules with nanometer length scales are very well-defined in terms of their shape and chemical structure and possess the inherent ability to self-assembly in bottom-up approaches. The so-called BioNanoProcess²¹³ introduced by Yamashita is one of the first examples of breaking the border between the well-separated fields of clean-room semiconductor-based nanotechnology and wet biological materials for the fabrication of nanoscale electronic structures.^{14,335}

The BioNanoProcess consists of several steps:

- (1) Nanoparticle synthesis inside the protein cavity
- (2) Positioning and alignment/self-assembly on surfaces
- (3) Elimination of the protein moiety
- (4) Reduction and burring in a silicon dioxide layer and usage as electron storage or usage as lithographic mask

While the first issue was the topic of intensive research by many research groups, Yamashita and his colleagues investigated also the formation of two-dimensional crystalline arrays of ferritin at various interfaces. The successful pick-up of ferritin assemblies from liquid interfaces on a hydrophobized wafer and subsequent heat treatment to remove the protein layer with preservation of the crystalline order mark the starting point for application of ferritin nanoparticles for electronic devices.²¹³ The SEM images of such transferred assemblies show well-ordered hexagonal arrays of ferritin particles. The few vacancies indicate the loss of ferritin particles during the transfer process or the presence of empty protein cages, which are not visualized in the SEM. Assemblies transferred to a TEM grid did not show loss of protein particles. Heat treatment at 450 °C under nitrogen flow eliminated the protein shell completely as the disappearance of the amide bands at 1660 and 1545 cm⁻¹ indicated, but the assembly became considerably more disordered at temperatures above 300 °C. The preparation of metal nanodot arrays and integration in semiconductor devices will be a requirement to meet the future challenges in the preparation of nonvolatile semiconductor memory technology.³³⁶

Yamashita and co-workers were focusing on the construction of nanoelectronic devices such as floating nanodot gate memory devices (FNGM) as proofs for the feasibility of the

biological path for fabrication of electronic device components (Figure 21).^{337,338} FNGMs are promising candidates for next

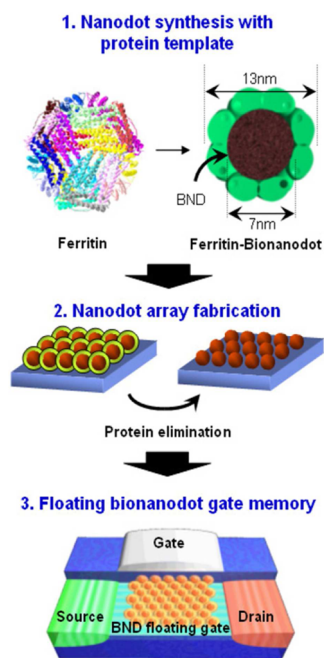


Figure 21. Schematic drawing of the bionanodot-ferritin, apoferitin in which a cobalt oxide (Co_3O_4) nanoparticle is synthesized, and this is utilized in the floating nanodot gate memory (FNGM) fabrication process. It uses the semiconductor nanodot as a charge storage element with the intention of creating a memory device. Reprinted with permission from ref 337. Copyright 2008 IOP Publishing.

generation nonvolatile memory applications. A floating nanodot gate memory has a structure similar to that of a metal–oxide semiconductor field-effect transistor (MOSFET), but an additional nanodot array is embedded in an insulating control oxide layer just above the channel. The gate electrode is used to inject electrons or holes on the dots, which work as charge storage nodes. Ideally, one electron is stored per each dot. The electrostatic potential alters and controls the drain current–gate voltage ($I_D - V_G$) characteristics. The performance of an FNGM is strongly dependent on the structural characteristics of the employed floating gate. A conductive floating plate-type gate has insufficient immunity to local leakage paths, which requires unfavorable thick tunnel oxides. A high density of well-separated, homogeneous nanodots or nanocrystals with narrow size distribution is favorable to further down-scale the tunnel oxide and usage of smaller operating voltages, better endurance, and faster write/erase speeds. It is difficult to obtain enhanced charge storage and long charge retention times with semiconductor nanocrystals, but the potential well-depth can easily be adjusted by using metal nanodots and work function engineering. To achieve this, Yamashita and co-workers employed recombinant apoferitin, consisting of solely L-type subunits. After controlled mineralization in vitro with ferrihydrite^{339,340} or cobalt oxide,^{233,269,337,338,341} homogeneous ferritins with inorganic cores were obtained. Ferritin solutions were spin-cast on a 3 nm thermal oxide on p-type silicon substrate, which has been hydrophilized previously by UV ozone treatment. Alternatively, the SiO_2 layer can be coated with a thin film of PEI or coated with APTES, which renders a positive charge. At neutral pH, ferritin is negatively charged and

adsorption is electrostatically driven. Changing the pH of the solution allows convenient control over the adsorption density.^{233,269} Such prepared ferritin monolayers were reaching densities of $6 \times 10^{11}/\text{cm}^2$ or 75% of the geometrically calculated maximum value. However, a regular assembly cannot be achieved by this simple procedure, but pick-up from liquid interfaces works well.^{213,230} The protein shell and the polymer film, respectively, can be eliminated in an RTA furnace under an oxygen atmosphere²⁵⁸ or by UV/ozone treatment under mild conditions,²³⁰ and the bare inorganic cores were embedded in an 17 nm insulating silicon oxide layer by plasma-enhanced chemical vapor deposition (CVD) using tetraethoxysilane (TEOS). Organic layers are efficiently removed as can be followed from FTIR peak profile of the amide bands or XPS signals from nitrogen and carbon.²³⁰ The electronic properties of the device remain unaffected.²³³ After completion of the device with electrodes, the nonconducting cores had to be reduced to metallic nanodots in a postmetal annealing step. This step was carried out in ammonia plasma³⁴⁰ or in a reductive atmosphere of H_2/N_2 ^{339,341} directly after the deposition of the control oxide in the same CVD system. Reduction of the cores should be possible if the surrounding silicon atoms have a higher affinity against oxygen atoms than the respective metal atoms. On the basis of XPS and EELS measurements, it was shown that treatment with forming gas at 400–450 °C for 1 h will reduce the iron oxide or cobalt oxide cores at least partially to the respective metal nanoparticles.^{337,339,341} In a reductive atmosphere of 4% H_2 in nitrogen, an increase of the Co-peak in XPS was observed for higher annealing temperatures, concomitant with a larger memory window size.³⁴¹ However, a low annealing temperature is necessary to prevent nanodot deformation or diffusing, and 450 °C proved useful. Annealing in a nonreductive atmosphere does not yield (partially) metallic nanodots, and the memory window size of the device was insufficiently low. Cross-section TEM proved nicely the assembly of the layers. The iron or cobalt metal dots with a diameter of 4.6 nm could clearly be identified, and the observed lattice spacing in HR-TEM pointed further to the formation of metallic Fe and Co, respectively.^{340,341} In a detailed investigation, Hikono et al. showed that in the reverse order, that is, first core reduction and then silicon oxide deposition, ferritin is reoxidized and the metallic state of the nanoparticles can only be maintained if nonoxidizing SiN-layers are used.³⁴⁰ Reduction of the ferrihydrate in ammonia plasma required only a mild temperature of 200 °C. Devices with cobalt oxide^{233,269,337,338,341} and ferrihydrite cores^{339,340,342,343} were fabricated. The core embedded MOS capacitors were characterized in terms of their capacitance–gate voltage ($C - V_G$) sweep curves. Wide gate voltage scans induced a flat band voltage shift, and the $C - V_G$ curves displayed a pronounced counterclockwise hysteresis. The hysteresis behavior is a strong evidence for the electron- or hole-injection and confinement to the embedded metal cores at sufficiently large potentials. A narrow gate voltage scan is not sufficient for electron tunneling, and similar to control devices that were prepared without bionanodots, no hysteresis was observed. A control device in which apoferitin was used also did not exhibit hysteresis, indicating the efficient removal of the protein such that it cannot work as a charge trap in the MOS stacked structure. The bias polarity-dependent charge confinement to the discrete Co-nanoparticles could also be shown by monitoring the surface potential change with Kelvin probe force microscopy. The memory window size depends on the V_G

sweep range and amounts to 3.3 V for $-9/+9$ V sweeps. Six electrons are stored per nanoparticle under these conditions. Consistent with the $C-V_G$ curves, the drain current–gate voltage (I_D-V_G) curve showed a clockwise hysteresis for wide gate voltage sweeps. Charge retention was maintained very well with an approximated 10-year memory window of 1.0 V. Also, the endurance test, that is, stressing the memory device with short pulsed bias, did not induce any degradation of the I_D-V_G curve.³³⁷ All of the phenomena can be explained by an efficient injection and excellent trapping of the charges in the metal/metal oxide nanoparticles in the insulating gate layer. The high durability against charge leakage is attributed to the efficient isolation of the nanodots, which work as independent charge storage nodes. A different assembly with a 9 nm HfO_2 tunnel oxide on p-Si and 15 nm thick Al_2O_3 control dielectric on ferrihydrite cores derived from native ferritins showed similar performance characteristics but needs decreased program/erase voltages.^{232,344} The ferrihydrite cores were reduced with high-pressure H_2 -annealing because the lower thermal budget relative to the conditions employing forming gas diminished the Si/ HfO_2 -interface states and improved the device properties because of less trap-to-trap tunneling. This explains further the larger charge retention times and better endurance characteristics for the high-pressure H_2 -annealed samples.

Generally, high- k gate dielectrics as tunnel or gate oxides improve retention characteristics as they exhibit lower leakage currents and higher breakdown voltages. For example, HfO_2 had a 6 times higher dielectric constant than SiO_2 , and a 5 nm HFSiO or HFO_2 tunnel oxide had an effective oxide thickness similar to that of SiO_2 . Devices prepared from ferritin with an iron or cobalt core with hafnium oxide as tunnel and/or gate oxide displayed a much larger memory window and a higher breakdown voltage.^{345,346} The difference is attributed to different charge injection mechanisms. The thin SiO_2 layer with a high energy barrier enables only direct tunneling at sufficient high bias voltages. The physically much thicker hafnium tunnel oxide layers have a smaller barrier height, and charge injection occurs according to the Fowler–Nordheim tunneling. Back tunneling is not easy anymore. To avoid additional capacitances at the bulk-Si/source and bulk-Si/drain interfaces (seen as shoulder in the capacitance–voltage plot, e.g., ref 347), a silicon-on-insulator substrate, that is, fabrication of the drain and source in c-Si on an insulating SiO_2 -layer, was chosen. Devices with high writing and erasing speeds and high reliability were prepared, but the charge retention characteristics were limited by the use of a thin SiO_2 tunnel oxide.³⁴⁸

The size of ferritin restricts nanodot densities to below 10^{12} cm^{-2} . To realize smaller structures with sufficient leakage endurance and memory magnitude, higher densities of floating nanodots need to be achieved, which is possible by using smaller particles. Ferritin from *Listeria* accommodates particles of 4.5 nm ferrihydrite dots. Densities of up to 1.8×10^{12} cm^{-2} were achieved, which even exceeded the theoretical number calculated on the basis of a dense monolayer of particles with an outer diameter of 9.4 nm. Nevertheless, the particles were well-separated on the surface. Here, the 3 nm SiO_2 -top layer of the wafer was modified with APTES to achieve binding of the *Listeria* ferritin. The removal of the protein shell was done by thermal treatment at 500 °C for 10 min instead of UV/ozone as to avoid severe aggregation of the particles on the surface. After embedding of the metal oxide nanodots in a 20 nm SiO_2 -layer, fabrication of Al-electrodes, the MOS structure was annealed for 1 h at 450 °C in H_2/N_2 (10/90). The $C-V_G$ curve showed

clear hysteresis for sufficient wide gate voltage sweeps with a memory window size of 1.5 V for bias voltages of -5 to 5 V.³⁴⁹ The dot density and dot size have a pronounced effect on the charge injection characteristics. Using recombinant horse spleen ferritin and *Listeria* ferritin, two different sized biomolecules with iron oxide cores of 7.0 and 4.5 nm, respectively, are at hand. Furthermore, the core density can be varied through mixtures with nonmineralized protein cages. A series of MOS capacitors with nanodot arrays of different densities were prepared and the capacitance–voltage characteristics measured at 1 MHz with 10 V DC sweeps.³⁴⁷ The number of electrons stored under the applied bias voltage of ± 10 V was calculated to be 2. Finally, by plotting the flat-band voltage shift per unit dot (i.e., $\Delta V_{fb}/p_r$) against the dot density, an approximately linear relationship could be found. This indicates that the charge injected into the nanodot arrays depends on the sum of hemisphere areas.³⁴⁷ Thus, for good charge leakage properties and a large memory window, a thoroughly balanced dot density and size is necessary. This opens the possibility, together with different metal or mineral cores, to realize FNGMs with specific performances.

Hikono et al. reported first on the use of recombinant ferritin for FNGD arrays.³⁴⁰ The difficulty consisted of the isolator properties of the ferrihydrite core, which is not suitable for the construction of the nanodot-MOSFET. Thus, after adsorption of the ferritin on the native silicon oxide layer of a p-type silicon wafer, the organic matter was eliminated from the bionanodot array by exposure to UV-ozone treatment. The ferrihydrite was then reduced by ammonia plasma treatment in a CVD chamber in which immediately after either a 5 nm layer of SiO_2 or SiN was deposited on the device. The authors provided a detailed analysis with high-resolution SEM, TEM, and XPS, which showed that in the first case, insulating iron oxide nanodots were obtained. The reoxidation was avoided when SiN was used. The iron nanoparticles remained metallic. The initial ferritin monolayer showed many defects, and coverage of approximately 75% of the theoretical maximum was achieved, corresponding to a density of 6×10^{11} dots/ cm^2 . The reduced cores were around 2 nm smaller as expected when accounting for the loss of oxygen from the initial ferric oxide particles.

A further useful application of the BioNanoProcess is as bionanoparticle masks for lithography applications in nanoelectronics.³³⁵ In contrast to conventional colloidal particles, the apo ferritin protein cage exhibits absolute uniformity, which can translate to its inorganic core. The assembly of the uniform particles replicates then in the image structure. Thus, the mineralized ferritin particles are ideal nanometer-sized building blocks for masks via a bottom-up approach. In a first report, Yamazaki et al. used inductively coupled plasma (ICP) etching in CHF_3/O_2 , but the harsh method led to aggregation of the iron oxide nanodots and a patchy, lobe-like structured surface.³⁵⁰ Plasma etching is not suitable for sub-10 nm structures because high-energy ultraviolet photons, ion bombardment, and charge accumulation generate defects on the surface. To avoid these problems, an improved procedure of a low-energy neutral chlorine beam source made of an ICP source was employed. The high etching selectivity of silicon to the iron nanoparticle mask is especially useful for the application to ferritin-based masks. After 6 min of etching and removal of the iron core, pillar-like structures of 25 nm height and a top diameter of 7 nm were obtained, which is exactly the diameter of the iron core.³⁵¹ The columns were slightly tapered. The nanocolumn height and etching time

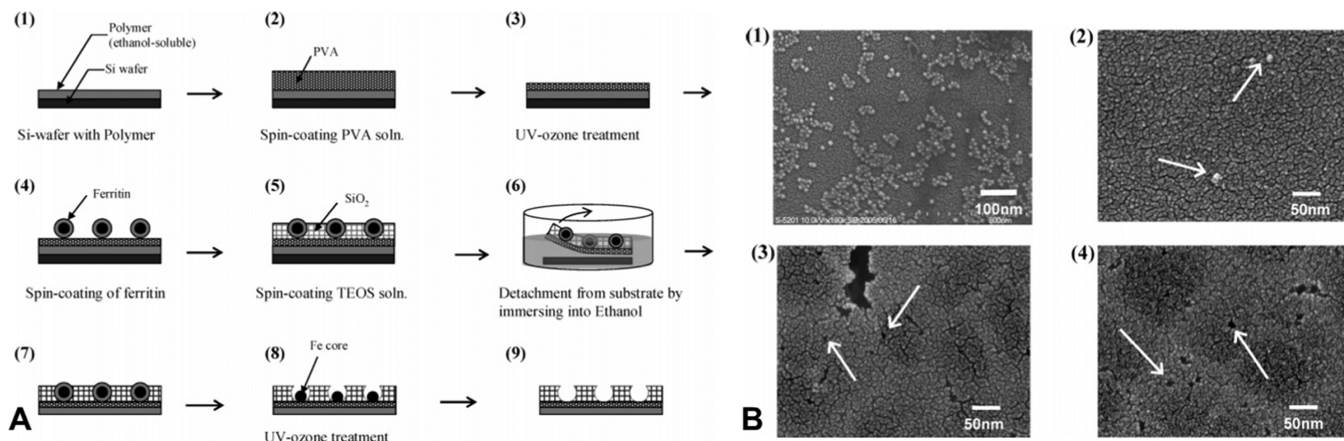


Figure 22. Embedding of individual ferritin molecules in large, self supporting silica nanofilms. (A) Preparative procedure of a ferritin/silica composite film and its chemical treatments. A polymer layer is first placed onto the substrate for proper ferritin adhesion and film removal followed by deposition of silicon oxide formation via the sol–gel process using TEOS. Ferritin can be removed via UV-ozone treatment, which leaves behind the iron core that is washed away. An inorganic porous film is the result. (B) Analysis of the individual steps in ferritin template porous film formation. SEM images of ferritin and the corresponding pore: (1) ferritin coated on a PVA-coated Si wafer, (2) after silica coating on (1), (3) after UV-ozone treatment of (2), and (4) after treatment with 1 N hydrochloric acid. Reprinted with permission from ref 362. Copyright 2007 American Chemical Society.

followed a linear relationship. Because the masking iron core is also gradually etched, a time limit of 40 min was estimated, and high aspect ratio nanocolumns with a height of about 170 nm could ultimately be fabricated.³⁵² In a following detailed study, the authors confirmed that a low (<10%) content of SiF_6 in a mixture with chlorine is advantageous to increase the etching rate, but larger SiF_6 content results in undercutting or a larger taper profile. The taper angle and etching selectivity depended further on the energy of the neutral beam, which could be adjusted by applying an rf bias power to the bottom electrode. With optimized settings, highest etching selectivity was about 500, and taper angles of up to 86° could be achieved.³⁵³ Cross-sectional high-resolution TEM showed that the sidewalls of the nanocolumn were atomically flat and the silicon lattice did not suffer any crystalline defects. The density of dangling bonds can be calculated from ESR spectra, and the defect density did not change upon neutral beam etching.³⁵²

If a $\text{Si}_{\text{substrate}}\text{-}\text{SiO}_x\text{ substrate}\text{-}\text{Si}_{\text{polycrystalline}}\text{-}\text{SiO}_x\text{ surface}\text{-ferritin}$ layer structure was thermally treated and etched, silicon nanodisks of sub-10 nm with a thickness of 1.2 nm were produced, while the whole sample surface was covered with a thermal oxide of 2 nm due to the thermal treatment.^{354,355} Considering that the first surface-oxide layer has to be quickly penetrated, the underlying poly-Si-layer must be completely etched, and the thermal oxide of the substrate must be preserved, a two-step etching procedure was employed. The surface oxide layer was thus removed by dry etching with a mixture of NF_3/H_2 gas, followed by fabrication of the disks by neutral beam etching. The etching progress can be monitored by analyzing the surface composition with XPS. This ensured that the diameter of the disks closely resembles the dimension of the masking iron oxide nanoparticles. A detailed investigation with SEM and STEM-EELS proved that the hemispherical nanodisks (diameter at the basement was approximately 16 nm, the diameter of the poly-Si disk approximately 7 nm) had a layered structure.³⁵⁵ Serial stacked nanodisks were produced if the respective multilayered substrates were etched.³⁵⁶ The prepared disks have electron/hole charging ability as measured with Kelvin probe microscopy. The corresponding $I\text{-}V$ curves of the $\text{Si}_{\text{substrate}}\text{-}\text{SiO}_x\text{-Si}_{\text{disk}}\text{-SiO}_x$ assembly showed steps (Coulomb staircase

effect) with a width of 0.2–0.3 V in good agreement with calculations for a single-electron charging effect. The underlying oxide and surface oxide worked as two tunnel junctions. The staircase width was nearly independent of the nanodisk diameter but decreased with increasing nanodisk thickness because the thickness was much smaller (1.5–4 nm) than twice the Bohr radius but the diameter (8–10.5 nm) was not. The Coulomb staircase effect could even be observed at room temperature; that is, the structure attained single-electron properties even at room temperature.^{355,357} Such structures work as quantum wells and are promising building blocks for nanoelectronic devices, such as single electron transistors. The formation of regular arrays of nanodisks requires the controlled assembly of ferritin particles. Treatment of the top Si layer by neutral beam oxidation instead of thermal oxidation produced dangling bonds, which were stable above 200 °C and responsible for the formation of regular hexagonal arrays of ferritin at the surface.³⁵⁸

The ferritin bionanoparticles can also be used for negative masks. For this, the assembled and stripped iron oxide cores from ferritin were embedded in a 2 nm thin amorphous silicon film.³⁵⁹ After removal of the iron oxide cores with hydrochloric acid, ultrafine holes are generated. In the next step, Si^+ ions were implanted into the SiO_x surface through the thin amorphous Si mask, which blocked the low energy ion beam. Yet, a high dose was maintained, and after annealing with a Nd:YAG laser, a dense assembly of silicon nanocrystals was obtained, which featured the original ferritin assembly. The uniform sizes of the crystal with 3.2 ± 0.4 nm resulted in a photoluminescence spectrum with a peak at 590 nm and a fwhm of 78 nm, clearly blue-shifted and slightly narrower than nanocrystals that were prepared without the ferritin mask. $\text{Ge}_{1-x}\text{C}_x$ nanocrystal assemblies were fabricated by this technique as well.³⁶⁰ For this, the Si nanomask was exposed to a Ge molecular beam flux and a pulsed C flux from an arc-plasma gun. Nanocrystals with C-contents of up to 3.2% were obtained, and a broad photoluminescence peak at 1.3 μm was observed.

Nakama et al. deposited iron(III) oxide containing ferritin on an APTES-modified Si(100) substrate for fabrication of small-

size and high-density $\beta\text{-FeSi}_2$ nanocrystal assemblies.³⁶¹ A dense array of Fe_2O_3 -nanoparticles was produced after electrostatic adsorption of ferritin and removal of the protein shell by thermal annealing. After reduction of the cores by NH_3 plasma, the 4.9 nm diameter Fe nanodots were embedded in an $\alpha\text{-Si}$ film within the CVD reactor to avoid reoxidation and clustering of the FeSi-alloy. After heat treatment at temperatures of 500–800 °C, a signal at 29.2° in XRD proved the formation of $\beta\text{-FeSi}_2$ (202). In addition to other signals, the minimum exciton peak was found in corresponding photoluminescence spectra. $\beta\text{-FeSi}_2$ films are promising photonic materials for silicon-based light-emitting devices. The proposed results will be improved by using smaller nanodots, for example, formed in the cavity of Dps of *Listeria innocua*, and the formation of regular assemblies.

Closely related to the fabrication of arrays for lithographic masks are the preparations of thin nanoporous membranes. For filtration purposes or sustained drug delivery, well-defined pores with uniform size distribution are advantageous. The monodisperse bionanoparticles represent ideal templates for such pores as they can be removed under a variety of conditions. Although biomolecules have been imprinted on various membranes for recognition purposes, trans-membrane functionality was not yet achieved with solid-supported membrane systems. This holds also true for the work of Fujikawa et al., who employed ferritin in a very thin matrix of silica, supported on a poly(vinyl alcohol) matrix (Figure 22).³⁶² For this, ferritin was first spin-coated on a thin (PVA) film on a silicon wafer and then embedded in a thin silica film by a second spin-coating process employing prehydrolyzed TEOS solutions. The silica film thickness was 15 ± 5 nm and thus very similar to the ferritin diameter. Although the investigation of the surface morphology with SEM and the films with TEM indicated the formation of pores after UV/ozone treatment and dissolution of the iron core with hydrochloric acid, a strong evidence of trans-membrane function was not given. Nevertheless, the results show that this was a promising approach. Of special interest can also be trans-membrane electrical functionality, mediated by the ferritin protein and the iron or other inorganic core, concomitant with catalytic activity.

6.3. Applications in Medicine and Diagnostics

The fully biocompatible and multivalent protein surface provides useful functionalities to conjugate specific ligands, such as antibodies, and offers thus interesting therapeutic and analytical applications in biomedicine. An important aspect is the biological uptake and degradation route; thus drugs, “disguised” as ferritin, would be released at specific sites and, most probably, with defined release rate.

The advantageous combination of virtually any kind of inorganic or organic compound within the apoferritin capsid and the multifunctional protein shell has already been pointed out several times. Different materials for diagnostic or therapeutic purposes can be encapsulated. The protein shell can be genetically engineered or post-translational modified by means of chemical synthesis to render a polyvalent affinity label to specifically addressed targets.

Therefore, ferritin particles have several advantages for production of diagnostic and therapeutic labels.^{138,139} First, they can be obtained in high yields in simple bacterial cultivation from generic and inexpensive raw materials. Production is fast, can be scaled up, and relies on standard biotechnology techniques. Simple and established genetic

engineering protocols allow for specifically changing the protein. Especially, it was shown that the C-terminus, including the E helix part, can be changed without altering the capability of monomer folding or 24mer-assembly.³⁶³ The N-terminus is located at the outside of the protein shell, and modification does not hamper the subunit assembly either.¹³⁹ The size uniformity of the apoferritin particles and the homogeneous conformational orientation of target-binding probes on the protein surface are critical to excellent detection sensitivity in bioassays. Assay sensitivity is further strongly enhanced by the multivalent display of epitopes and the high binding capabilities. Thus, attomolar detection sensitivity could be achieved as shown for autoantibodies of Type I diabetes in clinical patients’ sera.³⁶⁴ The comparatively small ferritin particles present less steric hindrance than other polyvalent drug carriers for therapeutic in vivo applications. The protein shell keeps the inorganic cores or ions and other encapsulated substances stable, fully water-soluble, and biocompatible. The precisely defined and identical particles of each preparation are of high importance for the preparation of pharmaceutical or analytical purposes. The encapsulation of different ions within the chemically identical shell or the assembly of the bionanoparticle shell from differently modified subunits allow the preparation of encoded labels for multiplexed assays.^{135,136,364}

6.3.1. Ferritin as Drug Delivery System. Protein-based drug delivery systems are desirable because of their biocompatibility and biodegradability and offer advantages over liposome based or direct administering of the drugs.³⁶⁵ The nontoxicity, stability, and the important biological functions of ferritin make it a very useful and versatile drug delivery system.

Various materials with therapeutic or diagnostic functions have been encapsulated. For example, apoferritin was incubated with soluble uranyl acetate at a pH around 4.5 or lower. After addition of phosphate buffer, insoluble uranium compounds precipitated inside ferritin. The uranium-235 loaded apoferritin protein surface then was functionalized with Fab-fragments for targeted binding to cells.¹⁴⁹ The sequestered uranium ions have several advantages over conventional boron-10 complexes used in clinical neutron capture therapy: Uranium-235 was efficiently precipitated inside apoferritin with only minimal loss after several days. A smaller number of uranium atoms are required because of the higher effectiveness of U-235 compared to B-10. This reduced the estimated number of the metal ions per antibody binding site on a tumor cell to approximately 320. That amount of uranium could fit adequately in the apoferritin cavity. The encapsulated heavy metal compound is efficiently shielded, and only limited immune response and toxicity is expected, if at all. Conjugation of Fab' antibody fragments yielded immune-reactive particles for targeting specific binding-sites. The functional surface allows binding to specific epitopes, which could minimize unwanted distribution to healthy and vital organs and nontumor cells.

The precipitation approach was also used by Lin and co-workers to produce ferritin encapsulated radionuclide nanoparticles.^{175,193} Traditionally, chelators were used for delivery of radionuclides for imaging and therapy of cancer (radioimmunodetection and -therapy). However, problems arise from the weak specificity of small molecular chelators and competition with other elements and leaching to set free the noncomplexed metal ions. Many ligands are complex molecules, the synthesis of which is difficult but exhibits

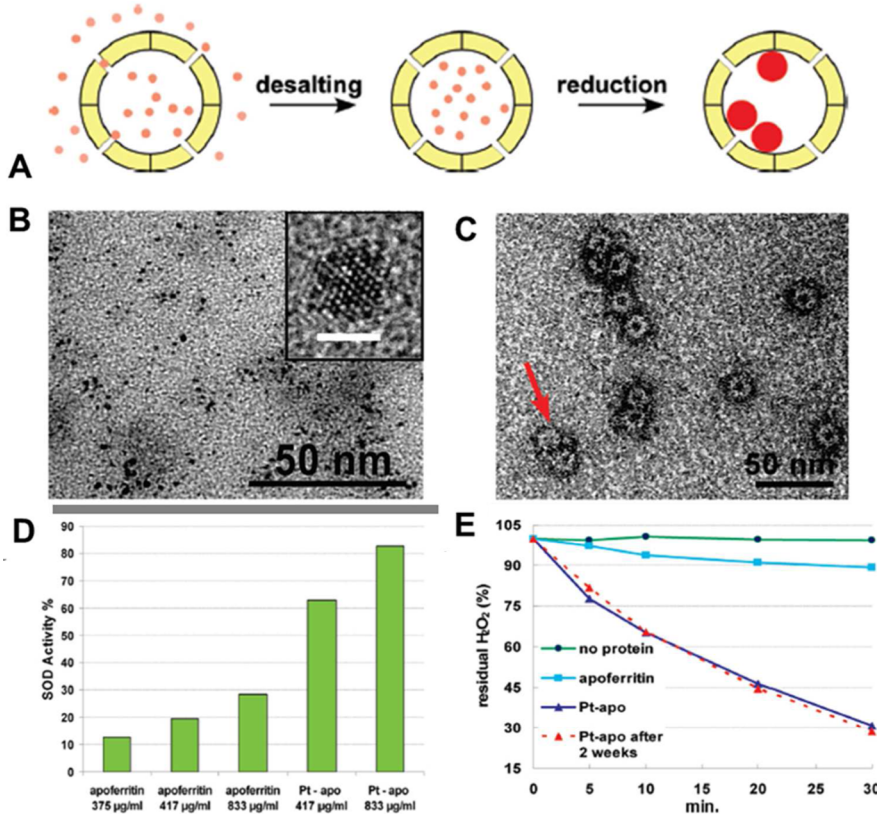


Figure 23. (A) Preparation of apo ferritin-encapsulated platinum nanoparticles (Pt-apo). (B) TEM image of Pt-apo prepared from K_2PtCl_4 /apo ferritin with a molar ratio of 24 000:1. The concentration of K_2PtCl_4 in the mixture was 312 mM. (Inset: High-resolution electron micrograph of a platinum nanoparticle; scale bar, 2 nm.) (C) TEM image of Pt-apo after negative staining with 1.5% uranyl acetate. The red arrow points toward an apo ferritin without or with very small Pt-nps in the cavity. (D) SOD activity of apo ferritin and Pt-apo prepared with a molar ratio of 15 000:1. The end concentration of K_2PtCl_4 was 250 mM. The concentration of Pt-apo is given by the protein concentration of the composite. (E) Activities of apo ferritin and Pt-apo for the H_2O_2 -decomposition and activity change of Pt-apo after 2 weeks storage in water at 4 °C. The temperature was 30 °C and pH was 7.4. Reprinted with permission from ref 165. Copyright 2010 American Chemical Society.

often poor biocompatibility and specificity. Lin and co-workers used the apo ferritin cavity as a fully biocompatible and stable enclosure for insoluble yttrium and lutetium phosphate.^{175,193} After 1 h of incubation with the nuclide, a plateau with a loading of approximately 500 yttrium or lutetium ions was achieved, which were precipitated by addition of phosphate buffer. Excess ions precipitated in solution and were removed by simple centrifugation. Biotin-modified apo ferritin, which was loaded with yttrium phosphate or lutetium phosphate, was shown to conjugate with fluorescein-streptavidin and to immobilize on avidin-modified magnetic beads. The simple and fast preparation and purification allows the use of radioisotopes with short lifetimes, which are advantageous for a gentle and well-controlled therapeutic strategy. Plain ferritin itself can be used for directed cell targeting because it plays an essential role in living biological systems.

The disassembly reassembly route has been proven particularly useful to entrap various inorganic salts, nanoparticles, or organic compounds as was described above (see section 3.1). Photosensitizer dyes were entrapped inside ferritin for photodynamic therapy¹²⁶ or platinum anticancer drugs to improve cellular uptake of the compounds and to reduce their systemic toxicity.^{129,181} PbS nanodots inside ferritin exhibited less cytotoxic effects and showed a differential effect on healthy fibroblast cells as compared to two cancer cell lines. The increased cytotoxic effect on carcinoma cells was explained with

their higher oxidative stress and metabolic activity; thus, PbS, which is disturbing these processes, had a more pronounced effect on them than on healthy cells.²⁰⁰ Another explanation could be the increased uptake of ferritin by cancer cells. Furthermore, such particles can be used for *in vivo* and deep tissue imaging because the biological matrix will not interfere with the analytical spectral part. Depending on the PbS quantum dot size, photoluminescence between 1000 and 1300 nm can be observed.^{184,200} Ferritin encapsulated platinum particles have quenching activities against H_2O_2 and superoxide ions. Having ensured that Pt-ferritin had no significant cytotoxicity on the Caco-2 cells in the applied conditions, Knez and co-workers showed that the average level of reactive oxygen species in cells treated with Pt-ferritin was lower than in cells without nanoparticles, which were challenged with oxidative stress through H_2O_2 treatment (Figure 23).¹⁶⁵ The viability of the cells was concomitantly higher. Apart from protection against oxidative species, Pt-ferritin but also apo ferritin had protective effects against other stresses as well. Although the encapsulation of the platinum nanoparticle inside ferritin and receptor-mediated internalization reduced toxicity, the location and effects of the metabolism of Pt-ferritin need still to be explored and evaluated.

The increased iron metabolism of cancer cells suggests using ferritin receptor mediated mechanisms to transfer drugs to certain cells. Jain et al. conjugated ferritin to the surface of solid

lipid nanoparticles (SLN) bearing 5-fluorouracil as a drug.³⁶⁶ The in vitro release profile of the drug from ferritin-conjugated SLNs was similar to that of bare SLNs, but the rate was slower. The uptake by the MDA-MB-468-breast cancer cell line was increased 7.4 times with concomitant increased cytotoxicity. Similarly, in vivo studies with mice showed a lower drug serum level and a higher loading in the tumors with ferritin-labeled SLNs than with the free drug or uncoupled SLNs. The tumors were markedly better inhibited with ferritin-modified SLNs.

A few studies revealed that patients suffering from various cancers exhibited higher total ferritin serum levels with a shift to H-rich ferritin, and also a marked increase of this was found in tumor tissue versus normal tissues. Thus, not only ferritin can be used to target cancer cells and tumor tissues but also ferritin-targeting antibodies. The monoclonal AMB8LK ferritin-targeting antibody was successfully used to address A-549 cells (human lung carcinoma).³⁶⁷ AMB8LK-conjugated PEG-PLA-based nanoparticles were localized in the cytosol, and paclitaxel palmitate loaded conjugates had a more pronounced effect on cell viability than the free drug or unconjugated drug-loaded nanoparticles. Surface plasmon resonance was used to assay the binding affinities in vitro, showing, for example, the discrimination between ferritin and transferrin.

6.3.2. Ferritin Nanoparticles for Biomedical Diagnostics. The construction of extremely sensitive assays based on the multivalent properties of genetic engineered apoferritin particles was shown by Lee et al.³⁶⁴ A plasmid expression vector was constructed that encoded the human ferritin heavy chain subunits with an epitope at the C-terminus that binds the 65 kDa glutamate decarboxylase specific antibody, an early marker of Type I diabetes. After expression of the fusion protein and self-assembly in *E. coli*, well-defined, intact protein cages were obtained. The authors suggested that the E-helix was in “flop” conformation, that is, with the E-helix and the antigenic epitopes being extruded outside. The assay was performed with a quantum dot and PCR-based detection. In the first case, the analytic antibodies that were bound to the epitopes of the ferritin supramolecular assemblies were further reacted with CdSe quantum dot-secondary antibody with which luminescence could be conveniently observed using a plate reader. In the PCR-based detection, the captured autoantibodies bound further epitope-containing ferritin particles, which carried additionally polylysine tags. These tags captured a type of single-stranded DNA primers, which were required for PCR-amplification of the gene in combination with the second primer strand. Both methods were able to detect antibody concentrations with sensitivity limits as low as 3 amol. The results were reproducible with another type of antibody, for example, monoclonal antibodies against hepatitis B surface antigen. The use of the same immobilized amount of nonsupramolecular antigen probes resulted in an increase in detection sensitivity of six orders of magnitude, impressively pointing out the influence of the homogeneous conformational orientation of the target-binding probes for highest assay sensitivities. Additionally, assay sensitivity is strongly enhanced by the multivalent display of epitopes. The simultaneous detection of both epitopes, the diabetes and hepatitis marker, with a mixture of the respective ferritin labels suggests that multiplexed detection techniques might be feasible.³⁶⁴ Multi-functional ferritin particles, by assembly of different engineered subunits, have not yet been produced and tested, but successful application is certainly not beyond imagination. However, the

power of the newly developed labels was further shown in assays employing sera from Type I diabetes patients.

Ferritin particles as labels for biotin-streptavidin or other antibody–antigen affinity assays based on time-resolved fluorescence were prepared by inclusion of europium(III) in apoferritin (see section 3.1).^{137–139} The apoferritin protein shell binds further defined amounts of nonferrous ions, such as Cd²⁺, Mn²⁺, or Tb³⁺, the latter particularly strong.³⁶⁸ The metal binding capability was exploited for luminescent biosensing of poly(arginine) tagged proteins. Upon incubation of intact apoferritin with Tb³⁺ ions, green luminescence is observed. Further, upon mixing with poly(arginine) or poly(arginine)-tagged proteins, a precipitate is formed selectively and luminescence is reduced.³⁶⁹ The precipitation is chain length and concentration dependent: Longer poly(arginines) (>10 arginines) and higher concentrations (>1 poly(arginine)/apoferritin subunit) yield near quantitative precipitation. The Tb³⁺-apoferritin complex is thus a suitable detection and separation tool for poly(arginine) and poly(arginine)-tagged proteins. Fluorescent and redox markers were produced by encapsulation of fluorescein or hexacyanoferrat in antibody modified ferritin and worked as sensitive labels for protein assays.^{132,133} An interesting approach to multiplexed assays with encoded ferritin particles containing metal phosphate cores was presented by Liu et al. (section 3.1).^{135,136} Shapiro et al. constructed a totally protein based MRI sensor for protein kinase activity by engineering modifying ferritin light chains and obtained, in optimized conditions, a change of 10% in the MRI signal.³⁷⁰ Contrast agents based on gadolinium(III) ions or complexes using apoferritin as a container for contrast imaging agents for the use in magnetic resonance imaging were developed as well and are described in more detail in section 6.3.4.^{127,170}

The electron dense core and the functional protein coat make ferritin an ideal contrast agent for immune-staining for electron microscopy.³⁷¹ For example, a univalent conjugate of ferritin with epidermal growth factor was used to follow time-resolved binding and internalization of cell-surface bound EGF and the transport to lysosomes.³⁷² After an initial even distribution of the ferritin-conjugated hormone on the plasma membrane with minor clustering, clustering was observed upon heating the cells from 4 to 37 °C, and internalization of 74% of the initially plasma membrane bound ferritin as endocytic vesicles or multivesicular bodies occurred within 15–30 min. Ferritin proved useful to follow physiological processes also on molecular levels. Ferritin was conjugated to the packaging RNA of the phage phi29 DNA-packaging motor and found to bind to phi29 procapsids.³⁷³ TEM investigations revealed that the ferritin-pRNA conjugates were attached to the unique vertex at the capsid where the site of the DNA translocation was supposed. However, DNA-packaging efficiency was only recovered to the level of unlabeled pRNA after release of the ferritin label.

6.3.3. Basic Magnetic Properties of Magnetic Ferritin Particles. Nature is able to synthesize magnetic nanoparticles, for example, as part of the orientation organ of magnetotactic bacteria. Biological templates obviously allow control over the crystal structure and the formation of distinct phases of inorganic materials, properties that are critical to the magnetic properties of particles. Thus, biomimetic synthesis was considered as a powerful method, and various templates, particularly ferritin, were successfully used.³⁷⁴ Advantageously, the apoferritin cage around the magnetic core particles keeps

them apart and noninteracting.³⁷⁵ Synthesis conditions of the magnetic core as well as purification of magnetoferitin samples will obviously have a strong influence on the magnetic data. Thus, magnetic parameters need always a clear description of the conditions and a physico-chemical characterization of the material as well.

Ferrihydrite is an antiferromagnetic material. The compositional deviations in the core of natural ferritin preparations may lead to differences in the observed magnetic properties. Frequently, the zero-field-cooled (ZFC) magnetic susceptibility peaks at around the blocking temperature T_b of around 12 K (depending on particle size) and superimposes with the field-cooled curve above 20–30 K.^{376–378} Because of the small size of the core, it shows superparamagnetic behavior at high temperatures. A hysteresis loop of the magnetization at low temperatures with a coercive field of around 2200–2400 G can usually be observed. In single-domain particles below some certain size, thermal energy can be enough to reverse the magnetization, and in the absence of any anisotropy the magnetization curve can be described by the classical theory of paramagnetism where M_s is the saturation magnetization and L is the Langevin function of the uncompensated magnetic moment of the particle, μ :

$$M(H, T) = M_s \cdot L(\mu H/kT)$$

A value for μ of $\sim 300 \mu_B$ is usually reported and ascribed to uncompensated spin locations in either the surface or the core sites.^{376,379} By linear extrapolation of the magnetization, an ordering temperature (Néel temperature) of around 460 K can be determined, and μ varies only little with temperature. Ferritin follows the Néel–Arrhenius behavior with a relaxation time of $\sim 10^{-11}$ s and an anisotropy energy (flip barrier) of $E_a/k_B = 318 \text{ K}$.³⁷⁹ Magnetization curves show a remarkable hysteresis, which is shifted in field cooled measurements for an exchange field of which size and position at crossing zero depend on the (maximum) field applied during field cooling.³⁸⁰ Both the exchange field and the coercive force are decreasing rapidly until 10 K and vanish at around 20 K.^{116,376,381}

The magnetization of ferritin particles cannot satisfactorily be described by a simple Langevin function, and several models have been put forward. There is still a controversy about the nature of the particles and whether they consist of multiple phases, different single phase cores, or a single phase in all protein cages (see above). Obviously, this controversy translates into difficulties to describe adequately the magnetic behavior of ferritin. Several models have been suggested.^{376,379}

Lee and co-workers presented a three-phase model by linearly adding the magnetization of the three different phases: ferrihydrite, hematite, and maghemite/magnetite. This model fit the data better than the previous models.^{382,383} The phase distribution with 60–80% ferrihydrite, 15–25% maghemite/magnetite, and 1–10% hematite corresponds reasonably well to other compositional studies. A more appropriate description can be obtained if the particle's magnetic moment μ is described by a distribution function including the influence of surface disorder, frustration, and spin canting instead of a simple volume distribution.³⁸⁴ The analysis of statistical distributions of the magnetic anisotropy energy revealed that canted surface spins contribute significantly to the observed magnetic moment in ferritin.^{384–386} The temperature and field dependence was investigated in detail (see ref 387). The linear and nonlinear magneto-optics of ferritin was investigated by

Pankowska and Dobek, and the effects were interpreted as a result of superparamagnetic and diamagnetic contributions.³⁸⁸

The T_2 relaxivity of native ferritin is $1\text{--}10 \text{ mM}^{-1} \text{ s}^{-1}$, and concentrations of some tens of micromolar would be necessary to achieve a useful contrast in magnetic resonance applications. Thus, soon after the first reports on the core reconstruction with non-native materials, the synthesis of magnetic ferritin (magnetoferitin) was reported (see above) and considered as an important step toward biomedical applications.^{150,378,389} Synthesis of magnetic iron oxide cores starts with incremental addition of iron(II) under anaerobic conditions to apoferritin with intermittent addition of oxygen as oxidant. Bulte et al. obtained monocrystalline cores of magnetite or maghemite with an average diameter 7.3 nm. They exhibited an R_1 of $8 \text{ mM}^{-1} \text{ s}^{-1}$ and an R_2/R_1 ratio of 22 (37 °C, 1.5 T).^{150,389,390} Wong et al. synthesized magnetoferitin with Fe(II) and trimethylamine-*N*-oxide as oxidant.¹⁴¹ Martínez-Pérez et al. studied the size-dependent properties of magnetoferitin prepared by this route in detail.³⁹¹ A consistent set of ferritin samples with iron loadings from 240 to 3000 Fe was characterized. With increasing filling, the particles showed better crystallinity with Bragg reflections of magnetite or maghemite. Core size distribution widened with increasing loading, and core shape was changing from irregularly shaped to complete filling and agglomeration at maximum loading, indicative for merging of crystalline domains forming the final nanoparticle core. This leads to the observed small net magnetic moment as the magnetization vectors of each crystalline domain are pinned and magnetic interactions between the domains are frustrated by the strongly anisotropic surface spins. The superparamagnetic blocking temperature was decreasing from around 22 to 7 K with the core size decreasing from around 5 to 1.8 nm. The magnetically induced optical birefringence of magnetoferitin, prepared by the method of Wong et al., was investigated by Koralewski and co-workers and compared to ferritin and nanosized magnetite. The experimental data of magnetoferitin could not be properly described by the usual Langevin formalism.³⁹² Uchida et al. used a protocol with ammonium iron sulfate and hydrogen peroxide as oxidant under anaerobic conditions for the formation of maghemite/magnetite cores with tunable sizes. The particles with iron loadings of 1000–5000 Fe per cage had relaxivities of $11\text{--}93 (\text{mM s})^{-1}$ (R_2) and $2.3\text{--}8.4 (\text{mM s})^{-1}$ (R_1) and were phagocytosed in similar amounts (as per ferritin cage) by macrophages as other iron oxide-based contrast agents.¹⁵³ Cao et al. investigated such prepared and purified ferromagnetic human H chain ferritin with a mean core diameter of $3.9 \pm 1.1 \text{ nm}$.³⁷⁵ The Wohlfarth–Cisowski test and Henkel plot indicated no magnetostatic interactions. Low-field magnetization showed that the susceptibility peaked at 9.2 K and the field and zero-field cooling curves merge at 50 K. At higher temperatures, the material obeys the Curie–Weiss law. All of the single domain particles were unblocked at 15 K (superparamagnetic state). Correspondingly, the hysteresis loops measured at $\pm 3 \text{ T}$ become smaller, and coercivity as well as remanence coercivity decrease approaching 15 K and vanish above that temperature. A Néel–Arrhenius plot was extracted from frequency-dependent measurements of the in-phase susceptibility χ' at various temperatures. At temperatures above 50 K, the curves superpose perfectly. The magnetic anisotropy energy constant $K_{\text{eff}} = 1.2 \times 10^5 \text{ J/m}^3$ is much larger than that of bulk magnetite, which can be explained with the surface uniaxial anisotropy. Synthesis under near anaerobic

conditions and magnetic separation yielded magnetoferitin particles with improved R_2 values of $78 \text{ mM}^{-1} \text{ s}^{-1}$ and R_2/R_1 ratio of 1114 (per particle).³⁹³ Such prepared particles showed at concentrations as low as 30 nM a T_2 phase contrast in rats, while natural ferritin did not. Magnetoferitin that was decorated with photocleavable dendrons showed switchable self-assembly properties and concomitantly changed magnetic properties.³⁹⁴

Mixed-metal iron oxide (Co/Fe) particles were synthesized in ferritin to gain control over the exchange coupling at the interface of ferromagnetic and antiferromagnetic materials and obtain magnetic order at higher temperatures.³⁹⁵ A mixed phase $\text{Co}_x\text{Fe}_{3-x}\text{O}_4$ formed, competing with the formation of Co_3O_4 at high doping levels. Correspondingly, the T_B increased to 126 K at 10% Co in Fe_3O_4 but decreased at higher concentrations because of the formation of antiferromagnetic cobalt oxide, which biases the ferromagnetic iron oxide core. The exchange bias was highest for “slowly” synthesized mixed oxides because more Co_3O_4 was formed. Any bias disappeared near the Néel temperature of cobalt oxide at 30 K. Mn-doping led to nonferromagnetic cores as the Fe local environment changes from the $\gamma\text{-Fe}_2\text{O}_3$ defected spinel structure to a Fe_3O_4 spinel structure beyond Mn concentrations of 10%.¹⁵² Magnetic Co/Pt nanoparticulate films were prepared by annealing ferritin films and showed widely varying shapes and coercivities in the hysteresis loops.³⁹⁶

Other than iron oxide, magnetic cores were prepared, for example, Gd-loaded apoferitin particles. Characterization of the magnetic properties revealed that the particles were fully paramagnetic with a longitudinal relaxivity of 10–25 times higher and a transverse relaxivity of about 70 times higher than commercial Gd-based agents for magnetic resonance imaging. The long-term stability and low leaching rate constitute another advantage of the Gd(III)–ferritin system as MRI contrast agent over the classical low molecular, mononuclear gadolinium(III) complexes.¹⁷⁰ Of all possible mechanisms for the enhancement of the nuclear relaxation rates, the free exchange of water molecules with the cage interior might be the most responsible one. Aime and co-workers showed that Mn(II)-loaded apoferitin can be prepared as a highly sensitive magnetic resonance imaging agent.¹⁴⁸ They reduced MnOOH cores with aminopolycarbocyclic ligands like nitrilotriacetic acid or 1,4,8,11-tetraazacyclotetradecane-1,4,8,11-tetraacetic acid (TETA) with a final Mn(II) content tunable by the extent of the reductive treatment. Up to 1090 ± 90 Mn(II, III) were entrapped in the protein cavity after treatment with TETA, and an average relaxivity of $4000\text{--}7000 \text{ mM}^{-1} \text{ s}^{-1}$ per apoferitin particle was thus achieved. The stable sequestration of the toxic Mn(II) aqua ion was verified by the NMR dispersion and the characteristic six-line pattern of the EPR spectrum.

Interesting magnetic properties were observed for Pd nanoparticles in apoferitin as well.¹⁵⁵ The reconstitution was done with K_2PdCl_4 and NaBH_4 . The XRD pattern of the 2.4 ± 1 nm small particles corresponded to fcc Pd reflection. The sample showed marked hysteresis loops in the magnetization curves up to 300 K. Magnetization is lower and tends to saturate at higher temperatures, which indicates the existence of blocked ferromagnetic entities dominating the high temperature behavior. The blocking temperature was determined to be at around 350 K. The DC magnetic susceptibility, however, increases upon cooling, evidencing the presence of superparamagnetic and paramagnetic contributions, dominating at low temperatures. The authors postulated the presence of a

thin, although not yet detected, oxide shell on the Pd nanoparticles, which leads to the changes in the Fermi level occupation with the resulting observed magnetic phenomena.¹⁵⁵

6.3.4. Magnetic Ferritin Nanoparticles, Attractive for MRI Applications. Magnetic resonance imaging (MRI) has great promise in the development of high-resolution diagnostic clinical imaging techniques as the basic technique is already well-introduced and can be applied repeatedly as it does not use ionizing radiation. Imaging at resolutions in the submillimeter range will improve even further with the introduction of higher magnetic fields with 3 T and more. Comparatively low sensitivity has been considered as a major obstacle of the technique, thus requiring larger amounts of contrast agents.

Basically, MRI records the relaxation process of protons after they have been perturbed by a radio frequency pulse from their aligned state in an external field. Longitudinal and transversal relaxation processes can be used to generate the MRI image. The varying water concentrations and local environments produce the contrast in biological specimens. MRI imaging agents can also be separated into two classes, paramagnetic molecular complexes derived from, for example, Gd(III), or superparamagnetic iron oxide nanoparticles, for example, Fe_3O_4 . The former type appears bright in T_1 -weighted images because it induces an increase in signal intensity, while the latter type appears dark in T_2 -weighted images because it produces a decrease in signal intensity. The concentration of MRI agents is directly related to the enhancement or reduction of the respective relaxation rates of the water protons. The development of nanoscale high-sensitivity contrast agents had a great impact on the development of MR for molecular imaging and clinical diagnosis.^{397–399} High performance MRI contrast agents have favorable cellular uptake properties and biodistribution, tunable magnetic properties, and conjugation possibilities. Particularly, ferritin has been developed toward a probeless MRI reporter, for example, to monitor gene therapy.^{398,400} Following their (co)expression, they sequester endogenous iron and provide MRI contrast from T_2 -weighted images.⁴⁰¹ Using specific vectors enables the targeted delivery of ferritin to specific tissues. For example, ferritin was cloned into two rabies virus vectors, which can pass the blood–brain barrier and were shown to be expressed in transfected BHK-21 cells.⁴⁰² Ferritin as endogenous iron storage protein has the significant advantage of well-defined dimensions, no toxicity, and a well-known biodistribution and excretion profile. Beeman et al. studied the accumulation of cationized ferritin by intravenous injection, and the particles were found neither nephrotoxic nor hepatotoxic in a MRI detectable dose.⁴⁰³ Further, conjugation of targeting ligands can reroute the particles to specific receptors. This means that distribution can differ within different tissues. The accumulation of ferritin in macrophages in atherosclerotic plaques can help, for example, direct *in vivo* vascular imaging.^{153,404} The slow excretion profile from dead cells might constitute a disadvantage. Another issue is the up-regulation of transferring receptor to answer the state of the transient iron deficiency due to ferritin expression and iron core formation or iron overload due to iron leaching from iron oxide particles. Thus, in systemic views, various influences have to be considered when interpreting MRI intensities. It is further noteworthy that the construction of ferritin from L and H chain chimera, driven by the rationale to use the ferroxidase activity of the H-chain to promote higher iron storage while driving self-assembly and stabilizing the shell through the L

chain interactions, had a significant influence on iron uptake and the resulting MRI image contrast.⁴⁰⁵ The engineered protein shell acquired higher iron loadings during expression in HEK293 cells and significantly higher R_2 relaxation rates than the cells that expressed only L or H subunits or the reverse construct H–L. The longitudinal relaxation rate R_1 was similar for all samples. Because of the high L-content, the ferritin particles were conveniently located in the cytoplasm with better access to iron and mobile water.

The relatively low $1/T_2$ of ferritin requires high field strengths or other ways to increase $1/T_2$, for example, via aggregation or as Qiang et al. developed a wireless amplifier nuclear MR detector (WAND) device that can be introduced into the body with minimal invasion and amplifying the MR signal in T_1 -weighted (gadopentetate dimeglumine) and T_2^* -weighted (cationized ferritin) GRE images to identify renal tubules and glomeruli structures in kidney tissues.⁴⁰⁶ In the end, Bennett et al. achieved an increase of R_2 of 70% from 9 to $16\text{ mM}^{-1}\text{ s}^{-1}$ via chemical cross-linking with 3,3'-dithiobis-(sulfosuccinimidylpropionate) or an increase of still 30% by in vitro polymerization of actin-ferritin.⁴⁰⁷ Srivastava et al. found the same effect after ex situ interparticle coupling of aggregated ferritin with magnetic FePt.²⁴⁴

Upon a systemic disease, the basement membrane can be altered, and its structure and integrity can help diagnose renal and cardiac conditions. Bennet et al. based their investigation on the electrostatic attraction between the proteoglycans present in the basement membrane and the cationic ferritin, which is obtained by the addition of amino groups in its outer surface. Results showed great selectivity of the CF with the basement membrane and a signal reduction of 60%, allowing the identification of glomeruli, which are critical structures in renal diseases.⁴⁰⁸ Actual methods for sizing and counting of glomeruli are invasive and not possible in intact organs. However, by noninvasive MR imaging and using the same interaction between CF and the basement membrane, identification and quantification of every glomerulus were possible using a segmentation algorithm in whole rat kidneys.^{409,410} Furthermore, Bennett and co-workers could also size and number glomeruli structures in intact human kidneys by intravenous injection of CF, a step further to in vivo applications.⁴¹¹

7. CONCLUSIONS AND OUTLOOK

Using protein structures in combination with synthetic as well as genetic alterations has proven to be highly interesting for the production of new materials. These materials may be applicable in electronic devices, sensors, medicine, or for biofunctionalization of surfaces.^{1,2,86,118,412} Even though for all of these applications, the most often used is probably ferritin because the behavior and structural properties have been intensely studied as well as the ease of availability of various ferritins and ferritin-like structures, it is worth mentioning the potential of other protein cage structures as DPs and also virus like particles (CCMV, CPMV, M13, M2), which possess the ability of cell permeability. Moreover, the elucidation of new protein structures leads to a wide range of genetic and synthetic modifications of those blends with inorganic nanoparticles for future applications from electronic devices to in vivo delivery systems.

Nevertheless, although many combinations between proteins and synthetic components have been achieved, finding improved synthetic procedures with respect to lower reaction

temperatures, protein stability, and scalability still is a continuing process, also with respect to increasing the variety of possible modifications. Most of these modifications address either the inside of the ferritin cage or the outside. To further advance the practical aspects and the usability, it is vital that both approaches are combined to maximize the number of materials and applications that are feasible with this versatile protein structure. Possibilities are combining antigens and semiconductor nanoparticles, for example, silver nanoparticles for cell-targeting in combination with imaging or antibacterial properties. Also, in molecular electronic devices, conjugated polymers with isolated structures in the nanometer regime would potentially benefit from this approach.

AUTHOR INFORMATION

Corresponding Author

*E-mail: boker@dwi.rwth-aachen.de.

Author Contributions

[§]These authors contributed equally.

Notes

The authors declare no competing financial interest.

Biographies



Günther Jutz studied Chemistry with Macromolecular Chemistry as a major subject at the University of Bayreuth. End of 2008, he received his Ph.D. under the supervision of Prof. Alexander Böker with a research work on mineralized bionanoparticle stabilized Pickering emulsions. His research interests reach from controlled polymerization techniques to viruses and proteins as building blocks in bionanotechnology and bio-(in)organic composite materials. After a visit in the group of Prof. José Carlos Rodriguez Cabello, University of Valladolid, Spain, he joined SGL Carbon GmbH, working now on the development of carbon and graphite materials for energy storage systems. Now he is working at Leclanché GmbH as project manager for the development of lithium ion cells.



Patrick van Rijn is currently assistant professor and head of the research group Bio-inspired Synthetic Materials Science within the department of BioMedical Engineering at the University Medical Center Groningen. He is associated to the W.J. Kolff Institute for Biomedical Engineering and Materials Science in which he coordinates the research-line “Bionanotechnology and Advanced Therapeutic Materials”. His group focuses on the development of new biointerfaces, artificial virus structures and polymeric microgels for medical applications. Previously, he was an Alexander von Humboldt-fellow for Post-doctoral research in the group of Alexander Böker at the DWI-Leibniz-Institute for Interactive Materials, Aachen, Germany. He joined this institute in 2010, directly after receiving his Ph.D. in the field of Supramolecular Chemistry with Jan H. van Esch at Delft University of Technology.



Barbara S. Miranda obtained her Bachelor degree in Chemistry at University of Brasilia, before her Master's degree in Physical Chemistry in 2009, from University of Campinas, Brazil. Her Ph.D. in Analytical Chemistry was also obtained from the same institution in 2013, but part of the research was developed at Helmholtz Zentrum München, Germany, during one year period as an exchange Ph.D. student. During her studies, she synthesized and applied nanoparticles in combination with biomolecules for the development of energy conversion and sensor devices. Currently, she is a guest postdoctoral researcher at Patrick van Rijn's group, with a Science Without Borders fellowship from INCTBio (Brazil), in the department of Biomedical Engineering at the University of Groningen, University Medical Center Groningen, the Netherlands.



Alexander Böker holds the Chair of Macromolecular Materials and Surfaces at RWTH Aachen and is Co-Director of the DWI – Leibniz-Institut für Interaktive Materialien. He studied chemistry at the Johannes Gutenberg University Mainz and received his Ph.D. from Bayreuth University in 2002, working with Prof. G. Krausch and Prof. Axel H.E. Müller. From 2002–2004 he was a postdoctoral fellow with Thomas P. Russell at the University of Massachusetts, Amherst. In 2006, he received a Lichtenberg-Professorship funded by the VolkswagenStiftung. Besides being Founding Editor-in-Chief of *Polymers*, he is Member of the Reimund Stadler Minerva Center for Mesoscale Macromolecular Engineering in Beer Sheva, Israel, Member of the International Advisory Board of *Macromolecular Chemistry & Physics* (Wiley-VCH), as well as the Editorial Board of *Colloid & Polymer Science* (Springer) and *Polymer* (Elsevier). He published more than 90 papers in peer-reviewed journals. The main research interests of his group include guided self-assembly of block copolymer systems, hierarchical (bio)nanoparticle assemblies and the control of self-assembly processes via external fields.

REFERENCES

- (1) Jutz, G.; Boeker, A. *Polymer* **2011**, *52*, 211.
- (2) van Rijn, P.; Böker, A. *J. Mater. Chem.* **2011**, *21*, 16735.
- (3) Lee, L. A.; Nguyen, H. G.; Wang, Q. *Org. Biomol. Chem.* **2011**, *9*, 6189.
- (4) Shen, L.; Bao, N.; Zhou, Z.; Prevelige, P. E.; Gupta, A. *J. Mater. Chem.* **2011**, *21*, 18868.
- (5) Cardinale, D.; Carette, N.; Michon, T. *Trends Biotechnol.* **2012**, *30*, 369.
- (6) Lee, L. A.; Niu, Z.; Wang, Q. *Nano Res.* **2009**, *2*, 349.
- (7) Behrens, S. S. *J. Mater. Chem.* **2008**, *18*, 3788.
- (8) Sano, K.; Ajima, K.; Iwahori, K.; Yudasaka, M.; Iijima, S.; Yamashita, I.; Shiba, K. *Small* **2005**, *1*, 826.
- (9) Mao, C.; Liu, A.; Cao, B. *Angew. Chem., Int. Ed.* **2009**, *48*, 6790.
- (10) Pokorski, J. K.; Steinmetz, N. F. *Mol. Pharmaceutics* **2011**, *8*, 29.
- (11) Douglas, T.; Young, M. *Nature* **1998**, *393*, 152.
- (12) Laplagne, D. A.; Zylberman, V.; Aincart, N.; Steward, M. W.; Scitto, E.; Fossati, C. A.; Goldbaum, F. A. *Proteins* **2004**, *57*, 820.
- (13) McMillan, R. A.; Paavola, C. D.; Howard, J.; Chan, S. L.; Zaluzec, N. J.; Trent, J. D. *Nat. Mater.* **2002**, *1*, 247.
- (14) Yamashita, I.; Iwahori, K.; Kumagai, S. *Biochim. Biophys. Acta* **2010**, *1800*, 846.
- (15) Kramer, R. M.; Li, C.; Carter, D. C.; Stone, M. O.; Naik, R. R. *J. Am. Chem. Soc.* **2004**, *126*, 13282.
- (16) Harrison, P. M.; Arosio, P. *Biochim. Biophys. Acta, Bioenerg.* **1996**, *1275*, 161.
- (17) Arosio, P.; Ingrassia, R.; Cavadini, P. *Biochim. Biophys. Acta, Gen. Subj.* **2009**, *1790*, 589.
- (18) Bou-Abdallah, F. *Biochim. Biophys. Acta* **2010**, *1800*, 687.
- (19) Andrews, S. C.; Robinson, A. K.; Rodriguez-Quinones, F. *FEMS Microbiol. Rev.* **2003**, *27*, 215.

- (20) Crow, A.; Lawson, T. L.; Lewin, A.; Moore, G. R.; Le Brun, N. *E. J. Am. Chem. Soc.* **2009**, *131*, 6808.
- (21) Carrondo, M. A. *EMBO J.* **2003**, *22*, 1959.
- (22) Chiancone, E.; Ceci, P. *Biochim. Biophys. Acta, Gen. Subj.* **2010**, *1800*, 798.
- (23) Haikarainen, T.; Papageorgiou, A. C. *Cell. Mol. Life Sci.* **2010**, *67*, 341.
- (24) Calhoun, L. N.; Kwon, Y. M. *J. Appl. Microbiol.* **2010**, *110*, 375.
- (25) Briat, J. F.; Duc, C.; Ravet, K.; Gaymard, F. *Biochim. Biophys. Acta, Gen. Subj.* **2010**, *1800*, 806.
- (26) Briat, J. F.; Ravet, K.; Arnaud, N.; Duc, C.; Boucherez, J.; Touraine, B.; Cellier, F.; Gaymard, F. *Ann. Bot.* **2010**, *105*, 811.
- (27) Pham, D. Q. D.; Winzerling, J. J. *Biochim. Biophys. Acta, Gen. Subj.* **2010**, *1800*, 824.
- (28) Andrews, S. C. *Biochim. Biophys. Acta, Gen. Subj.* **2010**, *1800*, 691.
- (29) Harrison, P. M.; Hempstead, P. D.; Artymiuk, P. J.; Andrews, S. C. In *Iron Transport and Storage in Microorganisms, Plants and Animals*; Sigel, A., Sigel, H., Eds.; Marcel Dekker, Inc.: New York, 1998.
- (30) Grossman, M. J.; Hinton, S. M.; Minak-Bernero, V.; Slaughter, C.; Stiefel, E. I. *Proc. Natl. Acad. Sci. U.S.A.* **1992**, *89*, 2419.
- (31) Liu, X.; Theil, E. C. *Acc. Chem. Res.* **2005**, *38*, 167.
- (32) Powell, A. K. In *Iron Transport and Storage in Microorganisms, Plants and Animals*; Sigel, A., Sigel, H., Eds.; Marcel Dekker, Inc.: New York, 1998.
- (33) Hintze, K. J.; Theil, E. C. *Cell. Mol. Life Sci.* **2006**, *63*, 591.
- (34) Alkhateeb, A. A.; Connor, J. R. *Biochim. Biophys. Acta, Gen. Subj.* **2010**, *1800*, 793.
- (35) Arosio, P.; Levi, S. *Biochim. Biophys. Acta, Gen. Subj.* **2010**, *1800*, 783.
- (36) Wang, W.; Knovich, M. A.; Coffman, L. G.; Torti, F. M.; Torti, S. V. *Biochim. Biophys. Acta, Gen. Subj.* **2010**, *1800*, 760.
- (37) Knovich, M. A.; Storey, J. A.; Coffman, L. G.; Torti, S. V.; Torti, F. M. *Blood Rev.* **2009**, *23*, 95.
- (38) Theil, E. C. *Annu. Rev. Nutr.* **2004**, *24*, 327.
- (39) Le Brun, N. E.; Crow, A.; Murphy, M. E. P.; Mauk, A. G.; Moore, G. R. *Biochim. Biophys. Acta, Gen. Subj.* **2010**, *1800*, 732.
- (40) Linder, M. C.; Kakavandi, H. R.; Miller, P.; Wirth, P. L.; Nagel, G. M. *Arch. Biochem. Biophys.* **1989**, *269*, 485.
- (41) Liu, X.; Jin, W.; Theil, E. C. *Proc. Natl. Acad. Sci. U.S.A.* **2003**, *100*, 3653.
- (42) Crichton, R. R.; Declercq, J. P. *Biochim. Biophys. Acta, Gen. Subj.* **2010**, *1800*, 706.
- (43) Hempstead, P. D.; Yewdall, S. J.; Fernie, A. R.; Lawson, D. M.; Artymiuk, P. J.; Rice, D. W.; Ford, G. C.; Harrison, P. M. *J. Mol. Biol.* **1997**, *268*, 424.
- (44) Chasteen, N. D.; Harrison, P. M. *J. Struct. Biol.* **1999**, *126*, 182.
- (45) Banyard, S. H.; Stammers, D. K.; Harrison, P. M. *Nature* **1978**, *271*, 282.
- (46) Clegg, G. A.; Stansfield, R. F. D.; Bourne, P. E.; Harrison, P. M. *Nature* **1980**, *288*, 298.
- (47) Watt, R. K.; Hilton, R. J.; Graff, D. M. *Biochim. Biophys. Acta, Gen. Subj.* **2010**, *1800*, 745.
- (48) Liu, X. F.; Theil, E. C. *Proc. Natl. Acad. Sci. U.S.A.* **2004**, *101*, 8557.
- (49) Bou-Abdallah, F. *Biochim. Biophys. Acta, Gen. Subj.* **2010**, *1800*, 719.
- (50) Theil, E. C.; Takagi, H.; Small, G. W.; He, L.; Tipton, A. R.; Danger, D. *Inorg. Chim. Acta* **2000**, *297*, 242.
- (51) Theil, E. C.; Liu, X. S.; Toshia, T. *Inorg. Chim. Acta* **2008**, *361*, 868.
- (52) Jin, W.; Takagi, H.; Pancorbo, B.; Theil, E. C. *Biochemistry* **2001**, *40*, 7525.
- (53) Galvez, N.; Ruiz, B.; Cuesta, R.; Colacio, E.; Dominguez-Vera, J. M. *Inorg. Chem.* **2005**, *44*, 2706.
- (54) Liu, X. S.; Patterson, L. D.; Miller, M. J.; Theil, E. C. *J. Biol. Chem.* **2007**, *282*, 31821.
- (55) Shi, H.; Bencze, K. Z.; Stemmler, T. L.; Philpott, C. C. *Science* **2008**, *320*, 1207.
- (56) Theil, E. C.; Matzapetakis, M.; Liu, X. F. *J. Biol. Inorg. Chem.* **2006**, *11*, 803.
- (57) Toshia, T.; Ng, H. L.; Bhattachari, O.; Alber, T.; Theil, E. C. *J. Am. Chem. Soc.* **2010**, *132*, 14562.
- (58) Turano, P.; Lalli, D.; Felli, I. C.; Theil, E. C.; Bertini, I. *Proc. Natl. Acad. Sci. U.S.A.* **2010**, *107*, 545.
- (59) Masuda, T.; Goto, F.; Yoshihara, T.; Mikami, B. *Biochem. Biophys. Res. Commun.* **2010**, *400*, 94.
- (60) Deng, Q. Y.; Yang, B.; Wang, J. F.; Whiteley, C. G.; Wang, X. N. *Biotechnol. Lett.* **2009**, *31*, 1505.
- (61) Ueno, T.; Suzuki, M.; Goto, T.; Matsumoto, T.; Nagayama, K.; Watanabe, Y. *Angew. Chem., Int. Ed.* **2004**, *43*, 2527.
- (62) Webb, B.; Frame, J.; Zhao, Z.; Lee, M. L.; Watt, G. D. *Arch. Biochem. Biophys.* **1994**, *309*, 178.
- (63) Michel, F. M.; Hosein, H. A.; Hausner, D. B.; Debnath, S.; Parise, J. B.; Strongin, D. R. *Biochim. Biophys. Acta, Gen. Subj.* **2010**, *1800*, 871.
- (64) Carta, D.; Casula, M. F.; Corrias, A.; Falqui, A.; Navarra, G.; Pinna, G. *Mater. Chem. Phys.* **2009**, *113*, 349.
- (65) Michel, F. M.; Ehm, L.; Antao, S. M.; Lee, P. L.; Chupas, P. J.; Liu, G.; Strongin, D. R.; Schoonen, M. A. A.; Phillips, B. L.; Parise, J. B. *Science* **2007**, *316*, 1726.
- (66) Galvez, N.; Fernandez, B.; Sanchez, P.; Cuesta, R.; Ceolin, M.; Clemente-Leon, M.; Trasobares, S.; Lopez-Haro, M.; Calvino, J. J.; Stephan, O.; Dominguez-Vera, J. M. *J. Am. Chem. Soc.* **2008**, *130*, 8062.
- (67) Pan, Y. H.; Sader, K.; Powell, J. J.; Bleloch, A.; Gass, M.; Trinick, J.; Warley, A.; Li, A.; Brydson, R.; Brown, A. *J. Struct. Biol.* **2009**, *166*, 22.
- (68) Sczkan, S. R.; Joshi, J. G. *Biochim. Biophys. Acta, Gen. Subj.* **1989**, *990*, 8.
- (69) Pead, S.; Durrant, E.; Webb, B.; Larsen, C.; Heaton, D.; Johnson, J.; Watt, G. D. *J. Inorg. Biochem.* **1995**, *59*, 15.
- (70) Polanams, J.; Ray, A. D.; Watt, R. K. *Inorg. Chem.* **2005**, *44*, 3203.
- (71) Sanchez, P.; Galvez, N.; Colacio, E.; Minones, E.; Dominguez-Vera, J. M. *Dalton Trans.* **2005**, *4*, 811.
- (72) Funk, F.; Lenders, J. P.; Crichton, R. R.; Schneider, W. *Eur. J. Biochem.* **1985**, *152*, 167.
- (73) Sakurai, K.; Nabeyama, A.; Fujimoto, Y. *BioMetals* **2006**, *19*, 323.
- (74) Jackson, C. S.; Kodanko, J. *J. Metallomics* **2010**, *2*, 407.
- (75) Hoy, T. G.; Harrison, P. M.; Shabbir, M.; Macara, I. G. *Biochem. J.* **1974**, *137*, 67.
- (76) Salgado, J. C.; Olivera-Nappa, A.; Gerdzen, Z. P.; Tapia, V.; Theil, E. C.; Conca, C.; Nunez, M. T. *BMC Syst. Biol.* **2010**, *4*, 147.
- (77) Flenniken, M. L.; Willits, D. A.; Brumfield, S.; Young, M. J.; Douglas, T. *Nano Lett.* **2003**, *3*, 1573.
- (78) Flenniken, M. L.; Liepold, L. O.; Crowley, B. E.; Willits, D. A.; Young, M. J.; Douglas, T. *Chem. Commun.* **2005**, *4*, 447.
- (79) Varpness, Z.; Peters, J. W.; Young, M.; Douglas, T. *Nano Lett.* **2005**, *5*, 2306.
- (80) Wiedenheft, B.; Mosolf, J.; Willits, D.; Yeager, M.; Dryden, K. A.; Young, M.; Douglas, T. *Proc. Natl. Acad. Sci. U.S.A.* **2005**, *102*, 10551.
- (81) Schonafinger, A.; Morbitzer, A.; Kress, D.; Essen, L. O.; Noll, F.; Hampp, N. *Langmuir* **2006**, *22*, 7185.
- (82) Tatur, J.; Hagedoorn, P. L.; Overeijnder, M. L.; Hagen, W. R. *Extremophiles* **2006**, *10*, 139.
- (83) Tatur, J.; Hagen, W. R.; Matias, P. M. *J. Biol. Inorg. Chem.* **2007**, *12*, 615.
- (84) Honarmand Ebrahimi, K.; Hagedoorn, P.-L.; Jongejan, J. A.; Hagen, W. R. *J. Biol. Inorg. Chem.* **2009**, *14*, 1265.
- (85) Parker, M. J.; Allen, M. A.; Ramsay, B.; Klem, M. T.; Young, M.; Douglas, T. *Chem. Mater.* **2008**, *20*, 1541.
- (86) Klem, M. T.; Young, M.; Douglas, T. *J. Mater. Chem.* **2010**, *20*, 65.
- (87) Kasyutich, O.; Ilari, A.; Fiorillo, A.; Tatchev, D.; Hoell, A.; Ceci, P. *J. Am. Chem. Soc.* **2010**, *132*, 3621.

- (88) Bozzi, M.; Mignogna, G.; Stefanini, S.; Barra, D.; Longhi, C.; Valenti, P.; Chiancone, E. *J. Biol. Chem.* **1997**, *272*, 3259.
- (89) Chiaraluce, R.; Consalvi, V.; Cavallo, S.; Ilari, A.; Stefanini, S.; Chiancone, E. *Eur. J. Biochem.* **2000**, *267*, 5733.
- (90) Ilari, A.; Stefanini, S.; Chiancone, E.; Tsernoglou, D. *Nat. Struct. Biol.* **2000**, *7*, 38.
- (91) Bellapadrona, G.; Stefanini, S.; Zamparelli, C.; Theil, E. C.; Chiancone, E. *J. Biol. Chem.* **2009**, *284*, 19101.
- (92) Yang, X. K.; Chiancone, E.; Stefanini, S.; Ilari, A.; Chasteen, N. D. *Biochem. J.* **2000**, *349*, 783.
- (93) Stefanini, S.; Cavallo, S.; Montagnini, B.; Chiancone, E. *Biochem. J.* **1999**, *338*, 71.
- (94) Kramer, R. M.; Sowards, L. A.; Pender, M. J.; Stone, M. O.; Naik, R. R. *Langmuir* **2005**, *21*, 8466.
- (95) Allen, M.; Willits, D.; Mosolf, J.; Young, M.; Douglas, T. *Adv. Mater.* **2002**, *14*, 1562.
- (96) Allen, M.; Willits, D.; Young, M.; Douglas, T. *Inorg. Chem.* **2003**, *42*, 6300.
- (97) Tam, J. P.; Lu, Y. A. *Proc. Natl. Acad. Sci. U.S.A.* **1989**, *86*, 90848.
- (98) Tam, J. P.; Profy, A. T. PCT Int. Appl.; Repligen Corp., Rockefeller University, U.S., WO, 1993.
- (99) Taylor, K. M.; Lin, T.; Porta, C.; Mosser, A. G.; Giesing, H. A.; Lomonosoff, G. P.; Johnson, J. E. *J. Mol. Recognit.* **2000**, *13*, 71.
- (100) Lomonosoff, G. P.; Johnson, J. E. *Curr. Opin. Struct. Biol.* **1996**, *6*, 176.
- (101) Danon, D.; Goldstein, L.; Marikovsky, Y.; Skutelsky, E. *J. Ultrastruct. Res.* **1972**, *38*, 500.
- (102) Perriman, A. W.; Colfen, H.; Hughes, R. W.; Barrie, C. L.; Mann, S. *Angew. Chem., Int. Ed.* **2009**, *48*, 6242.
- (103) Perriman, A. W.; Mann, S. *ACS Nano* **2011**, *5*, 6085.
- (104) Wetz, K.; Crichton, R. R. *Eur. J. Biochem.* **1976**, *61*, 545.
- (105) Takeda, S.; Yamaki, M.; Ebina, S.; Nagayama, K. *J. Biochem.* **1995**, *117*, 267.
- (106) Wong, K. K. W.; Colfen, H.; Whilton, N. T.; Douglas, T.; Mann, S. *J. Inorg. Biochem.* **1999**, *76*, 187.
- (107) Wong, K. K. W.; Whilton, N. T.; Douglas, T.; Mann, S.; Colfen, H. *Chem. Commun.* **1998**, 1621.
- (108) Sengonul, M.; Sousa, A.; Libera, M. *Colloids Surf., B* **2009**, *73*, 152.
- (109) Sengonul, M.; Ruzicka, J.; Attygalle, A. B.; Libera, M. *Polymer* **2007**, *48*, 3632.
- (110) Kumashiro, Y.; Ikezoe, Y.; Tamada, K.; Hara, M. *J. Phys. Chem. B* **2008**, *112*, 8291.
- (111) Zeng, Q.; Reuther, R.; Oxsher, J.; Wang, Q. *Bioorg. Chem.* **2008**, *36*, 255.
- (112) Zeng, Q.; Li, T.; Cash, B.; Li, S.; Xie, F.; Wang, Q. *Chem. Commun.* **2007**, *14*, 1453.
- (113) Hu, Y. X.; Samanta, D.; Parelkar, S. S.; Hong, S. W.; Wang, Q. A.; Russell, T. P.; Emrick, T. *Adv. Funct. Mater.* **2010**, *20*, 3603.
- (114) Mougin, N. C.; van Rijn, P.; Park, H.; Muller, A. H. E.; Boker, A. *Adv. Funct. Mater.* **2011**, *21*, 2470.
- (115) Fernandez, B.; Galvez, N.; Sanchez, P.; Cuesta, R.; Bermejo, R.; Dominguez-Vera, J. M. *J. Biol. Inorg. Chem.* **2008**, *13*, 349.
- (116) Fernandez, B.; Galvez, N.; Sanchez, P.; Morales, J.; Santoyo, F.; Cuesta, R.; Dominguez-Vera, J. M. *Inorg. Chim. Acta* **2007**, *360*, 3951.
- (117) Won, K.; Park, M. J.; Yoon, H. H.; Kim, J. H. *Ultramicroscopy* **2008**, *108*, 1342.
- (118) Mann, S.; Meldrum, F. *Adv. Mater.* **1991**, *3*, 316.
- (119) Meldrum, F. C.; Wade, V. J.; Nimmo, D. L.; Heywood, B. R.; Mann, S. *Nature* **1991**, *349*, 684.
- (120) Yoshimura, H. *Colloids Surf., A* **2006**, *282 + 283*, 464.
- (121) Iwahori, K.; Yamashita, I. *J. Cluster Sci.* **2007**, *18*, 358.
- (122) Macara, I. G.; Hoy, T. G.; Harrison, P. M. *Biochem. J.* **1972**, *126*, 151.
- (123) Dominguez-Vera Jose, M.; Colacio, E. *Inorg. Chem.* **2003**, *42*, 6983.
- (124) Galvez, N.; Sanchez, P.; Dominguez-Vera, J. M. *Dalton Trans.* **2005**, *15*, 2492.
- (125) Yan, F.; Zhang, Y.; Yuan, H. K.; Gregas, M. K.; Vo-Dinh, T. *Chem. Commun.* **2008**, *38*, 4579.
- (126) Yan, F.; Zhang, Y.; Kim, K. S.; Yuan, H. K.; Vo-Dinh, T. *Photochem. Photobiol.* **2010**, *86*, 662.
- (127) Aime, S.; Frullano, L.; Geninatti Crich, S. *Angew. Chem., Int. Ed.* **2002**, *41*, 1017.
- (128) Yang, Z.; Wang, X. Y.; Diao, H. J.; Zhang, J. F.; Li, H. Y.; Sun, H. Z.; Guo, Z. *J. Chem. Commun.* **2007**, *33*, 3453.
- (129) Xing, R. M.; Wang, X. Y.; Zhang, C. L.; Zhang, Y. M.; Wang, Q.; Yang, Z.; Guo, Z. *J. Inorg. Biochem.* **2009**, *103*, 1039.
- (130) Niemeyer, J.; Abe, S.; Hikage, T.; Ueno, T.; Erker, G.; Watanabe, Y. *Chem. Commun.* **2008**, *48*, 6519.
- (131) Liu, R. Y.; Loll, P. J.; Eckenhoff, R. G. *FASEB J.* **2005**, *19*, 567.
- (132) Liu, G. D.; Wang, J.; Wu, H.; Lin, Y. H. *Anal. Chem.* **2006**, *78*, 7417.
- (133) Liu, G.; Wang, J.; Lea, S. A.; Lin, Y. *ChemBioChem* **2006**, *7*, 1315.
- (134) Yu, F. L.; Li, G.; Qu, B.; Cao, W. *Biosens. Bioelectron.* **2010**, *26*, 1114.
- (135) Liu, G.; Wu, H.; Dohnalkova, A.; Lin, Y. *Anal. Chem.* **2007**, *79*, 5614.
- (136) Liu, G.; Wu, H.; Wang, J.; Lin, Y. *Small* **2006**, *2*, 1139.
- (137) Jaaskelainen, A.; Harinen, R. R.; Soukka, T.; Lamminmaki, U.; Korpimilki, T.; Virta, M. *Anal. Chem.* **2008**, *80*, 583.
- (138) Jaaskelainen, A.; Harinen, R.-R.; Lamminmaki, U.; Korpimaki, T.; Pelliniemi, L. J.; Soukka, T.; Virta, M. *Small* **2007**, *3*, 1362.
- (139) Jaaskelainen, A.; Soukka, T.; Lamminmaki, U.; Korpimaki, T.; Virta, M. *Biotechnol. Bioeng.* **2009**, *102*, 1012.
- (140) Wong, K. K. W.; Mann, S. *Adv. Mater.* **1996**, *8*, 928.
- (141) Wong, K. K. W.; Douglas, T.; Gider, S.; Awschalom, D. D.; Mann, S. *Chem. Mater.* **1998**, *10*, 279.
- (142) Iwahori, K.; Yoshizawa, K.; Muraoka, M.; Yamashita, I. *Inorg. Chem.* **2005**, *44*, 6393.
- (143) Meldrum, F. C.; Douglas, T.; Levi, S.; Arosio, P.; Mann, S. *J. Inorg. Biochem.* **1995**, *58*, 59.
- (144) Jolley, C. C.; Uchida, M.; Reichhardt, C.; Harrington, R.; Kang, S.; Klem, M. T.; Parise, J. B.; Douglas, T. *Chem. Mater.* **2010**, *22*, 4612.
- (145) St. Pierre, T. G.; Chua-anusorn, W.; Sipos, P.; Kron, I.; Webb, J. *Inorg. Chem.* **1993**, *32*, 4480.
- (146) Douglas, T.; Dickson, D. P. E.; Betteridge, S.; Charnock, J.; Garner, C. D.; Mann, S. *Science* **1995**, *269*, 54.
- (147) Mackle, P.; Charnock, J. M.; Garner, C. D.; Meldrum, F. C.; Mann, S. *J. Am. Chem. Soc.* **1993**, *115*, 8471.
- (148) Kalman, F. K.; Geninatti-Crich, S.; Aime, S. *Angew. Chem., Int. Ed.* **2010**, *49*, 612.
- (149) Hainfeld, J. F. *Proc. Natl. Acad. Sci. U.S.A.* **1992**, *89*, 11064.
- (150) Meldrum, F. C.; Heywood, B. R.; Mann, S. *Science* **1992**, *257*, 522.
- (151) Hosein, H. A.; Strongin, D. R.; Allen, M.; Douglas, T. *Langmuir* **2004**, *20*, 10283.
- (152) Pool, V.; Klem, M.; Jolley, C.; Arenholz, E. A.; Douglas, T.; Young, M.; Idzerda, Y. U. *J. Appl. Phys.* **2010**, *107*, 09B517.
- (153) Uchida, M.; Terashima, M.; Cunningham, C. H.; Suzuki, Y.; Willits, D. A.; Willis, A. F.; Yang, P. C.; Tsao, P. S.; McConnell, M. V.; Young, M. J.; Douglas, T. *Magn. Res. Med.* **2008**, *60*, 1073.
- (154) Prozorov, T.; Mallapragada, S. K.; Narasimhan, B.; Wang, L. J.; Palo, P.; Nilsen-Hamilton, M.; Williams, T. J.; Bazylinski, D. A.; Prozorov, R.; Canfield, P. C. *Adv. Funct. Mater.* **2007**, *17*, 951.
- (155) Clemente-Leon, M.; Coronado, E.; Soriano-Portillo, A.; Galvez, N.; Dominguez-Vera, J. M. *J. Mater. Chem.* **2007**, *17*, 49.
- (156) Ceolin, M.; Galvez, N.; Sanchez, P.; Fernandez, B.; Dominguez-Vera, J. M. *Eur. J. Inorg. Chem.* **2008**, *5*, 795.
- (157) Galvez, N.; Sanchez, P.; Dominguez-Vera, J. M.; Soriano-Portillo, A.; Clemente-Leon, M.; Coronado, E. *J. Mater. Chem.* **2006**, *16*, 2757.
- (158) Zhang, L.; Swift, J.; Butts, C. A.; Yerubandi, V.; Dmochowski, I. *J. Inorg. Biochem.* **2007**, *101*, 1719.
- (159) Zheng, B.; Yamashita, I.; Uenuma, M.; Iwahori, K.; Kobayashi, M.; Uraoka, Y. *Jpn. J. Appl. Phys., Part 2* **2010**, *21*, 045305.

- (160) Fan, R. L.; Chew, S. W.; Cheong, V. V.; Orner, B. P. *Small* **2010**, *6*, 1483.
- (161) Dominguez-Vera, J. M.; Galvez, N.; Sanchez, P.; Mota, A. J.; Trasobares, S.; Hernandez, J. C.; Calvino, J. J. *Eur. J. Inorg. Chem.* **2007**, *30*, 4823.
- (162) Suzuki, M.; Abe, M.; Ueno, T.; Abe, S.; Goto, T.; Toda, Y.; Akita, T.; Yamadae, Y.; Watanabe, Y. *Chem. Commun.* **2009**, *32*, 4871.
- (163) Shin, Y. S.; Dohnalkova, A.; Lin, Y. H. *J. Phys. Chem. C* **2010**, *114*, 5985.
- (164) Kang, S.; Lucon, J.; Varpness, Z. B.; Liepold, L.; Uchida, M.; Willits, D.; Young, M.; Douglas, T. *Angew. Chem., Int. Ed.* **2008**, *47*, 7845.
- (165) Zhang, L. B.; Laug, L.; Munchgesang, W.; Pippel, E.; Gosele, U.; Brandsch, M.; Knez, M. *Nano Lett.* **2010**, *10*, 219.
- (166) Zhang, B.; Harb, J. N.; Davis, R. C.; Kim, J. W.; Chu, S. H.; Choi, S.; Miller, T.; Watt, G. D. *Inorg. Chem.* **2005**, *44*, 3738.
- (167) Douglas, T.; Stark, V. T. *Inorg. Chem.* **2000**, *39*, 1828.
- (168) Okuda, M.; Iwahori, K.; Yamashita, I.; Yoshimura, H. *Biotechnol. Bioeng.* **2003**, *84*, 187.
- (169) Klem, M. T.; Mosolf, J.; Young, M.; Douglas, T. *Inorg. Chem.* **2008**, *47*, 2237.
- (170) Sanchez, P.; Valero, E.; Galvez, N.; Dominguez-Vera, J. M.; Marinone, M.; Poletti, G.; Corti, M.; Lascialfari, A. *Dalton Trans.* **2009**, *S*, 800.
- (171) Okuda, M.; Suzumoto, Y.; Yamashita, I. *Cryst. Growth Des.* **2011**, *11*, 2540.
- (172) Ensign, D.; Young, M.; Douglas, T. *Inorg. Chem.* **2004**, *43*, 3441.
- (173) Kang, S.; Jolley, C. C.; Liepold, L. O.; Young, M.; Douglas, T. *Angew. Chem., Int. Ed.* **2009**, *48*, 4772.
- (174) Okuda, M.; Kobayashi, Y.; Suzuki, K.; Sonoda, K.; Kondoh, T.; Wagawa, A.; Kondo, A.; Yoshimura, H. *Nano Lett.* **2005**, *5*, 991.
- (175) Wu, H.; Engelhard, M. H.; Wang, J.; Fisher, D. R.; Lin, Y. J. *Mater. Chem.* **2008**, *18*, 1779.
- (176) Li, M.; Viravaidya, C.; Mann, S. *Small* **2007**, *3*, 1477.
- (177) Fukano, H.; Aizawa, M.; Yoshimura, H. 20th International Symposium on Ceramics in Medicine, Nantes, France, 2007; p 183.
- (178) Naito, M.; Iwahori, K.; Miura, A.; Yamane, M.; Yamashita, I. *Angew. Chem., Int. Ed.* **2010**, *49*, 7006.
- (179) Iwahori, K.; Enomoto, T.; Furusho, H.; Miura, A.; Nishio, K.; Mishima, Y.; Yamashita, I. *Chem. Mater.* **2007**, *19*, 3105.
- (180) Okuda, M.; Suzumoto, Y.; Iwahori, K.; Kang, S.; Uchida, M.; Douglas, T.; Yamashita, I. *Chem. Commun.* **2010**, *46*, 8797.
- (181) Xing, R. M.; Wang, X. Y.; Yan, L. L.; Zhang, C. L.; Yang, Z.; Wang, X. H.; Guo, Z. J. *Dalton Trans.* **2009**, *10*, 1710.
- (182) Yoshizawa, K.; Iwahori, K.; Sugimoto, K.; Yamashita, I. *Chem. Lett.* **2006**, *35*, 1192.
- (183) Iwahori, K.; Takagi, R.; Kishimoto, N.; Yamashita, I. *Mater. Lett.* **2011**, *65*, 3245.
- (184) Hennequin, B.; Turyanska, L.; Ben, T.; Beltran, A. M.; Molina, S. I.; Li, M.; Mann, S.; Patane, A.; Thomas, N. R. *Adv. Mater.* **2008**, *20*, 3592.
- (185) Dominguez-Vera, J. M.; Colacio, E. *Inorg. Chem.* **2003**, *42*, 6983.
- (186) Liu, R.; Loll, J. P.; Eckenhoff, G. R. *FASEB J.* **2005**, *19*, 567.
- (187) Takezawa, Y.; Boeckmann, P.; Sugi, N.; Wang, Z.; Abe, S.; Murakami, T.; Hikage, T.; Erker, G.; Watanabe, Y.; Kitagawa, S.; Ueno, T. *Dalton Trans.* **2011**, *40*, 2190.
- (188) Wang, Z.; Takezawa, Y.; Aoyagi, H.; Abe, S.; Hikage, T.; Watanabe, Y.; Kitagawa, S.; Ueno, T. *Chem. Commun.* **2011**, *47*, 170.
- (189) Abe, S.; Hikage, T.; Watanabe, Y.; Kitagawa, S.; Ueno, T. *Inorg. Chem.* **2010**, *49*, 6967.
- (190) Abe, S.; Niemeyer, J.; Abe, M.; Takezawa, Y.; Ueno, T.; Hikage, T.; Erker, G.; Watanabe, Y. *J. Am. Chem. Soc.* **2008**, *130*, 10512.
- (191) Tsukamoto, R.; Iwahori, K.; Muraoka, M.; Yamashita, I. *Bull. Chem. Soc. Jpn.* **2005**, *78*, 2075.
- (192) Kim, J. W.; Choi, S. H.; Lillehei, P. T.; Chu, S. H.; King, G. C.; Watt, G. D. *Chem. Commun.* **2005**, *32*, 4101.
- (193) Wu, H.; Wang, J.; Wang, Z.; Fisher, D. R.; Lin, Y. J. *Nanosci. Nanotechnol.* **2008**, *8*, 2316.
- (194) Yamashita, I.; Hayashi, J.; Hara, M. *Chem. Lett.* **2004**, *33*, 1158.
- (195) Iwahori, K.; Morioka, T.; Yamashita, I. *Phys. Status Solidi A* **2006**, *203*, 2658.
- (196) Iwahori, K.; Yamashita, I. *Jpn. J. Appl. Phys., Part 2* **2008**, *49*, 495601.
- (197) Wang, Z. Y.; Takezawa, Y.; Aoyagi, H.; Abe, S.; Hikage, T.; Watanabe, Y.; Kitagawa, S.; Ueno, T. *Chem. Commun.* **2011**, *47*, 170.
- (198) Ueno, T.; Abe, M.; Hirata, K.; Abe, S.; Suzuki, M.; Shimizu, N.; Yamamoto, M.; Takata, M.; Watanabe, Y. *J. Am. Chem. Soc.* **2009**, *131*, 5094.
- (199) Ceolin, M.; Galvez, N.; Dominguez-Verab, J. M. *Phys. Chem. Chem. Phys.* **2008**, *10*, 4327.
- (200) Turyanska, L.; Bradshaw, T. D.; Sharpe, J.; Li, M.; Mann, S.; Thomas, N. R.; Patane, A. *Small* **2009**, *5*, 1738.
- (201) Resnick, D. A.; Gilmore, K.; Idzerda, Y. U.; Klem, M. T.; Allen, M.; Douglas, T.; Arenholz, E.; Young, M. *J. Appl. Phys.* **2006**, *99*, 08Q501.
- (202) Usselman, R. J.; Klem, M. T.; Russek, S. E.; Young, M.; Douglas, T.; Goldfarb, R. B. *J. Appl. Phys.* **2010**, *107*, 114703.
- (203) Nagayama, K. *Adv. Biophys.* **1997**, *34*, 3.
- (204) Aoyama, K.; Ogawa, K.; Kimura, Y.; Fujiyoshi, Y. *Ultramicroscopy* **1995**, *57*, 345.
- (205) Scheybani, T.; Yoshimura, H.; Baumeister, W.; Nagayama, K. *Langmuir* **1996**, *12*, 431.
- (206) Yoshimura, H.; Scheybani, T.; Baumeister, W.; Nagayama, K. *Langmuir* **1994**, *10*, 3290.
- (207) Nagayama, K.; Takeda, S.; Endo, S.; Yoshimura, H. *Jpn. J. Appl. Phys., Part 1* **1995**, *34*, 3947.
- (208) Yoshimura, H. *Adv. Biophys.* **1997**, *34*, 93.
- (209) Yoshimura, H.; Matsumoto, M.; Endo, S.; Nagayama, K. *Ultramicroscopy* **1990**, *32*, 265.
- (210) Yamaki, M.; Matsubara, K.; Nagayama, K. *Langmuir* **1993**, *9*, 3154.
- (211) Dimitrov, A. S.; Yoshimura, H.; Nagayama, K. *Langmuir* **1995**, *11*, 3937.
- (212) Furuno, T.; Sasabe, H.; Ulmer, K. M. *Thin Solid Films* **1989**, *180*, 23.
- (213) Yamashita, I. *Thin Solid Films* **2001**, *393*, 12.
- (214) Kobayashi, K.; Ishii, N.; Sasabe, H.; Knoll, W. *Biosci. Biotechnol. Biochem.* **2001**, *65*, 176.
- (215) Johnson, C. A.; Yuan, Y.; Lenhoff, A. M. *J. Colloid Interface Sci.* **2000**, *223*, 261.
- (216) Bergkvist, M.; Mark, S. S.; Yang, X.; Angert, E. R.; Batt, C. A. *J. Phys. Chem. B* **2004**, *108*, 8241.
- (217) Jutz, G. *Mineralized Bionanoparticle Pickering Emulsions*; University of Bayreuth: Germany, 2008; <http://opus.ub.uni-bayreuth.de/volltexte/2009/508/>.
- (218) Fujii, S.; Aichi, A.; Muraoka, M.; Kishimoto, N.; Iwahori, K.; Nakamura, Y.; Yamashita, I. *J. Colloid Interface Sci.* **2009**, *338*, 222.
- (219) Miller, R.; Aksenenko, E. V.; Fainerman, V. B.; Pison, U. *Colloids Surf., A* **2001**, *183*, 381.
- (220) Yampolskaya, G.; Platikanov, D. *Adv. Colloid Interface Sci.* **2006**, *128*, 159.
- (221) Beverung, C. J.; Radke, C. J.; Blanch, H. W. *Biophys. Chem.* **1999**, *81*, 59.
- (222) van Rijn, P.; Mougin, N. C.; Franke, D.; Park, H.; Boeker, A. *Chem. Commun.* **2011**, *47*, 8376.
- (223) van Rijn, P.; Mougin, N. C.; Boker, A. *Polymer* **2012**, *53*, 6045.
- (224) Tangirala, R.; Hu, Y. X.; Joralemon, M.; Zhang, Q. L.; He, J. B.; Russell, T. P.; Emrick, T. *Soft Matter* **2009**, *5*, 1048.
- (225) Fromherz, P. *Nature* **1971**, *231*, 267.
- (226) Britt, D. W.; Mobius, D.; Hlady, V. *Phys. Chem. Chem. Phys.* **2000**, *2*, 4594.
- (227) Clemente-Leon, M.; Coronado, E.; Soriano-Portillo, A.; Martin-Romero, M. T.; Perez-Morales, M.; Dominguez-Vera, J. M.; Galvez, N. *Polyhedron* **2007**, *26*, 1871.

- (228) Clemente-Leon, M.; Coronado, E.; Soriano-Portillo, A.; Mingotaud, C.; Dominguez-Vera, J. M. *Adv. Colloid Interface Sci.* **2005**, *116*, 193.
- (229) Velev, O. D. *Adv. Biophys.* **1997**, *34*, 139.
- (230) Hikono, T.; Uraoka, Y.; Fuyuki, T.; Yamashita, I. *Jpn. J. Appl. Phys., Part 2* **2003**, *42*, L398.
- (231) Masuda, H.; Matsui, Y.; Miwa, T.; Nagae, M.; Tanji, M.; Nishio, K. *Chem. Lett.* **2006**, *35*, 192.
- (232) Kwon, M.; Choi, H.; Chang, M.; Jo, M.; Jung, S.-J.; Hwang, H. *Appl. Phys. Lett.* **2007**, *90*, 193512.
- (233) Miura, A.; Uraoka, Y.; Fuyuki, T.; Kumagai, S.; Yoshii, S.; Matsukawa, N.; Yamashita, I. *Surf. Sci.* **2007**, *601*, L81.
- (234) Yuan, Z.; Petsev, D. N.; Prevo, B. G.; Velev, O. D.; Atanassov, P. *Langmuir* **2007**, *23*, 5498.
- (235) Hu, Y.; Samanta, D.; Parelkar, S. S.; Hong, S. W.; Wang, Q.; Russel, T. P.; Emrick, T. *Adv. Funct. Mater.* **2010**, *20*, 3603.
- (236) Ibrahim, S.; Ito, T. *Langmuir* **2010**, *26*, 2119.
- (237) Sousa, A.; Sengonul, M.; Latour, R.; Kohn, J.; Libera, M. *Langmuir* **2006**, *22*, 6286.
- (238) Onda, M.; Lvov, Y.; Ariga, K.; Kunitake, T. *Jpn. J. Appl. Phys., Part 2* **1997**, *36*, L1608.
- (239) Uto, K.; Yamamoto, K.; Kishimoto, N.; Muraoka, M.; Aoyagi, T.; Yamashita, I. *J. Mater. Chem.* **2008**, *18*, 3876.
- (240) Sano, K.; Sasaki, H.; Shiba, K. *J. Am. Chem. Soc.* **2006**, *128*, 1717.
- (241) Sano, K. I.; Yoshii, S.; Yamashita, I.; Shiba, K. *Nano Lett.* **2007**, *7*, 3200.
- (242) Li, M.; Wong, K. K. W.; Mann, S. *Chem. Mater.* **1999**, *11*, 23.
- (243) Li, M.; Mann, S. *J. Mater. Chem.* **2004**, *14*, 2260.
- (244) Srivastava, S.; Samanta, B.; Jordan, B. J.; Hong, R.; Xiao, Q.; Tuominen, M. T.; Rotello, V. M. *J. Am. Chem. Soc.* **2007**, *129*, 11776.
- (245) Dominguez-Vera, J.; Welte, L.; Galvez, N.; Fernandez, B.; Gomez-Herrero, J.; Zamora, F. *Nanotechnology* **2008**, *19*, 025302.
- (246) Park, C. W.; Park, H. J.; Kim, J. H.; Won, K.; Yoon, H. H. *Ultramicroscopy* **2009**, *109*, 1001.
- (247) Lam, S. K. H.; Yang, W.; Wiogo, H. T. R.; Foley, C. P. *Nanotechnology* **2008**, *19*, 285303.
- (248) Scott, B. L.; Zapien, D. C. *Electroanalysis* **2010**, *22*, 379.
- (249) Casella, S. S.; Ritzert, N. L.; Zapien, D. C. *Electroanalysis* **2009**, *21*, 811.
- (250) Hu, Y. X.; Chen, D. A.; Park, S.; Emrick, T.; Russell, T. P. *Adv. Mater.* **2010**, *22*, 2583.
- (251) Masuda, H.; Hogi, H.; Nishio, K.; Matsumoto, F. *Chem. Lett.* **2004**, *33*, 812.
- (252) Caruso, F.; Furlong, D. N.; Kingshott, P. *J. Colloid Interface Sci.* **1997**, *186*, 129.
- (253) Feng, L.; Damodaran, S. *Thin Solid Films* **2000**, *365*, 99.
- (254) Stenberg, M.; Nygren, H. *Biophys. Chem.* **1991**, *41*, 131.
- (255) Ngunjiri, J. N.; Daniels, S. L.; Li, J. R.; Serem, W. K.; Garno, J. C. *Nanomedicine* **2008**, *3*, 529.
- (256) Poor, V.; Kasyutich, O.; Hallam, K. R.; Schwarzacher, W. *Acta Phys. Polym., A* **2010**, *117*, 394.
- (257) Manning, E.; Yau, S. T. *J. Vac. Sci. Technol., B* **2005**, *23*, 2309.
- (258) Yoshii, S.; Yamada, K.; Matsukawa, N.; Yamashita, I. *Jpn. J. Appl. Phys., Part 1* **2005**, *44*, 1518.
- (259) Yamada, K.; Yoshii, S.; Kumagai, S.; Fujiwara, I.; Nishio, K.; Okuda, M.; Matsukawa, N.; Yamashita, I. *Jpn. J. Appl. Phys., Part 1* **2006**, *45*, 4259.
- (260) Yoshinobu, T.; Suzuki, J.; Kurooka, H.; Moon, W. C.; Iwasaki, H. *Electrochim. Acta* **2003**, *48*, 3131.
- (261) Tominaga, M.; Matsumoto, M.; Soejima, K.; Taniguchi, I. *J. Colloid Interface Sci.* **2006**, *299*, 761.
- (262) Choi, J.-W.; Kim, Y. J.; Kim, S.-U.; Min, J.; Oh, B.-K. *Ultramicroscopy* **2008**, *108*, 1356.
- (263) Kumagai, S.; Yoshii, S.; Yamada, K.; Fujiwara, I.; Matsukawa, N.; Yamashita, I. *J. Photopolym. Sci. Technol.* **2005**, *18*, 495.
- (264) Kumagai, S.; Yoshii, S.; Yamada, K.; Matsukawa, N.; Fujiwara, I.; Iwahori, K.; Yamashita, I. *Appl. Phys. Lett.* **2006**, *88*, 153103.
- (265) Kumagai, S.; Yoshii, S.; Yamada, K.; Matsukawa, N.; Iwahori, K.; Yamashita, I. *Jpn. J. Appl. Phys., Part 1* **2006**, *45*, 8311.
- (266) Yoshii, S.; Kumagai, S.; Nishio, K.; Kadotani, A.; Yamashita, I. *Appl. Phys. Lett.* **2009**, *95*, 133702.
- (267) Martinez, R. V.; Martinez, J.; Chiesa, M.; Garcia, R.; Coronado, E.; Pinilla-Cienfuegos, E.; Tatay, S. *Adv. Mater.* **2010**, *22*, 588.
- (268) Fukuta, M.; Yamashita, I. *Colloids Surf., B* **2010**, *75*, 323.
- (269) Miura, A.; Hikono, T.; Matsumura, T.; Yano, H.; Hatayama, T.; Uraoka, Y.; Fuyuki, T.; Yoshii, S.; Yamashita, I. *Jpn. J. Appl. Phys., Part 2* **2006**, *45*, L1.
- (270) Ritzert, N. L.; Casella, S. S.; Zapien, D. C. *Electrochem. Commun.* **2009**, *11*, 827.
- (271) Martin, T. D.; Monheit, S. A.; Niichel, R. J.; Peterson, S. C.; Campbell, C. H.; Zapien, D. C. *J. Electroanal. Chem.* **1997**, *420*, 279.
- (272) Tominaga, M.; Taniguchi, I. *Chem. Lett.* **2001**, 704.
- (273) Tominaga, M.; Ohira, A.; Yamaguchi, Y.; Kunitake, M. *J. Electroanal. Chem.* **2004**, *566*, 323.
- (274) Tominaga, M.; Ohira, A.; Kubo, A.; Taniguchi, I.; Kunitake, M. *Chem. Commun.* **2004**, *1518*.
- (275) Bellido, E.; de Miguel, R.; Ruiz-Molina, D.; Lostao, A.; Maspoche, D. *Adv. Mater.* **2010**, *22*, 352.
- (276) Bellido, E.; de Miguel, R.; Sese, J.; Ruiz-Molina, D.; Lostao, A.; Maspoche, D. *Scanning* **2010**, *32*, 35.
- (277) Ishikawa, K.; Yamada, K.; Kumagai, S.; Sano, K.-i.; Shiba, K.; Yamashita, I.; Kobayashi, M. *Appl. Phys. Express* **2008**, *1*, 034006.
- (278) Matsukawa, N.; Nishio, K.; Sano, K.; Shiba, K.; Yamashita, I. *Langmuir* **2009**, *25*, 3327.
- (279) Yamashita, K.; Kirimura, H.; Okuda, M.; Nishio, K.; Sano, K. I.; Shiba, K.; Hayashi, T.; Hara, M.; Mishima, Y. *Small* **2006**, *2*, 1148.
- (280) Hayashi, T.; Sano, K. I.; Shiba, K.; Iwahori, K.; Yamashita, I.; Hara, M. *Langmuir* **2009**, *25*, 10901.
- (281) Matsui, T.; Matsukawa, N.; Iwahori, K.; Sano, K. I.; Shiba, K.; Yamashita, I. *Langmuir* **2007**, *23*, 1615.
- (282) Tominaga, M.; Taniguchi, I. *Chem. Lett.* **2003**, *32*, 954.
- (283) Martin, K. C.; Villano, S. M.; McCurdy, P. R.; Zapien, D. C. *Langmuir* **2003**, *19*, 5808.
- (284) Pyon, M. S.; Cherry, R. J.; Bjornsen, A. J.; Zapien, D. C. *Langmuir* **1999**, *15*, 7040.
- (285) Zapien, D. C.; Johnson, M. A. *J. Electroanal. Chem.* **2000**, *494*, 114.
- (286) Tominaga, M.; Miyahara, K.; Soejima, K.; Nomura, S.; Matsumoto, M.; Taniguchi, I. *J. Colloid Interface Sci.* **2007**, *313*, 135.
- (287) Tominaga, M.; Soejima, K.; Matsumoto, M.; Taniguchi, I. *J. Electroanal. Chem.* **2005**, *579*, 51.
- (288) Tominaga, M.; Soejima, K.; Taniguchi, I. *J. Electroanal. Chem.* **2008**, *617*, 78.
- (289) Wu, Y. H.; Hu, S. S. *Anal. Chim. Acta* **2004**, *527*, 37.
- (290) Inamuddin; Shin, K. M.; Kim, S. I.; So, I.; Kim, S. J. *Electrochim. Acta* **2009**, *54*, 3979.
- (291) Lee, S.-Y.; Lim, J.-S.; Harris, M. T. *Biotechnol. Bioeng.* **2012**, *109*, 16.
- (292) Carregal-Romero, S.; Buurma, N. J.; Pérez-Juste, J.; Liz-Marzán, L. M.; Hervés, P. *Chem. Mater.* **2010**, *22*, 3051.
- (293) Garcia, A. C. H. *Chem. Soc. Rev.* **2008**, *37*, 2096.
- (294) Kim, K. T.; Meeuwissen, S. A.; Nolte, R. J. M.; van Hest, J. C. M. *Nanoscale* **2010**, *2*, 844.
- (295) Vriezema, D. M.; Aragones, M. C.; Elemans, J.; Cornelissen, J.; Rowan, A. E.; Nolte, R. J. M. *Chem. Rev.* **2005**, *105*, 1445.
- (296) Kim, I.; Hosein, H.-A.; Strongin, D. R.; Douglas, T. *Chem. Mater.* **2002**, *14*, 4874.
- (297) Zhang, N.; Li, F. Y.; Fu, Q. J.; Tsang, S. C. *React. Kinet. Catal. Lett.* **2000**, *71*, 393.
- (298) Nikandrov, V. V.; Gratzel, C. K.; Moser, J. E.; Gratzel, M. J. *Photochem. Photobiol., B* **1997**, *41*, 83.
- (299) Kirimura, H.; Uraoka, Y.; Fuyuki, T.; Okuda, M.; Yamashita, I. *Appl. Phys. Lett.* **2005**, *86*, 262106.
- (300) Tojo, Y.; Miura, A.; Yamashita, I.; Uraoka, Y. *Jpn. J. Appl. Phys.* **2011**, *S0*, 04DL12.

- (301) Oh, J. H.; Kim, E. H.; Kang, D. H.; Ryu, J. H.; Jang, J. *Electrochem. Solid-State Lett.* **2006**, *9*, H96.
- (302) Tasis, D.; Tagmatarchis, N.; Bianco, A.; Prato, M. *Chem. Rev.* **2006**, *106*, 1105.
- (303) Chen, R. J.; Zhang, Y. G.; Wang, D. W.; Dai, H. J. *J. Am. Chem. Soc.* **2001**, *123*, 3838.
- (304) Azamian, B. R.; Davis, J. J.; Coleman, K. S.; Bagshaw, C. B.; Green, M. L. H. *J. Am. Chem. Soc.* **2002**, *124*, 12664.
- (305) Jiang, K. Y.; Schadler, L. S.; Siegel, R. W.; Zhang, X. J.; Zhang, H. F.; Terrones, M. *J. Mater. Chem.* **2004**, *14*, 37.
- (306) Lin, Y.; Allard, L. F.; Sun, Y. P. *J. Phys. Chem. B* **2004**, *108*, 3760.
- (307) Shin, K. M.; Lee, J. W.; Wallace, G. G.; Lim, S. J. *Sens. Actuators, B: Chem.* **2008**, *133*, 393.
- (308) Lee, J. W.; Shin, K. M.; Lynam, C.; Spinks, G. M.; Wallace, G. G.; Kim, S. J. *Smart Mater. Struct.* **2008**, *17*, 045029.
- (309) Dechakiatkrai, C.; Chen, J.; Lynam, C.; Shin, K. M.; Kim, S. J.; Phanichphant, S.; Wallace, G. G. *Electrochem. Solid-State Lett.* **2008**, *11*, K4.
- (310) Bhattacharyya, S.; Sinturel, C.; Salvietat, J. P.; Saboungi, M. L. *Appl. Phys. Lett.* **2005**, *86*, 113104.
- (311) Shin, M. K.; Kim, S. I.; Kim, S. J.; Kim, S. K.; Lee, H. *Appl. Phys. Lett.* **2006**, *88*, 193901.
- (312) Shin, M. K.; Kim, S. I.; Kim, S. J.; Kim, B. J.; So, I.; Kozlov, M. E.; Oh, J.; Baughman, R. H. *Appl. Phys. Lett.* **2008**, *93*, 163902.
- (313) Shin, M. K.; Spinks, G. M.; Shin, S. R.; Kim, S. I.; Kim, S. J. *Adv. Mater.* **2009**, *21*, 1712.
- (314) Shin, M. K.; Kim, S. I.; Kim, S. J.; Park, S. Y.; Hyun, Y. H.; Lee, Y.; Lee, K. E.; Han, S. S.; Jang, D. P.; Kim, Y. B.; Cho, Z. H.; So, I.; Spinks, G. M. *Langmuir* **2008**, *24*, 12107.
- (315) Kim, M. S.; Shin, K. M.; Kim, S. I.; Spinks, G. M.; Kim, S. J. *Macromol. Rapid Commun.* **2008**, *29*, 552.
- (316) Ko, S.; Jang, J. *Biomacromolecules* **2007**, *8*, 1400.
- (317) Li, Y. M.; Kim, W.; Zhang, Y. G.; Rolandi, M.; Wang, D. W.; Dai, H. J. *J. Phys. Chem. B* **2001**, *105*, 11424.
- (318) Takagi, D.; Yamazaki, A.; Otsuka, Y.; Yoshimura, H.; Kobayashi, Y.; Homma, Y. *Chem. Phys. Lett.* **2007**, *445*, 213.
- (319) Durrer, L.; Greenwald, J.; Helbling, T.; Muoth, M.; Riek, R.; Hierold, C. *Nanotechnology* **2009**, *20*, 355601.
- (320) Zhang, Y.; Li, Y.; Kim, W.; Wang, D.; Dai, H. *Appl. Phys. A: Mater.* **2002**, *74*, 325.
- (321) Kim, W.; Choi, H. C.; Shim, M.; Li, Y. M.; Wang, D. W.; Dai, H. J. *Nano Lett.* **2002**, *2*, 703.
- (322) Bonard, J. M.; Chauvin, P.; Klinke, C. *Nano Lett.* **2002**, *2*, 665.
- (323) Kondo, D.; Sato, S.; Kawabata, A.; Awano, Y. *Jpn. J. Appl. Phys., Part 1* **2005**, *44*, S292.
- (324) Choi, H. C.; Kim, W.; Wang, D. W.; Dai, H. J. *J. Phys. Chem. B* **2002**, *106*, 12361.
- (325) Durrer, L.; Helbling, T.; Zenger, C.; Jungen, A.; Stampfer, C.; Hierold, C. *Sens. Actuators, B: Chem.* **2008**, *B132*, 485.
- (326) An, Y. L.; Liu, Y. Q.; Yuan, X.; Tan, H. *Int. J. Mod. Phys. B* **2009**, *23*, 1529.
- (327) Haffner, M.; Schneider, K.; Schuster, B. E.; Stamm, B.; Latteyer, F.; Fleischer, M.; Burkhardt, C.; Chasse, T.; Stett, A.; Kern, D. P. *Microelectron. Eng.* **2010**, *87*, 734.
- (328) Tempel, H.; Joshi, R.; Schneider, J. *J. Mater. Chem. Phys.* **2010**, *121*, 178.
- (329) Kumagai, S.; Ono, T.; Yoshii, S.; Kadotani, A.; Tsukamoto, R.; Nishio, K.; Okuda, M.; Yamashita, I. *Appl. Phys. Express* **2010**, *3*, 015101.
- (330) Jeong, G.-H.; Yamazaki, A.; Suzuki, S.; Yoshimura, H.; Kobayashi, Y.; Homma, Y. *J. Am. Chem. Soc.* **2005**, *127*, 8238.
- (331) Tsang, S. C.; Qiu, J.; Harris, P. J. F.; Fu, Q. J.; Zhang, N. *Chem. Phys. Lett.* **2000**, *322*, 553.
- (332) Kameta, N.; Masuda, M.; Minamikawa, H.; Mishima, Y.; Yamashita, I.; Shimizu, T. *Chem. Mater.* **2007**, *19*, 3553.
- (333) Shimizu, T. *J. Polym. Sci., Part A: Polym. Chem.* **2005**, *44*, 5137.
- (334) Yui, H.; Shimizu, Y.; Kamiya, S.; Yamashita, I.; Masuda, M.; Ito, K.; Shimizu, T. *Chem. Lett.* **2005**, *34*, 232.
- (335) Yamashita, I. *Mater. Res. Soc. Symp. Proc.* **2005**, *873E*, K5 1.
- (336) Fujisaki, Y. *Jpn. J. Appl. Phys.* **2010**, *49*, 100001.
- (337) Miura, A.; Tsukamoto, R.; Yoshii, S.; Yamashita, I.; Uraoka, Y.; Fuyuki, T. *Nanotechnology* **2008**, *19*, 255201.
- (338) Miura, A.; Uraoka, Y.; Fuyuki, T.; Yoshii, S.; Yamashita, I. *J. Appl. Phys.* **2008**, *103*, 074503.
- (339) Hikono, T.; Matsumura, T.; Miura, A.; Uraoka, Y.; Fuyuki, T.; Takeguchi, M.; Yoshii, S.; Yamashita, I. *Appl. Phys. Lett.* **2006**, *88*, 023108.
- (340) Hikono, T.; Uraoka, Y.; Fuyuki, T.; Yoshii, S.; Yamashita, I.; Takeguchi, M. *Surf. Sci.* **2006**, *600*, 2817.
- (341) Tojo, Y.; Miura, A.; Uraoka, Y.; Fuyuki, T.; Yamashita, I. *Jpn. J. Appl. Phys.* **2009**, *48*, 04C190.
- (342) Ichikawa, K.; Fujii, M.; Uraoka, Y.; Punchaipetch, P.; Yano, H.; Hatayama, T.; Fuyuki, T.; Yamashita, I. *J. Korean Phys. Soc.* **2009**, *54*, 554.
- (343) Ichikawa, K.; Uraoka, Y.; Punchaipetch, P.; Yano, H.; Hatayama, T.; Fuyuki, T.; Yamashita, I. *Jpn. J. Appl. Phys., Part 2* **2007**, *46*, L804.
- (344) Kwon, M.; Choi, H.; Chang, M.; Jung, S. J.; Hwang, H. *Electron. Mater. Lett.* **2007**, *3*, 121.
- (345) Ohara, K.; Uraoka, Y.; Fuyuki, T.; Yamashita, I.; Yaegashi, T.; Moniwa, M.; Yoshimaru, M. *Jpn. J. Appl. Phys.* **2009**, *48*, 04C153.
- (346) Ohara, K.; Yamashita, I.; Yaegashi, T.; Moniwa, M.; Yoshimaru, M.; Uraoka, Y. *Appl. Phys. Express* **2009**, *2*, 095001.
- (347) Yamada, K.; Yoshii, S.; Kumagai, S.; Miura, A.; Uraoka, Y.; Fuyuki, T.; Yamashita, I. *Jpn. J. Appl. Phys., Part 1* **2007**, *46*, 7549.
- (348) Ohara, K.; Yamashita, I.; Uraoka, Y. *Jpn. J. Appl. Phys.* **2010**, *49*, 04DJ05.
- (349) Yamada, K.; Yoshii, S.; Kumagai, S.; Miura, A.; Uraoka, Y.; Fuyuki, T.; Yamashita, I. *Jpn. J. Appl. Phys., Part 1* **2006**, *45*, 8946.
- (350) Yamazaki, G.; Uraoka, Y.; Fuyuki, T.; Yamashita, I. *J. Photopolym. Sci. Technol.* **2003**, *16*, 439.
- (351) Kubota, T.; Baba, T.; Samukawa, S.; Kawashima, H.; Uraoka, Y.; Fuyuki, T.; Yamashita, I. *Appl. Phys. Lett.* **2004**, *84*, 1555.
- (352) Kubota, T.; Baba, T.; Saito, S.; Yamasaki, S.; Kumagai, S.; Matsui, T.; Uraoka, Y.; Fuyuki, T.; Yamashita, I.; Samukawa, S. *J. Vac. Sci. Technol., B* **2007**, *25*, 760.
- (353) Kubota, T.; Baba, T.; Kawashima, H.; Uraoka, Y.; Fuyuki, T.; Yamashita, I.; Samukawa, S. *J. Vac. Sci. Technol., B* **2005**, *23*, 534.
- (354) Kubota, T.; Hashimoto, T.; Ishikawa, Y.; Samukawa, S.; Miura, A.; Uraoka, Y.; Fuyuki, T.; Takeguchi, M.; Nishioka, K.; Yamashita, I. *Appl. Phys. Lett.* **2006**, *89*, 233127.
- (355) Kubota, T.; Hashimoto, T.; Takeguchi, M.; Nishioka, K.; Uraoka, Y.; Fuyuki, T.; Yamashita, I.; Samukawa, S. *J. Appl. Phys.* **2007**, *101*, 124301.
- (356) Huang, C.-H.; Igarashi, M.; Nishioka, K.; Takeguchi, M.; Uraoka, Y.; Fuyuki, T.; Yamashita, I.; Samukawa, S. *Appl. Phys. Express* **2008**, *1*, 084002.
- (357) Samukawa, S.; Kubota, T.; Huang, C.-H.; Hashimoto, T.; Igarashi, M.; Nishioka, K.; Takeguchi, M.; Uraoka, Y.; Fuyuki, T.; Yamashita, I. *Appl. Phys. Express* **2008**, *1*, 074002.
- (358) Huang, C. H.; Igarashi, M.; Wone, M.; Uraoka, Y.; Fuyuki, T.; Takeguchi, M.; Yamashita, I.; Samukawa, S. *Jpn. J. Appl. Phys.* **2009**, *48*, 04C187.
- (359) Nakama, Y.; Nagamachi, S.; Ohta, J.; Nunoshita, M. *Appl. Phys. Express* **2008**, *1*, 034001.
- (360) Nakama, Y.; Ohta, J.; Nunoshita, M. *Jpn. J. Appl. Phys.* **2008**, *47*, 3028.
- (361) Nakama, Y.; Minakawa, K.; Ohta, J.; Nunoshita, M. *Appl. Phys. Lett.* **2007**, *91*, 203102.
- (362) Fujikawa, S.; Muto, E.; Kunitake, T. *Langmuir* **2007**, *23*, 4629.
- (363) Luzzago, A.; Cesareni, G. *EMBO J.* **1989**, *8*, 569.
- (364) Lee, S. H.; Lee, H.; Park, J. S.; Choi, H.; Han, K. Y.; Seo, H. S.; Ahn, K. Y.; Han, S. S.; Cho, Y.; Lee, K. H.; Lee, J. *FASEB J.* **2007**, *21*, 1324.
- (365) MaHam, A.; Tang, Z. W.; Wu, H.; Wang, J.; Lin, Y. H. *Small* **2009**, *5*, 1706.

- (366) Jain, S. K.; Chaurasiya, A.; Gupta, Y.; Jain, A.; Dagur, P.; Joshi, B.; Katoch, V. M. *J. Microencapsulation* **2008**, *25*, 289.
- (367) Debottin, N.; Zer, H.; Parnes, M.; Harush-Frenkel, O.; Kadouche, J.; Benita, S. *Eur. J. Pharm. Biopharm.* **2010**, *74*, 148.
- (368) Wardeska, J. G.; Viglione, B.; Chasteen, N. D. *J. Biol. Chem.* **1986**, *261*, 6677.
- (369) Tsukube, H.; Noda, Y.; Shinoda, S. *Chem.—Eur. J.* **2010**, *16*, 4273.
- (370) Shapiro, M. G.; Szablowski, J. O.; Langer, R.; Jasanoff, A. *J. Am. Chem. Soc.* **2009**, *131*, 2484.
- (371) Rifkind, R. A.; Hsu, K. C.; Morgan; Seegal, B. C.; Knox, A. W.; Rose, H. M. *Nature* **1960**, *187*, 1094.
- (372) Haigler, H. T.; McKenna, J. A.; Cohen, S. *J. Cell Biol.* **1979**, *81*, 382.
- (373) Moll, W. D.; Guo, P. *J. Nanosci. Nanotechnol.* **2007**, *7*, 3257.
- (374) Klem, M. T.; Young, M.; Douglas, T. *Mater. Today* **2005**, *8*, 28.
- (375) Cao, C. Q.; Tian, L. X.; Liu, Q. S.; Liu, W. F.; Chen, G. J.; Pan, Y. X. *J. Geophys. Res.: Solid Earth* **2010**, *115*, B07103.
- (376) Makhlof, S. A.; Parker, F. T.; Berkowitz, A. E. *Phys. Rev. B* **1997**, *55*, 14717.
- (377) Tejada, J.; Zhang, X. X. *J. Phys.: Condens. Matter* **1994**, *6*, 263.
- (378) Gider, S.; Awschalom, D. D.; Douglas, T.; Mann, S.; Chaparala, M. *Science* **1995**, *268*, 77.
- (379) Kilcoyne, S. H.; Cywinski, R. *J. Magn. Magn. Mater.* **1995**, *140*, 1466.
- (380) Silva, N. J. O.; Amaral, V. S.; Urtizberea, A.; Bustamante, R.; Millan, A.; Palacio, F.; Kampert, E.; Zeitler, U.; de Brion, S.; Iglesias, O.; Labarta, A. *Phys. Rev. B* **2011**, *84*, 104427.
- (381) Galvez, N.; Fernandez, B.; Sanchez, P.; Morales-Sanfrutos, J.; Santoyo-Gonzalez, F.; Cuesta, R.; Bermejo, R.; Clemente-Leon, M.; Coronado, E.; Soriano-Portillo, A.; Dominguez-Vera, J. M. *Solid State Sci.* **2009**, *11*, 754.
- (382) Jung, J. H.; Eom, T. W.; Lee, Y. P.; Rhee, J. Y.; Choi, E. H. *J. Magn. Magn. Mater.* **2011**, *323*, 3077.
- (383) Jung, J. H.; Lee, Y. P. *J. Korean Phys. Soc.* **2011**, *58*, 966.
- (384) Silva, N. J. O.; Amaral, V. S.; Carlos, L. D. *Phys. Rev. B* **2005**, *71*, 184408.
- (385) Silva, N. J. O.; Amaral, V. S.; Carlos, L. D.; Rodriguez-Gonzalez, B.; Liz-Marzan, L. M.; Berquo, T. S.; Banerjee, S. K.; Bermudez, V. D.; Millan, A.; Palacio, F. *Phys. Rev. B* **2008**, *77*, 134426.
- (386) Gorham, N. T.; St Pierre, T. G.; Chua-Anusorn, W.; Parkinson, G. M. *J. Appl. Phys.* **2008**, *103*, 054302.
- (387) Silva, N. J. O.; Millan, A.; Palacio, F.; Kampert, E.; Zeitler, U.; Rakoto, H.; Amaral, V. S. *Phys. Rev. B* **2009**, *79*, 104405.
- (388) Pankowska, M.; Dobek, A. *J. Chem. Phys.* **2009**, *131*, 015105.
- (389) Bulte, J. W.; Douglas, T.; Mann, S.; Frankel, R. B.; Moskowitz, B. M.; Brooks, R. A.; Baumgartner, C. D.; Vymazal, J.; Strub, M. P.; Frank, J. A. *J. Magn. Reson.* **1994**, *4*, 497.
- (390) Bulte, J. W. M.; Douglas, T.; Mann, S.; Frankel, R. B.; Moskowitz, B. M.; Brooks, R. A.; Baumgartner, C. D.; Vymazal, J.; Frank, J. A. *Invest. Radiol.* **1994**, *29*, S214.
- (391) Martinez-Perez, M. J.; de Miguel, R.; Carbonera, C.; Martinez-Julvez, M.; Lostao, A.; Piquer, C.; Gomez-Moreno, C.; Bartolome, J.; Luis, F. *Nanotechnology* **2010**, *21*, 465707.
- (392) Koralewski, M.; Pochylski, M.; Mitroova, Z.; Timko, M.; Kopcansky, P.; Melnikova, L. *J. Magn. Magn. Mater.* **2011**, *323*, 2413.
- (393) Jordan, V. C.; Caplan, M. R.; Bennett, K. M. *Magn. Reson. Med.* **2010**, *64*, 1260.
- (394) Kostiainen, M. A.; Ceci, P.; Fornara, M.; Hiekkataipale, P.; Kasyutich, O.; Nolte, R. J. M.; Cornelissen, J. J. L. M.; Desautels, R. D.; van Lierop, J. *ACS Nano* **2011**, *5*, 6394.
- (395) Klem, M. T.; Resnick, D. A.; Gilmore, K.; Young, M.; Idzerda, Y. U.; Douglas, T. *J. Am. Chem. Soc.* **2007**, *129*, 197.
- (396) Hoinville, J.; Bewick, A.; Gleeson, D.; Jones, R.; Kasyutich, O.; Mayes, E.; Nartowski, A.; Warne, B.; Wiggins, J.; Wong, K. *J. Appl. Phys.* **2003**, *93*, 7187.
- (397) Hu, F. Q.; Joshi, H. M.; Dravid, V. P.; Meade, T. J. *Nanoscale* **2010**, *2*, 1884.
- (398) Waerzeggers, Y.; Monfare, P.; Viel, T.; Winkeler, A.; Voges, J.; Jacobs, A. H. *Methods* **2009**, *48*, 146.
- (399) Cormode, D. P.; Jarzyna, P. A.; Mulder, W. J. M.; Fayad, Z. A. *Adv. Drug Delivery Rev.* **2010**, *62*, 329.
- (400) Hasegawa, S.; Furukawa, T.; Saga, T. *Magn. Reson. Med. Sci.* **2010**, *9*, 37.
- (401) Ono, K.; Fuma, K.; Tabata, K.; Sawada, M. *Biochem. Biophys. Res. Commun.* **2009**, *388*, 589.
- (402) Liu, L. L.; Gong, K.; Ming, P. G.; Huang, Y.; Tang, Q.; Xu, G. L.; Yan, J. X.; Zhao, N. M.; Zhang, X. F.; Gong, Y. D. *Biotechnol. Lett.* **2010**, *32*, 743.
- (403) Beeman, S. C.; Georges, J. F.; Bennett, K. M. *Magn. Reson. Med.* **2013**, *69*, 853.
- (404) Terashima, M.; Uchida, M.; Kosuge, H.; Tsao, P. S.; Young, M. J.; Conolly, S. M.; Douglas, T.; McConnell, M. V. *Biomaterials* **2011**, *32*, 1430.
- (405) Iordanova, B.; Robison, C. S.; Ahrens, E. T. *J. Biol. Inorg. Chem.* **2010**, *15*, 957.
- (406) Qian, C.; Yu, X.; Chen, D.-Y.; Dodd, S.; Bouraoud, N.; Pothayee, N.; Chen, Y.; Beeman, S.; Bennett, K.; Murphy-Boesch, J.; Koretsky, A. *Radiology* **2013**, *268*, 228.
- (407) Bennett, K. M.; Shapiro, E. M.; Sotak, C. H.; Koretsky, A. P. *Biophys. J.* **2008**, *95*, 342.
- (408) Bennett, K. M.; Zhou, H.; Sumner, J. P.; Dodd, S. J.; Bouraoud, N.; Doi, K.; Star, R. A.; Koretsky, A. P. *Magn. Reson. Med.* **2008**, *60*, 564.
- (409) Beeman, S. C.; Zhang, M.; Gubhaju, L.; Wu, T.; Bertram, J. F.; Frakes, D. H.; Cherry, B. R.; Bennett, K. M. *Am. J. Physiol.: Renal Physiol.* **2011**, *300*, F1454.
- (410) Heilmann, M.; Neudecker, S.; Wolf, I.; Gubhaju, L.; Sticht, C.; Schock-Kusch, D.; Kriz, W.; Bertram, J. F.; Schad, L. R.; Gretz, N. *Nephrol., Dial., Transplant.* **2012**, *27*, 100.
- (411) Beeman, S. C.; Cullen-McEwen, L. A.; Puelles, V. G.; Zhang, M.; Wu, T.; Baldelomar, E. J.; Dowling, J.; Charlton, J. R.; Forbes, M. S.; Ng, A.; Wu, Q.; Armitage, J. A.; Egan, G. F.; Bertram, J. F.; Bennett, K. M. *Am. J. Physiol.: Renal Physiol.* **2014**, *306*, F1381.
- (412) van Rijn, P.; Tutus, M.; Kathrein, C.; Mougin, N. C.; Park, H.; Hein, C.; Schürings, M. P.; Böker, A. *Adv. Funct. Mater.* **2014**, *24*, 6762.